

American University in Cairo

AUC Knowledge Fountain

Theses and Dissertations

Student Research

Summer 6-15-2021

Fluid-Structure Interaction of NREL 5-MW Wind Turbine

Mohamed Sayed Elkady Abd-Elhay

The American University in Cairo AUC, mseikady@aucegypt.edu

Follow this and additional works at: <https://fount.aucegypt.edu/etds>



Part of the [Aerodynamics and Fluid Mechanics Commons](#), [Applied Mechanics Commons](#), [Computational Engineering Commons](#), [Energy Systems Commons](#), [Engineering Mechanics Commons](#), [Mechanics of Materials Commons](#), and the [Structures and Materials Commons](#)

Recommended Citation

APA Citation

Abd-Elhay, M. S. (2021). *Fluid-Structure Interaction of NREL 5-MW Wind Turbine* [Master's Thesis, the American University in Cairo]. AUC Knowledge Fountain.

<https://fount.aucegypt.edu/etds/1649>

MLA Citation

Abd-Elhay, Mohamed Sayed Elkady. *Fluid-Structure Interaction of NREL 5-MW Wind Turbine*. 2021. American University in Cairo, Master's Thesis. *AUC Knowledge Fountain*.

<https://fount.aucegypt.edu/etds/1649>

This Master's Thesis is brought to you for free and open access by the Student Research at AUC Knowledge Fountain. It has been accepted for inclusion in Theses and Dissertations by an authorized administrator of AUC Knowledge Fountain. For more information, please contact thesisadmin@aucegypt.edu.



THE AMERICAN UNIVERSITY IN CAIRO
SCHOOL OF SCIENCES AND ENGINEERING

**Fluid-Structure Interaction of
NREL 5- MW Wind Turbine**

By

Mohamed Sayed Elkady Abdelhay

A thesis submitted in partial fulfillment of the requirements for the degree of

Master of Science in Mechanical Engineering

Under the supervision of:

Dr. Mohamed El-Morsi

Associate Professor, Department of Mechanical Engineering
The American University in Cairo

Dr. Khalil El-Khodary

Associate Professor, Department of Mechanical Engineering
The American University in Cairo

May, 2021

Abstract

Wind energy is considered one of the major sources of renewable energy. Nowadays, wind turbine blades could exceed 100 m to maximize the generated power and minimize produced energy cost. Due to the enormous size of the wind turbines, the blades are subjected to failure by aerodynamics loads or instability issues. Also, the gravitational and centrifugal loads affect the wind turbine design because of the huge mass of the blades. Accordingly, wind turbine simulation became efficient in blade design to reduce the cost of its manufacturing. The fluid-structure interaction (FSI) is considered an effective way to study the turbine's behavior when the air and the blade are simulated as one system.

In the present study, NREL 5 MW wind turbine with a blade length of 61.5m long is selected as a reference turbine to apply the FSI. The FSI is performed using three commercial software. ANSYS Fluent is used for the Computational Fluid Dynamics (CFD) model. The Finite Element (FE) model is simulated by Abaqus. In order to link both models together and transfer the data between them, MPCCI software is used.

The blade is subjected to flap-wise deflection, edge-wise deflection, and torsion. So, a 2-way coupling simulation is implemented to optimize the blade deformation to protect it from hitting the tower, mitigate the effect of cyclic loading, and prevent the blade stall.

This study introduced two passive optimization methods: material Bend Twist Coupling (BTC) and blade root fixation.

One of the achievements of this study is that it is considered the first FSI research implemented at the AUC. Also, running the FSI model with three different codes and linking between them was another challenge. Moreover, it is concluded from this research that the 2-way coupling gives more accurate results than the 1-way coupling, although it is complicated. Although the centrifugal force reduces the flap-wise deflection, it significantly impacts the blade twist angle. The used material BTC optimization method improved the blade torsion

stiffness while the root fixation improved the longitudinal stiffness. The improvement in the blade protects it from fatigue loading and stall by reducing the peak-to-peak amplitude and twisting the blade to feather.

Abbreviations

BEM	Blade Element Momentum Theory
BTC	Bend Twist Coupling
CFD	Computational Fluid Dynamics
FEA	Finite Element Analysis
FSI	Fluid-Structure Interaction
HAWT	Horizontal Axis Wind Turbine
NREL	National Renewable Energy Laboratory
VAWT	Vertical Axis Wind Turbine

Acknowledgements

I would like to express my sincere gratitude to Dr. Mohamed El-Morsi and Dr. Khalil El-Khodary for guiding and supervising this research and offering the possibility to do it.

I also want to express my appreciation to my colleagues who supported me in finalizing this research. Special thanks to Yehia Raef, Youssef Abdel Raouf, and Ahmed Ali for their help and support.

Last but not least, I would like to thank my family for supporting me spiritually throughout my life.

Table of Contents

Abstract.....	i
Abbreviations.....	iii
Acknowledgements.....	iv
Table of Contents.....	v
List of Figures.....	viii
List of Tables.....	xi
Chapter 1 Introduction.....	1
1.1 Renewable energies.....	1
1.2 Wind turbine components:.....	4
1.2.1 Rotor:.....	4
1.2.2 Drivetrain:.....	5
1.2.3 Auxiliary aggregates and other components.....	6
1.2.4 Tower.....	7
1.3 Different designs of blades.....	7
1.4 Loads applied on the blade.....	9
1.4.1 Aerodynamic load.....	9
1.4.2 Gravitational load.....	9
1.4.3 Centrifugal load.....	10
1.4.4 Inertial Load.....	10
1.4.5 Gyroscopic load.....	11
1.5 Blade deformation.....	11
1.6 Load cases.....	12
1.7 Blade failure mechanism.....	13
1.7.1 Structural loading effects.....	13
1.7.2 Environmental conditions.....	13

1.8 Blade structure material	14
1.8.1 Fibers:	15
1.8.2 Matrix	15
Chapter 2 Literature Review	17
2.1 Introduction	17
2.2 FSI research categories:	18
2.2.1 Comparing:	19
2.2.2 Components affect:	24
2.2.3 Material design	30
2.2.4 Optimization:	32
Chapter 3 Model setup	40
3.1 NREL 5-MW Wind Turbine main properties	40
3.2 Blade geometry	40
3.3 Blade CAD Model.....	41
3.4 CFD model	43
3.4.1 Fluid Domains	43
3.4.2 CFD Mesh.....	45
3.4.3 CFD Model Setup.....	46
3.4.4 Mesh Independence	46
3.5 FE Model.....	47
3.5.1 Composite material layup and mechanical properties	47
3.5.2 FE model setup	49
3.6 FSI Model.....	51
Chapter 4 Results and Discussion.....	53
4.1 Introduction	53
4.2 CFD model validation	53
4.2.1 Blade tip speed and relative velocity	53

4.2.2	Generated power at rated conditions	55
4.2.3	Y^+ values.....	56
4.2.4	Wind turbine operating curve.....	57
4.3	FE model validation	57
4.3.1	Mode shapes	58
4.3.2	Blade deformation	60
4.4	Comparison between 1-way and 2-way coupling	61
4.4.1	Wind Load Only	61
4.4.2	Wind Load, Gravitational Load, and Centrifugal Load....	62
4.5	Optimization.....	64
4.5.1	Optimization by changing the fiber orientation in the cap	65
4.5.2	Optimization by increasing the fixation near the blade root	73
Chapter 5	Conclusion and recommendations	79
5.1	Conclusion.....	79
5.2	Recommendations	81
References	82
Appendix A	93
CFD mesh setup	93
Appendix B	95
CFD model setup	95
Appendix C	101
FE model setup	101
Appendix D	104
FSI model setup	104

List of Figures

Figure 1-1 Global power generated from wind energy [2]	1
Figure 1-2 (a) Horizontal Axis Wind Turbines (HAWT) (b) Vertical Axis Wind Turbines (VAWT)	2
Figure 1-3 Wind Turbine Components	4
Figure 1-4 Different blade design with (a) two webs (b) box girder [14]	8
Figure 1-5 Blade Three Regions [15]	8
Figure 1-6 Loads applied on the blade.....	9
Figure 1-7 Increase of the mass of blade with respect to rotor diameter [7].....	9
Figure 1-8 Gravitational load effect on blade [16]	10
Figure 1-9 Inertial load effect on blade[16].....	11
Figure 1-10 Load distribution	11
Figure 1-11 Blade loading [18].....	12
Figure 1-12 Blade damage sources	13
Figure 1-13 Blades Material Composition.....	14
Figure 2-1(a) one-way coupling (b) two ways coupling.....	18
Figure 2-2 FSI research categories	18
Figure 2-3 Torques for rigid and flexible cases [33]	20
Figure 2-4 Out of plane deflection [35]	21
Figure 2-5 CFD and FAST blade tip deflection [48].....	23
Figure 2-6 CFD, FAST, and Reference turbine rotor power [48]	24
Figure 2-7 Blade performance at different loads and materials [73]	31
Figure 2-8 Geometric Coupling [83]	33
Figure 2-9(a) Bend Twist Coupling (b) Extension Twist coupling [84]	34

Figure 3-1 Blade Geometry	41
Figure 3-2 Blade main zones	43
Figure 3-3 Breakdown of Fluid Domains	44
Figure 3-4 Surfaces and Volumes Identification	44
Figure 3-5 CFD grid of the rotating domain	45
Figure 3-6 Generated Power (MW) VS Number of Cells	47
Figure 3-7 Composite material distribution along wind turbine blade cross-section.....	50
Figure 3-8 MPCCI Simulation Steps	52
Figure 4-1 Blade Tip Speed	54
Figure 4-2 Relative Velocity Vectors Magnitude and Direction along the Blade Span at (a) 10m (b) 20m (c) 30m (d) 40m (e) 50m (f) 60m	55
Figure 4-3 Pressure distribution on the blade	58
Figure 4-4 Blade Mode Shapes (a) First Flapwise (b) First Edgewise (c) Second Flapwise (d) Second Edgewise (e) Third Flapwise (f) First Torsion	59
Figure 4-5 The Blade Flap-Wise and Edge-Wise Deflection	61
Figure 4-6 Applied gravitational and centrifugal loads at each blade position (a) 0° (b) 90° (c) 180° (d) 270°	62
Figure 4-7 comparison between blade deformation during one cycle (a) Flap-wise deflection (b) Edge-wise deflection (c) Tip twist angle	64
Figure 4-8 Carbon fibers orientation in the spar cap	66
Figure 4-9 Output power with and without BTC	66
Figure 4-10 Blade deformation at the tip for 0,5,10,15 carbon fiber orientation (a) Flap-wise deflection (b) Edge-wise deflection (c) Twist angle	68

Figure 4-11 Blade deformation at 20m of the blade span for 0°,5°,10°,15° carbon fiber orientation (a) Flap-wise deflection (b) Edge-wise deflection (c) Twist angle 69

Figure 4-12 Blade deformation at 30m of the blade span for 0°,5°,10°,15° carbon fiber orientation (a) Flap-wise deflection (b) Edge-wise deflection (c) Twist angle 70

Figure 4-13 Blade deformation at 40m of the blade span for 0°,5°,10°,15° carbon fiber orientation (a) Flap-wise deflection (b) Edge-wise deflection (c) Twist angle 71

Figure 4-14 Blade deformation at 50m of the blade span for 0°,5°,10°,15° carbon fiber orientation (a) Flap-wise deflection (b) Edge-wise deflection (c) Twist angle 72

Figure 4-15 Blade fixation 73

Figure 4-16 Comparison of the output power between the rigid and different fixation schemes 73

Figure 4-17 Blade deformation at the tip for 0m, 1.5m, 3m fixation (a) Flap-wise deflection (b) Edge-wise deflection (c) Twist angle 74

Figure 4-18 Blade deformation at 20m of the blade span for 0m, 1.5m, 3m fixation (a) Flap-wise deflection (b) Edge-wise deflection (c) Twist angle 75

Figure 4-19 Blade deformation at 30m of the blade span for 0m, 1.5m, 3m fixation (a) Flap-wise deflection (b) Edge-wise deflection (c) Twist angle 76

Figure 4-20 Blade deformation at 40m of the blade span for 0m, 1.5m, 3m fixation (a) Flap-wise deflection (b) Edge-wise deflection (c) Twist angle 77

Figure 4-21 Blade deformation at 50m of the blade span for 0m, 1.5m, 3m fixation (a) Flap-wise deflection (b) Edge-wise deflection (c) Twist angle 78

List of Tables

Table 3-1 NREL 5-MW Wind Turbine main properties	40
Table 3-2 NREL 5 MW blade Airfoil properties [102]	42
Table 3-3 Generated Power Values At Each Grid	47
Table 3-4 Summary of material properties	48
Table 4-1 Comparison of generated power with other studies	56
Table 4-2 Wind Turbine Performance Curve	57
Table 4-3 Blade Modal Frequencies	59
Table 4-4 Blade modal frequencies	60
Table 4-5 Difference Between 1-Way and 2-Way Coupling.....	62
Table 4-6 Difference between blade deformation at different azimuth angle including the load combination	63
Table 4-7 BTC blade deformation	68

Chapter 1 Introduction

1.1 Renewable energies

Fossil fuel consumption is reduced globally due to its negative impact on the environment, such as the greenhouse effect. Also, the fossil fuel reserves in nature can run out. Renewable energy (RE) is now considered the best energy source capable of replacing fossil fuels in power generation. Wind, solar, hydro, bioenergy, and geothermal are the main renewable energy sources. The main drawback of using renewable energy is its irregular availability.

The sources of renewable energy are classified into two groups based on their availability, quality, location, and constraints. Solar and wind energy are classified as group 1, while the remaining sources are located under group 2.[1]

The total generated power from wind energy globally is 620 GW in 2020, as indicated in the British Petroleum Statistical Review of World Energy. This value is 10% higher than that generated in 2018. The produced energy by offshore wind turbines is 28 GW. As illustrated in Figure 1-1, China generated 25.8 GW in 2019 with total production from wind energy of 210 GW while the total generated power in Europe and the United States of America is 23 GW. [2]

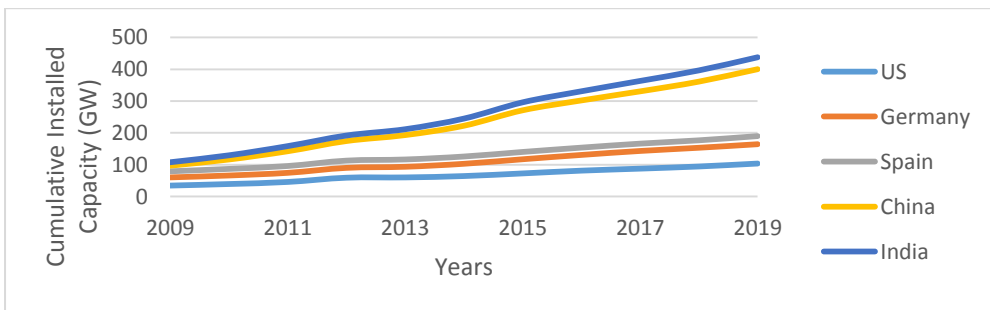


Figure 1-1 Global power generated from wind energy [2]

Wind turbines are classified into Vertical Axis Wind Turbines (VAWT) and Horizontal Axis Wind Turbines (HAWT). The difference between the two types is the axis of rotation. HAWT's gearbox and generator are located at the top of the turbine tower. The blades rotate at a low speed which is then converted by the gearbox to a higher speed. Regarding VAWT, the gearbox and the generator are at the turbine's base (Figure 1-2).

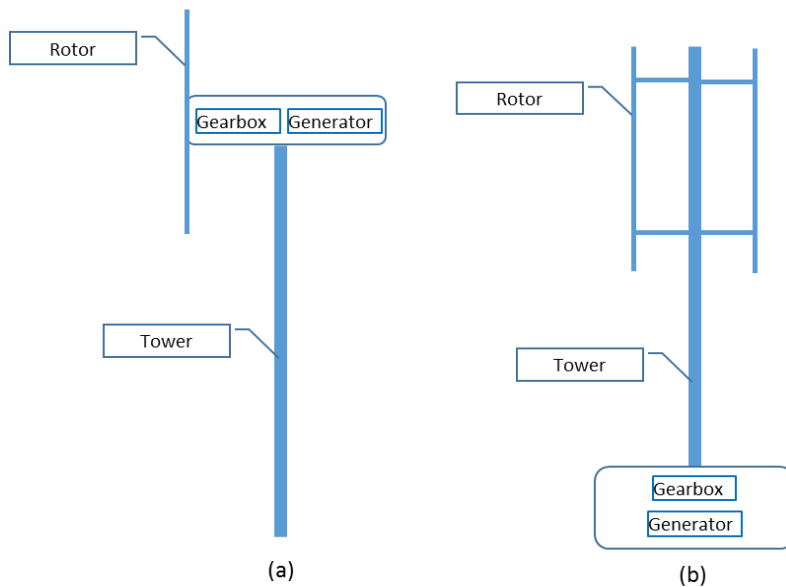


Figure 1-2 (a) Horizontal Axis Wind Turbines (HAWT) (b) Vertical Axis Wind Turbines (VAWT)

Wind turbines are built either onshore or offshore; however, the offshore turbines' capacity is higher than onshore. Wind turbine capacities have increased from less than 1 MW in the previous decades to around 10 MW today. Because of the rapid increase in wind turbine capacity, the rotor diameter has increased. In some cases, the rotor diameter exceeds 120m.

Because of the enormous sizes of wind turbine rotors, it is critical to predicting the turbine's response prior to construction. Simulation of the turbine before manufacturing is important to predict the generated power and achieve the best design. Wind turbine simulation includes 3D modeling, aerodynamics,

material properties, and air-turbine interaction. Because of the harsh environmental conditions, offshore wind turbines with higher capacities and massive rotor diameters must receive more attention. As a result, many engineering aspects should be taken into account when simulating offshore wind turbines. The blade element momentum theory (BEM) used in the design of traditional wind turbines does not consider complex blade geometry, flow separation, or time-dependent phenomena. [3]

Many wind turbine studies focus on either fluid dynamics or blade deformation. In aerodynamic studies, the blade is considered a rigid body. The behavior of air passing through the turbine, such as angle of attack, lift force, drag force, and aerodynamic torque, is investigated. While in Finite Element (FE) models, the main goal is to improve the mechanical properties of the blade material to achieve the least amount of mass and the greatest resistance to deformation.

The main goal of this thesis is to investigate the interaction between air and blade material by investigating the deformation of the blade caused by air pressure and its impact on generated power. Also, blade optimization methods are proposed to protect the blade from failure due to bending moment, torsion, stall, or cyclic loading. This type of investigation is known as fluid-structure interaction (FSI), and it will be carried out using ANSYS fluent [4] for Computational Fluid Dynamics (CFD) and Abaqus [5] for Finite Element Analysis (FEA), as well as MPCCI [6] to connect the two software.

1.2 Wind turbine components:

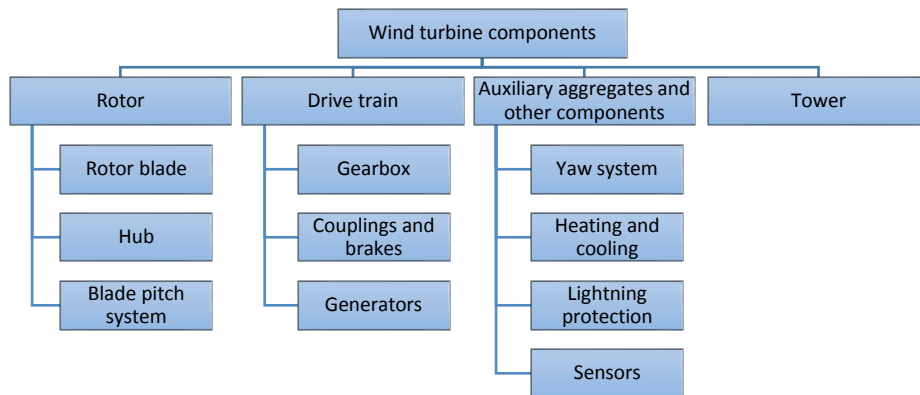


Figure 1-3 Wind Turbine Components

1.2.1 Rotor:

The rotor is considered the main component of the wind turbine, consisting of the blades, hub, and pitch system. It is responsible for converting wind energy to mechanical energy. There are two types of rotors of horizontal axis wind turbines:

Upwind rotor: the rotor is located in front of the tower facing the wind direction. This type is commonly used nowadays in most commercial wind turbines. However, it requires an active yaw system.

Downwind rotor: the rotor is located behind the tower. The main disadvantage of this design is that an additional load is applied on the rotor due to wakes generated behind the tower.[7]

1.2.1.1 Rotor blade:

The blade consists of different airfoils whose aerodynamic shape affects the generated power. High-quality profile selection leads to a higher lift to drag

coefficient. Generally, the blades are manufactured from glass fiber reinforced plastics or carbon fiber reinforced plastics. Recently, carbon fibers are commonly used due to their higher strength, but they are more expensive. Erosion prevention material is added on the leading edge to protect it during operation. The blade root is connected to the turbine hub by studs.[7]

1.2.1.2 Hub:

The hub holds the wind turbine blades and transfers their rotational motion to the generator. Its shape is complex, so it is manufactured by casting. There are two shapes commonly used for the hub:

- Tri-cylindrical: consists of three cylinders each one is at the same axis of its blade
- Spherical: consists of spherical shape with cutout at each blade. [8]

1.2.1.3 Blade pitch system:

The blade is pitched due to a reduction in lift force or flow separation to overcome the unusual operating condition. This system is driven by electrical, mechanical, or hydraulic energy. The electrical system is commonly used for large turbines with a rated power of multi-megawatts by providing a gear motor for each blade.[7]

1.2.2 Drivetrain:

The wind turbine drivetrain is responsible for transmitting the power from the rotor to the generator through the rotor shaft, gearbox, coupling, and brakes.[9]

1.2.2.1 Gearbox:

The rotational speed of the rotor is changed to the desired one by the generator through the gearbox. The transmission ratio is determined by the rotor speed, number of poles, and grid frequency.[7]

1.2.2.2 Couplings and brakes:

The huge torque is transmitted from the rotor shaft to the slow shaft of the gearbox through rigid coupling. While an elastic coupling is used to transmit the smaller torque between the fast shaft of the gearbox and generator and absorb any misalignment between them.

There is a disk brake on the fast shaft of the gearbox, which is designed to deal with emergency cases as the braking system is responsible for converting over speed rotation to a standstill within few seconds. The braking procedure during normal operation starts with an aerodynamic brake, and then the mechanical brake is activated for the remaining small torque to stop the rotor completely. [7]

1.2.2.3 Generator:

Wind turbine generators are responsible for converting the captured kinetic energy by the rotor to electrical energy. Generator selection is based on its reliability, efficiency, speed range, cost, and compact size to produce maximum power [10].

1.2.3 Auxiliary aggregates and other components

1.2.3.1 Yaw system

The Yaw system is responsible for rotating the turbine rotor with nacelle around the tower to be perpendicular to the wind to maximize the captured wind energy. The yaw system could be active or passive depending on the rotor type (upwind or downwind). The yaw system consists of yaw drives with electric motors, yaw brakes, and yaw bearings [11].

1.2.3.2 Heating and cooling

A cooling system is required in wind turbines to protect turbine parts from heat generated from gearbox and generator. Also, a heating system is important when there is a probability of icing. Ice accumulation on blades affects blade aerodynamics and causes vibrations due to mass unbalance[7].

1.2.3.3 Lightning protection

A lightning system is installed on the blades to absorb the lightning current and conduct it to the ground through cables inside the blade [12].

1.2.3.4 Sensors

A huge number of sensors are installed on the turbine to continuously monitor operating data such as wind speed and direction, temperature, pressure, vibration, and electrical data [7].

1.2.4 Tower

The tower carries the wind turbine rotor and nacelle. Towers are considered the heaviest part of the turbine which represents about 65% of the turbine weight. Towers are commonly constructed from pre-stressed concrete and steel [13]

1.3 Different designs of blades

Factors that affect blade design are its structural and aerodynamic considerations. Generally, the blade is formed of two shells joined with one web or more to transfer the loads. In some designs, a box girder is used in two webs-blade. Figure 1-4 shows different blade designs with one web, two webs, and a box girder.[14]

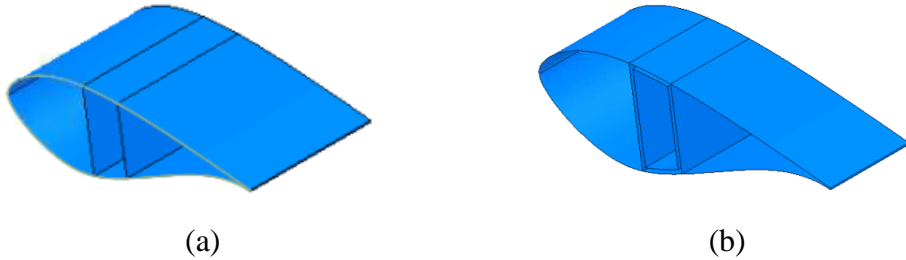


Figure 1-4 Different blade design with (a) two webs (b) box girder [14]

The effect of aerodynamic considerations appears in the outer two-third of blade span, while the importance of structure design appears along one-third of blade length measured from its root. As shown in Figure 1-5, the blade span is divided into three regions:

- Root region: in this area, where the highest load is applied, the circular cross-section of the blade is converted to an airfoil shape. Near the blade root, the relative velocity is low due to the small radius of the rotor at this area which leads to a low aerodynamic lift. Accordingly, this area is considered the highest thickness with the lowest aerodynamic efficiency.
- Mid region: lift to drag ratio is increased by moving along the blade span towards its tip.
- Tip region: this region is aerodynamically critical. The aerodynamic lift is maximized. [15]

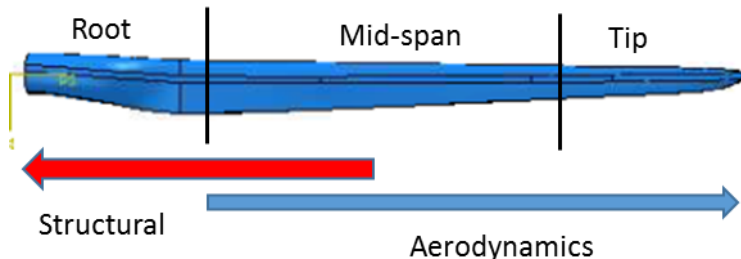


Figure 1-5 Blade Three Regions [15]

1.4 Loads applied on the blade

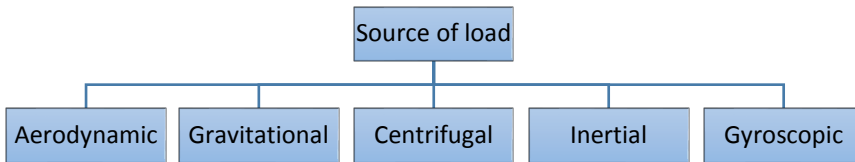


Figure 1-6 Loads applied on the blade

1.4.1 Aerodynamic load

Aerodynamic loads are responsible for generating power. When the wind passes through the blade, the lift and drag forces are converted to driving and thrust forces. According to change in wind speed and angular velocity, the relative velocity, angle of attack, and aerodynamic forces are changed [14]

1.4.2 Gravitational load

Centrifugal force is dependent on blade mass. According to similarity law, the mass of the blade is directly proportional to the cube of its radius (R). However, the mass of the commercial blade to their diameter is reduced to the power of 2.2 instead of 3 as shown in Figure 1-7 [7].

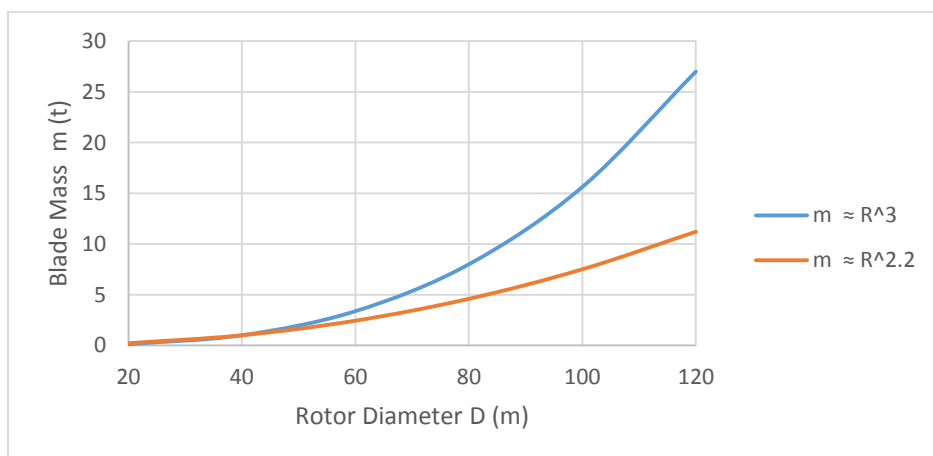


Figure 1-7 Increase of the mass of blade with respect to rotor diameter [7]

According to Figure 1-8, when the blade is at position 1 and due to gravitational force, the leading edge is subjected to compression stress while the trailing edge side is tensioned. At position 2, the leading edge is exposed to tension stress and the trailing edge is compressed. Accordingly, a sinusoidal loading is generated on the blade due to gravity. The lifetime of the wind turbine is considered to be 20 years, and if it operates at 12.1 rpm, so the total number of gravity stress cycles are $12.1 \times 60 \times 24 \times 365 \times 20 = 1.3 \times 10^8$ [16]

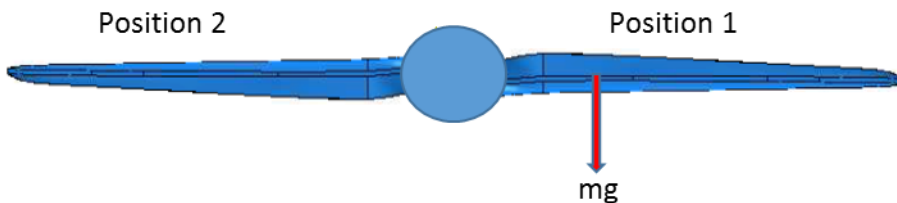


Figure 1-8 Gravitational load effect on blade [16]

1.4.3 Centrifugal load

The centrifugal force acts radially and outward which is a function of rotational velocity squared, mass, and radius of the blade.

1.4.4 Inertial Load

The inertial loading could be generated due to the operation of the wind turbine during its acceleration and deceleration such as starting, shutdown, or braking. Due to the change in normal operation, a small section will be subjected to force of $df = \dot{\omega} r m dr$ where m is the mass, r is the radius at this point and $\dot{\omega}$ is angular acceleration or deceleration as shown in Figure 1-9. [16]

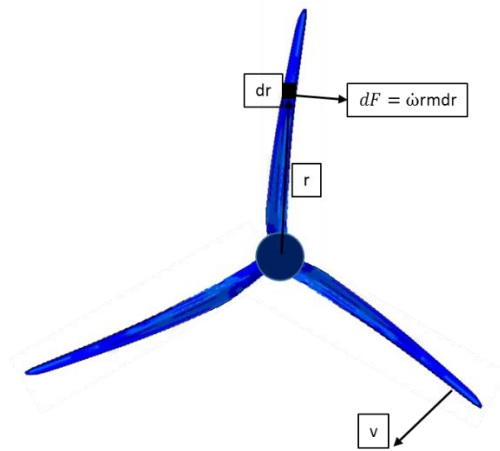


Figure 1-9 Inertial load effect on blade[16]

1.4.5 Gyroscopic load

The gyroscopic load is generated from the yaw movement. Due to yawing of the rotor about the vertical axis and rotation of the rotor about the spinning axis, an out-of-plane bending moment is generated on the rotor. The gyroscopic moment effect could not be considered as its value is small with respect to other loads on the blade such as the aerodynamic load because the rate is slow which is about 0.5 deg/ sec. [17]

1.5 Blade deformation

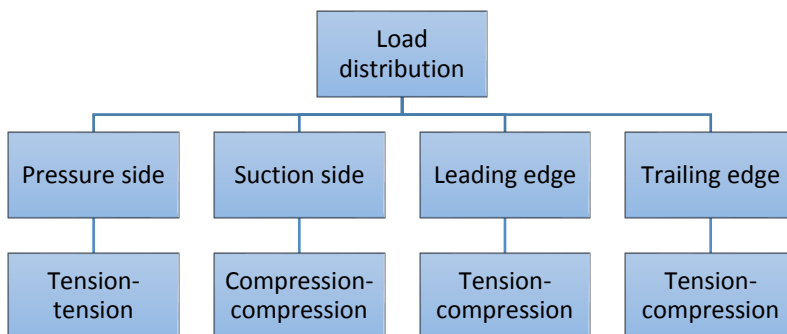


Figure 1-10 Load distribution

The blade is subjected to two types of deformation, flap-wise and edgewise. The source of flap-wise deformation is wind pressure, while the edgewise is caused by gravitational force and torque loads. The webs are responsible for resisting the flap-wise bending, and edgewise bending is resisted by leading and trailing edges. Blade pressure and suction sides are subjected to tension-tension and compression-compression cyclic loading respectively while leading and trailing edges are subjected to tension-compression loading. (Figure 1-11) [18]

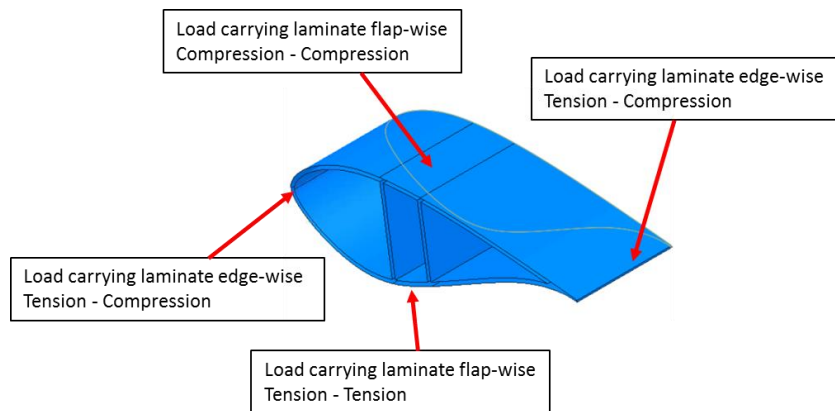


Figure 1-11 Blade loading [18]

1.6 Load cases

A combination of loads are applied on the blade during different normal conditions as follows [19]:

- Standby condition: aerodynamic loads, gravitational load and wind speed, and direction change.
- Startup condition: aerodynamic loads, gravitational load, and inertial load.
- Power production: aerodynamic loads, gravitational load, centrifugal force, Gyroscopic load, and wind speed direction change
- Shutdown: aerodynamic loads, gravitational load, and inertial load.

1.7 Blade failure mechanism

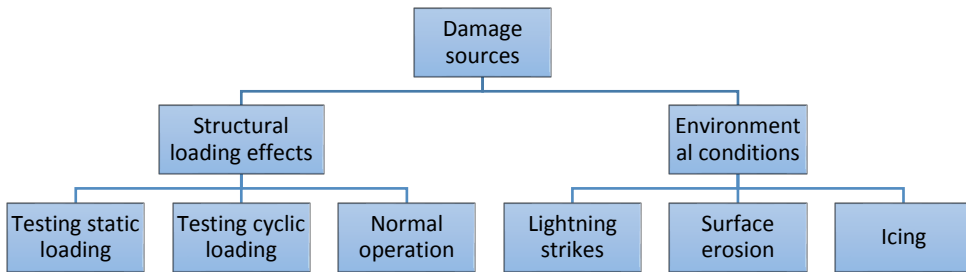


Figure 1-12 Blade damage sources

The damage in the blade is caused by mechanical or environmental conditions which could be at lamina or laminate or structural scale. Lamina scale damage is reflected in matrix cracking, fiber breaking, or matrix fiber debonding, while delamination is considered as laminate scale damage. The structural scale damage is represented in damage of the main component. [20]

1.7.1 Structural loading effects

There are different damage modes in wind turbine blades due to applied loads. The damage could occur during testing (static or cyclic) or the operation of the blade. The different types of blade damage are [21]:

- Damage in the adhesive layer (leading edge, trailing edge, skin/spar, or sandwich panel debonding)
- Delamination (Skin or spar)
- Splitting and fracture of fibers
- Cracks in Gelcoat

1.7.2 Environmental conditions

In addition to mechanical loading damage, the damage could occur due to environmental conditions such as lightning strikes, surface erosion, or icing. The wind turbine blade is subjected to several lightning strikes during its

lifetime. Although the blades are equipped with a lightning protection system, damage and cracks are found around lightning attraction points.[12]

Also, blade erosion is caused by the impact of airborne particulates at its leading edge. This erosion results in reduced power production and leads to blade damage. Moreover, the accumulation of ice on the blade surface causes unbalancing in load distribution and reduction in generated energy.[18]

1.8 Blade structure material

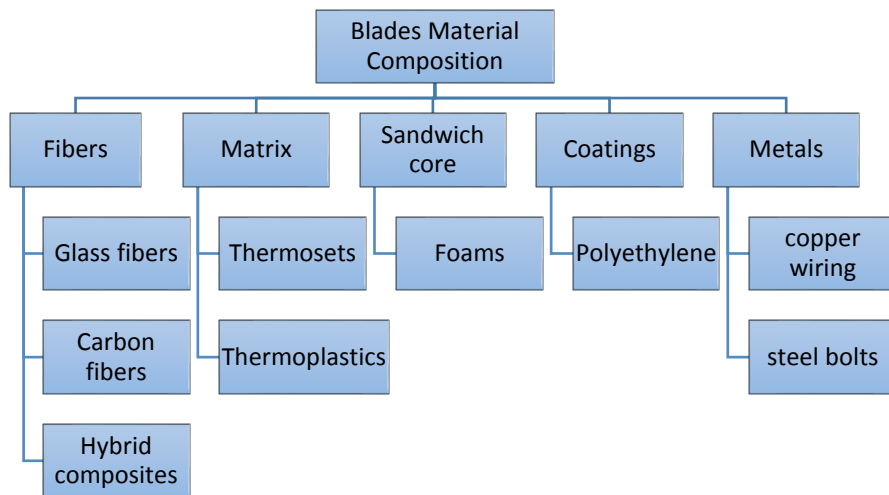


Figure 1-13 Blades Material Composition

Wind turbine blade materials differ from one designer or manufacturer to another; however, there are main materials that are commonly used in blade design. As indicated in Figure 1-13, the blade is composed of reinforcement fibers in a polymer matrix, sandwich core from wood or foam, coatings such as polyethylene, and metals used in wiring and bolts [22]

Reinforcement fibers and matrix only will be discussed in more details in this section:

1.8.1 Fibers:

1.8.1.1 Glass fibers:

Glass fibers are used to increase the stiffness, tensile and compression strengths. However, increasing their volume content will affect the bonding between fibers and matrix and fatigue resistance [23]. E-glass fibers are commonly used. S-glass type is considered a promising reinforcement due to its higher stiffness, tensile, and compression strengths but its cost is also high [18].

1.8.1.2 Carbon fibers:

Carbon fibers have higher stiffness and lower density than fiberglass which leads to a stiffer and lighter blade. The main disadvantages of carbon fibers are their high cost and sensitivity to misalignment which leads to a reduction in fatigue resistance [18].

1.8.1.3 Hybrid composites:

This type of reinforcement represents a combination of both glass and carbon fibers. Partial replacement of about 30% of glass fiber will lead to a 50% reduction in blade weight and a 90% increase in its cost [18]

1.8.2 Matrix

1.8.2.1 Thermosets:

Thermosets are commonly used as composite matrices due to their low curing temperature. Currently, epoxy resins are used to replace polyester resins [19].

1.8.2.2 Thermoplastics:

Thermoplastics could replace thermoset matrices due to their recyclability. However, thermoplastics require high temperatures during processing and are

difficult to be manufactured. The fracture toughness of thermoplastics is higher than thermosets but the fatigue resistance is low [24].

The objective of this study is to optimize NREL 5-MW wind turbine to protect the blades from failure due to different types of deformation by applying FSI simulation using ANSYS Fluent [4] for the CFD model, Abaqus [5] for the FE model, and MPCCI [6] for transferring the data between both models. This optimization aims to reduce the peak-to-peak amplitude of flap-wise deflection to protect the blade from cyclic loading. Also, by reducing the twist angle at different blade positions, the blade is twisted to feather and protected from stall. Chapter 2 presents a review of the previous works in the area of FSI applied on wind turbines. In Chapter 3, the wind turbine aerodynamics and material are presented. In addition, the CFD, FE, and FSI models setup are introduced. Chapter 4 presents the numerical simulation performed to validate the models, compare 1-way with 2-way coupling results, and optimize the blade to improve its performance. Finally, Chapter 5 presents the conclusions and recommendations for future work.

Chapter 2 Literature Review

2.1 Introduction

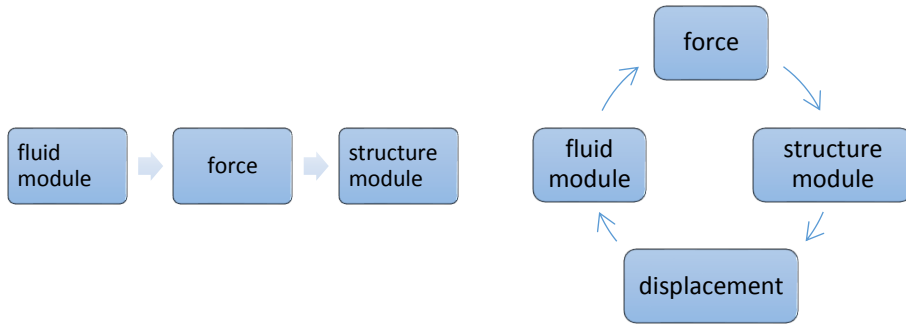
Many studies have been conducted on the fluid-structure interaction (FSI) of wind turbines ranging in size from a few kW to several MW. This chapter discusses FSI research on wind turbines, including the various fields investigated, input data, software used in simulation, and results.

Before linking the CFD model with the FE model through FSI simulation, each model is validated separately. The simulation results are compared with experimental data, previous studies, or calculations.

FSI is the method by which air and turbine blades communicate. Previously, each model was studied separately. Air behavior is studied around the blade, which is considered a rigid body, and the blade deformation is investigated as a separate component, without taking into account the effect of each part when they are linked as a single system.

To simulate this coupling, various approaches are used. 1-way coupling is used in some papers, while the 2-way coupling is used in others. FSI is performed by ANSYS [25], MPCCI [6], COMSOL [26], or in-house codes.

In the case of 1-way coupling, the fluid domain is solved until meeting the convergence criteria, then the pressure distribution on the blade is transferred to the structural model. The transferred pressure values are included in the FE model analysis to obtain stress on the blade. However, in the 2-way coupling, the new shape of the deformed blade is transferred back to the fluid again. Figure 2-1 distinguishes between 1-way and 2-way coupling.



(a) (b)
 Figure 2-1(a) one-way coupling (b) two ways coupling

2.2 FSI research categories:

FSI research is categorized into four main areas as shown in Figure 2-2

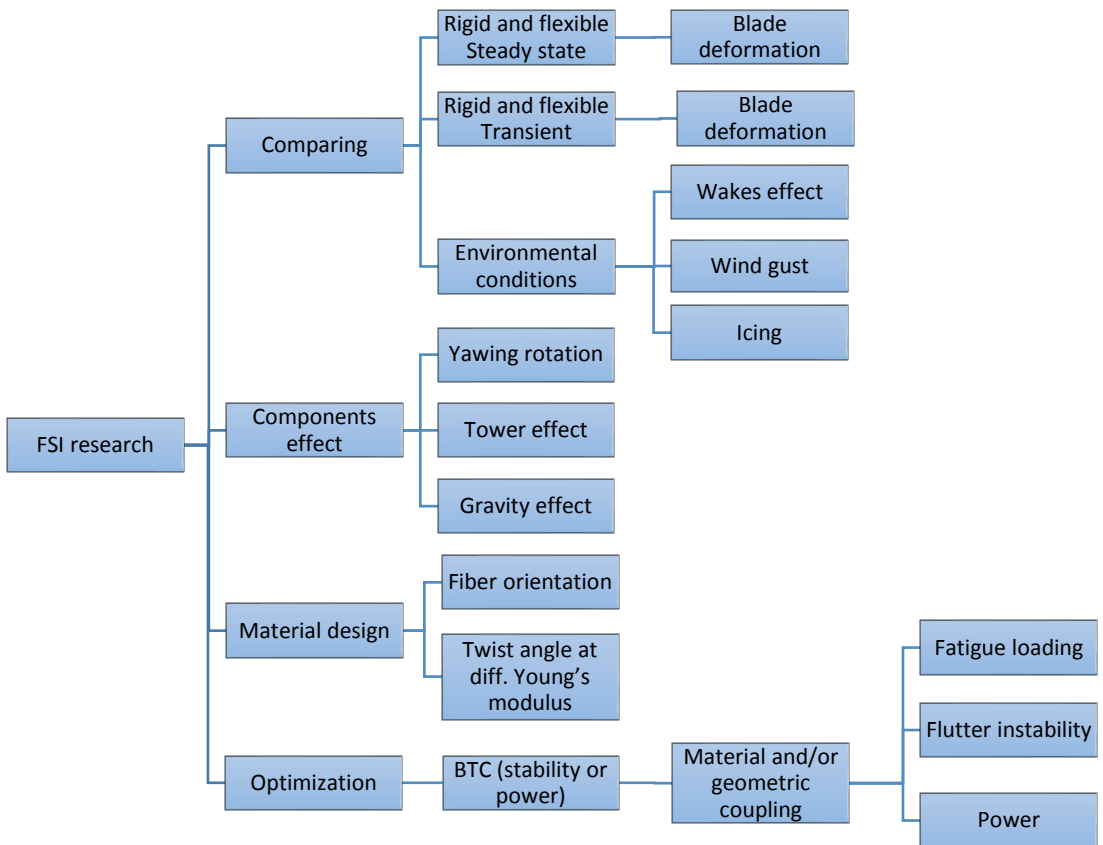


Figure 2-2 FSI research categories

2.2.1 Comparing:

Most FSI research depends on comparing the rigid case with a flexible one. Some researchers stop at the comparison only, while the rest use it as a first step to validate their model before going to the main point of the research. For example, one-way or two-way couplings are applied to study the FSI effect on power or blade deformation. Otherwise, the FSI model is validated against other research then the study purpose is applied such as optimization methods.

Cai et al. [27] applied the FSI comparing concept in their study. He validated the CFD model against a 1.5 MW wind turbine using ANSYS CFX and $k - \omega SST$ turbulent model. Then he applied BEM method by calculating lift and drag coefficients at 1m intervals. Regarding the finite element model, the blade was modeled with shell elements and composite materials using ANSYS and compared with experimental data. Finally, the flap-wise bending was simulated through one-way FSI to check the clearance between the blade and tower.

Another study was carried out by Jeong et al. [28] to investigate the aeroelastic response of wind turbines due to wake effects. CFD model was analyzed using Fluent with $k - \omega SST$ turbulence model and the tructure model was solved using Ansys. NREL 5 MW [29] and NREL phase VI [30] wind turbines were presented in this study as reference blades. It was shown from the FSI analysis that wakes affect the aeroelastic damping for edgewise modes, while the effect on flap-wise modes was almost the same as the results from the uniform inflow.

In 2014, Carrión et al. [31] applied FSI on MEXICO wind turbine [32]. Helicopter Multi-Block (HMB) code developed at the University of Liverpool was used to solve the CFD part, while FEA was performed by NASTRAN.

The author compared the wake generated after the rotor and the experimental data and studied the effect of low Mach number on blade loading.

According to Macphee and Beyene's [33] study comparing simulation and experimental data for both rigid and flexible cases. It was concluded that the torque for flexible cases (experimental and simulation) is higher than the rigid ones by about 67% of the average power production. As shown in Figure 2-3, experimental and simulated torques for rigid and flexible cases are 0.159 N.m, 0.1614 N.m, 0.209, and 0.196 respectively.

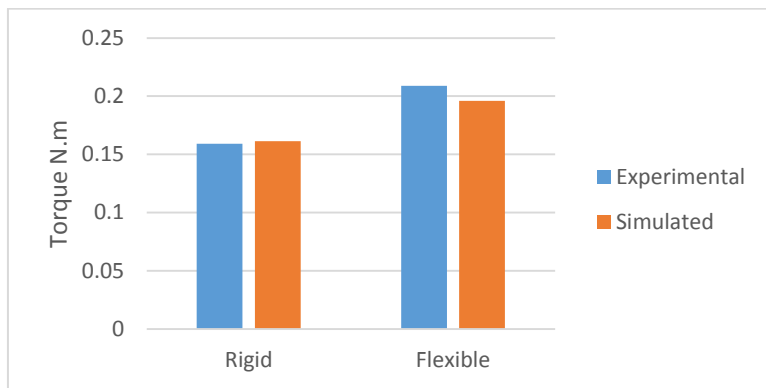


Figure 2-3 Torques for rigid and flexible cases [33]

Two-way coupling analysis was performed also by Braaten et al. [34] using ANSYS CFX and ANSYS mechanical to investigate bending, twist angle, stresses, and strains within the blade. He performed steady-state analysis to study blade deformation under different wind conditions and transient analysis for unsteady wind conditions. Both CFD and FE models were validated before applying FSI. Finally, the author compared computation outputs with ADAMS results for the same cases.

In Wenwei et al. [35] research, two models were presented: aeroelastic coupling (deformation and vibration were coupled with blade aerodynamic loads) was included and aeroelastic coupling was neglected. As a result, the

deflection and vibration amplitude in case of neglecting aeroelastic coupling was larger than the first case (Figure 2-4).

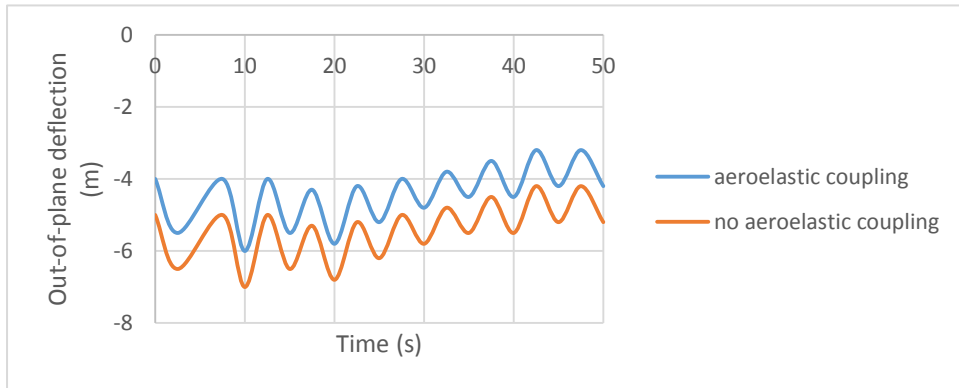


Figure 2-4 Out of plane deflection [35]

Also, Wenwei et al. [35] compared steady with unsteady cases and concluded that the lift coefficient in the unsteady case was larger than steady cases by 40.5% which lead to stall generation. Moreover, the same results were indicated in [36].

One way FSI was implemented on a 1.5 MW wind turbine by Wang et al. [37] using ANSYS FLUENT for CFD and ANSYS Static Structure for FEA models. The coupling was performed on five operational cases then flap-wise and edgewise deflections in each case were compared with other reference analyses. The torque generated from the CFD model was validated against FAST code [38] torque, and the maximum difference was 18.6%. Also, six modal shapes were generated for the FEA model. The maximum flap-wise tip deflection was 1.8m which was lower than the distance from the tower.

Another research that compared rigid with flexible blades was presented by Hoogedoorn et al. [39]. This research studied the response of a 2D airfoil under different wind conditions. The airfoil aerodynamics was performed using X-Foil [40] then coupled to MATLAB partial differential equation toolbox [41] to compute the solid deformation. It was concluded that increasing the airfoil

thickness led to higher resistance to deformation and lower camber deformation, while the flexible cambered airfoil improved lift force and turbine performance.

Also, FSI was used to study the effect of wind gust on large wind turbines. The research was presented by Gilberto et al. [42] to study the performance, loads, and deflection of the blade subjected to different gust models. Two gusts were selected to impact the blade which is developed by Timme et al. [43]. The results showed that the separation of the flow over the blade due to the gust reduced the blade deflection

The icing simulation of a wind turbine blade was presented by Wang & Zhu [44] using NREL phase VI wind turbine [30] as a reference turbine. It was concluded that the droplets impacted the leading edge and their concentration was large at the blade tip. Also, icing occurred on the leading edge with higher thickness at a stagnation point.

Another kind of research that used FSI to compare blade testing in the laboratory with the actual operating condition was implemented by Grinderslev et al. [45]. In order to certify a blade, full-scale tests shall be applied on it such as static and fatigue load tests. The fatigue test is performed by oscillating the blade for 2 million to 10 million cycles in flap-wise and edgewise directions [46]; however, the aerodynamics around the blade differs from the actual operating condition. Accordingly, the FSI model was applied to the blade by pulling and releasing it to validate the result with the experimental data. Then the model was used to simulate the wakes around the oscillating blade. The generated large vortices affected the drag force coefficients and exceeded those at normal operation.

A comparison between bidirectional FSI (BFSI) and unidirectional FSI (UFSI) was presented by Shi et al. [47]. In this research, a 5 MW wind turbine was

used to differentiate between different rotating and wind speeds using BFSI and UFSI. It was obtained that the displacement in the rotating conditions is higher in the UFSI case than in the BFSI case. Also, the displacement of the blade under rotation is higher than the static one. Moreover, the displacement was increased nonlinearly by increasing the rotational speed.

In 2012, Corson et al. [48] used Commercial CFD software AcuSolve in FSI simulation to study the aeroelastic behavior of 13.2 MW wind turbine. The researcher compared flap-wise deflection, edgewise deflection for the rigid with the flexible blade, and FAST calculation at different rotor speeds. Also, he compared the power curve of the blade against FAST calculation and found that power calculated from the CFD model was near FAST calculation at low wind speed up to the rated one. While the power dropped below the rated value at higher wind speed as shown in Figure 2-5 and Figure 2-6

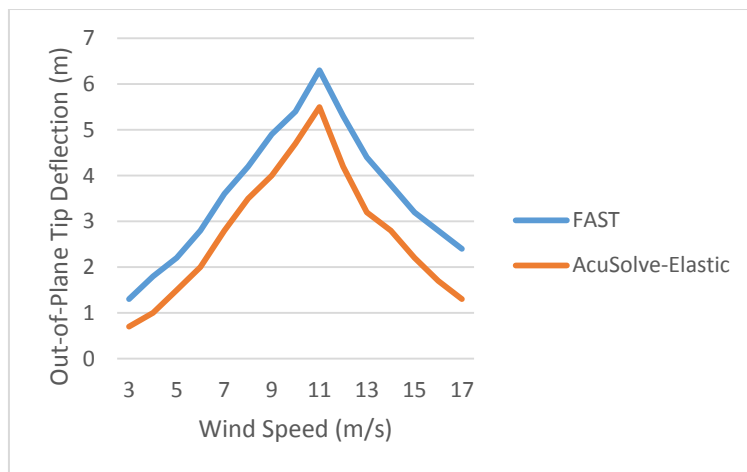


Figure 2-5 CFD and FAST blade tip deflection [48]

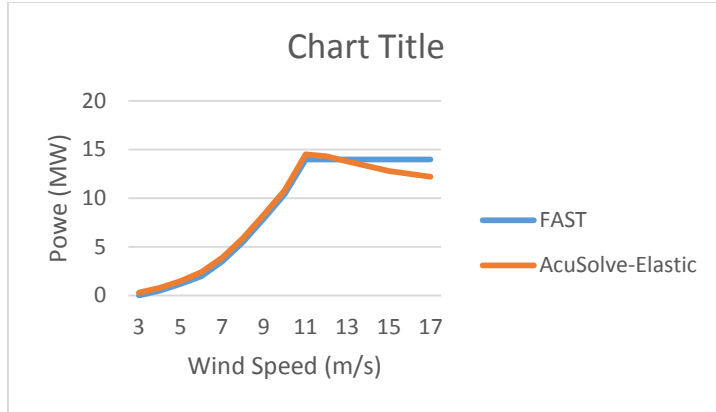


Figure 2-6 CFD, FAST, and Reference turbine rotor power [48]

In 2020, Ziying et al. [49] presented a comparison between the model developed in that study and the results of 5 MW NREL wind turbine performance including power, thrust, and deformation introduced in different research. The reference results were captured from 7 studies. The power and thrust were compared against research [29], [50]–[55] while the tip deflection was compared against [29], [51], [54], [55]. The results showed variation below and above the reference performance data.

2.2.2 Components affect:

Researchers studied the effect of some components on the performance of wind turbines such as the effect of tower, yaw, or gravity force of the blade. For each study, both models are studied separately before applying FSI.

2.2.2.1 Yawing rotation:

According to Dose et al. [56] research, a 5 MW NREL [29] wind turbine was used in FSI simulation. This study aimed to investigate the blade deformation effect on power and thrust. Also, the effect of turbine structure deformation such as yawing motion case on turbine performance is studied.

CFD solver used was open source CFD toolbox OpenFOAM [57] with $k - \omega - SST$ turbulence model. The structure solver was an in-house tool

BeamFoam. The coupling between both models is performed by SIMPLE-PISO algorithm PIMPLE which is included in OpenFOAM package.

Four rotor configurations were studied:

- 1- No blade cone, no rotor tilt, and yaw angle of 0°
- 2- No blade cone, no rotor tilt, and yaw angle of 30°
- 3- Blade cone of 2.5° , no rotor tilt and yaw angle of 0°
- 4- Blade cone of 2.5° , rotor tilt of 5° and yaw angle of 0°

The aerodynamic power and thrust from the CFD model were compared to the reference wind turbine report with an overpowering of 5%. Regarding the structure model, the total mass natural frequencies of the blade were compared to the reference to validate the model before coupling.

The output from this simulation is summarized in the following points:

- For rigid simulation vs FSI case, the generated power and thrust are slightly reduced in FSI cases than the rigid one, the flap-wise deflection, edgewise deflection, and torsion are 5.57 m, 0.62 m, and 0.35° respectively.
- The output power in the case of the coned rotor is increased due to the increase of rotor effective diameter compared to the effective diameter of the non-coned case which suffers from flap-wise deflection
- In the case of shaft tilt, the output power is decreased due to the reduction in the effective rotor area.
- Under yawed inflow, the output power and thrust were almost the same in cases of rigid and FSI case. However, there was a phase shift between both cases. When the power in inflow cases was compared to yawing case, there was a reduction of 25%.
- The previous cases were simulated again after adding the gravity force.

Another study was implemented by Foti et al. [58] to show the wind turbine nacelles effect in wind farms by applying large eddy simulation (LES). The model was simulated with and without the nacelles and it was found that the existence of the nacelles resulted in increasing the fluctuation of power and turbulence intensity.

Yu and Kwon [59] applied FSI to investigate blade response due to yaw misalignment. The reference wind turbine was also NREL 5 MW. It was concluded that blade aerodynamic loads and deformation were increased due to yaw misalignment.

Heinz et al. [60] investigated the behavior of the wind turbine blade when the yaw system is not able to rotate towards the wind. He applied FSI at different wind speeds and angles to study blade edgewise vibration and tip displacement. It was found that peak to peak of edgewise vibration was 5 m at maximum wind speed, maximum inclination angle, and no yaw rotation.

2.2.2.2 Tower effect:

The effects of turbine components on turbine performance were also studied by Hsu et al.[61], in that paper, a 3D FSI simulation of the wind turbine was performed in the presence of nacelle and tower. The effect of these components was compared to the case of rotor only.

The thickness of the first layer around the blade was 0.02 m with a growth rate of 1.2 to generate 15 layers. The time step size was 2.5×10^{-4} s for all studied cases.

Three cases were covered in that study:

- 1- The rotor only was simulated and the entire fluid domain was rotating

- 2- The rotor only was simulated and the rotating fluid subdomain housed it. The rotating domain was enclosed by a stationary fluid domain.
- 3- Same as case 2; however, the nacelle and tower were included in the stationary domain.

From this paper, the following information was found:

For rigid case, there was no difference in generated torque in case of rotating the entire domain or sliding inside stationary one. However, in the case of including the tower, a dip in generated torque was found when the blade passed the tower.

In the case of FSI simulation, there was a high-frequency oscillation in the generated torque compared with the rigid body. Also, the effect of the tower on the aerodynamic torque is presented. The presence of the tower caused a drop in the aerodynamic torque which created a cyclic loading on the blade that was important for fatigue analysis. [61]

In Imiela et al. [62] study, the used turbine model is NREL 5 MW [29]. There two types of studies applied on wind turbine:

- A full-scale wind turbine including tower, nacelle, and rotor was modeled and the effect of the tower on the generated power was studied. This power was compared to the rotor-only case and reference turbine report.
- Comparing between the output power of rotor only in rigid and FSI cases.

The geometry was built using CATIA V5, then Pointwise software was used in mesh generation. The CFD solver was TAU-Code [63] which was developed at the Institute of Aerodynamics and Flow Technology. FEA model

was performed using Hypersizer [64] and the data were coupled by SIMPACK.

The results from this research were:

- The torque resulted from the flexible simulation was slightly higher than the rigid one by 2.2%. While the rigid cases were higher than the reference power by 4.12%

	Rigid	Flexible	Reference
Torque (kN.m)	4373	4469	4200

- The generated torque in the case of full turbine simulation is lower than the rotor case by 1% due to tower shadowing [62]

	Full turbine	Rotor only
Torque (kN.m)	4394	4448

The effect of the tower was also studied with respect to the noise. Madsen et al. [65] showed that the unsteady wakes behind the tower due to interaction between blades and tower led to an increase in low-frequency noise of the turbine. Moreover, Zahle et al. [66] simulated a downwind turbine and studied the effect of the tower on generating impulses in applied forces on the blades due to tower wakes.

2.2.2.3 Gravity effect

A study by Bazilevs et al. [67], [68] performed FSI on the 5 MW [29] offshore horizontal axis wind turbine at full scale with 61 m blade length and 2 m hub radius. The blade is divided into three portions, the first part is cylindrical then DU airfoils up to 44.5 m from the blade root. After that NACA airfoils are used up to the blade tip. The fluid domain mesh consists of 1416782 tetrahedral elements and 7680 triangles on the surface. To refine the mesh near

the blade surface, 15 layers around the surface with a first layer height of 10 mm and 1.1 growth rate are generated. The first part of the research was preparing the CFD model in a rigid case and validated the aerodynamic torque against the reference report of the turbine[67]

Part II of the research [68] was focused on applying FSI to the turbine. For the FE model, the bending strips method is used which is a unidirectional bending stiffness imaginary material and its bending stiffness is transverse to the areas interface [69]. Fiberglass epoxy composite with different fiber orientations is considered to increase the blade flap-wise and edgewise stiffness. Wind velocity was 11.4 m/s, the rotational speed is 12.1 rpm and the time step was 0.0003 s. The output from this simulation is summarized in the following points:

- Aerodynamic torque for rigid and flexible cases is compared with the steady-state case of the reference turbine. The torque in the FSI case is lower with higher frequency than the rigid case.
- The twist angle increased from the root to the tip.
- The maximum flap-wise deflection was 6 m.
- Due to gravity, the edgewise deflection and twist angle was decreased significantly at the lowest vertical position of the blade.

Another FSI research was done by Santo et al. [70] to study the effect of gravity force on load and performance at different blade positions and compare between FSI simulations with and without gravity. A full-scale wind turbine was simulated in a rotating domain with a 52 m diameter and length of 12 m to enclose a 50 m rotor. The stationary domain dimensions were 5-times rotor diameter from sides, top, and front of the rotor. The outflow was 15 times rotor diameter away from the rotor.

CFD mesh was composed of 13M cells and $k - \varepsilon$ turbulent model was applied. While the FE model was made of composite material with blade mass exceeding 9 tons and validated against manufacturer data through its first flap-wise and edgewise mode shapes. CFD and FEA models were coupled by an in-house code called Tango [71].

The results from this research were showing higher bending moment when the blade position was pointing upwards than the bending moment in the case of the downward position.[70]

The gravity force effect was also introduced by Santo et al. [72]. He applied FSI on a 50 m long fiberglass blade and presented the contribution of gravity force to the total bending moment. It was found that the maximum effect of gravity was introduced when the blade was vertically up; however, the axial force was the main source of the bending moment

2.2.3 Material design

A FSI study by Krawczyk et al. [73] was performed on a 2D NACA 4412 profile. The goal of this study was to assess the airfoil behavior due to aerodynamic loads at different wind speeds and material elasticity. In this research, ANSYS CFX and Mechanical were used for fluid and structure simulation and coupled together with ANSYS coupling module.

There were 18 cases investigated which were a combination of three young's modulus used at six wind speeds. The outcome of these cases is summarized in the following conditions relative to the rated one (Figure 2-7):

- Part load (wind speed is less than the rated one): the blade has better performance in the FSI case than the rigid case. The best part load case performance was in the lowest modulus of elasticity case.

- Overload (wind speed is higher than the rated one): the blade suffered from lower performance in the FSI case than the rigid case. The worst overload performance was for the least young's modulus [73].

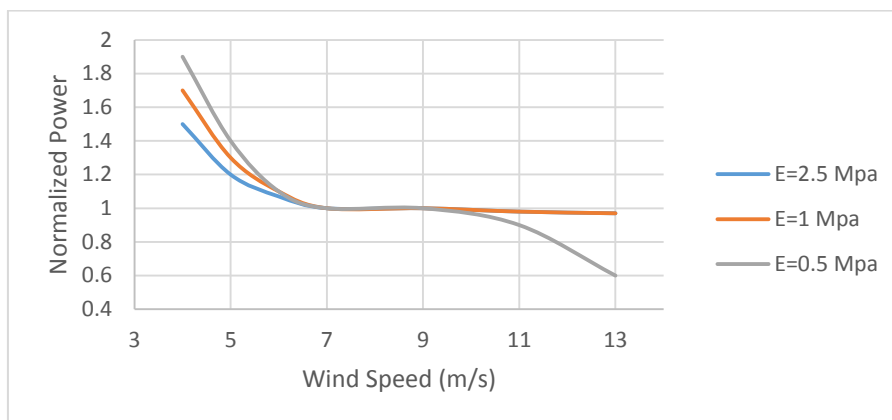


Figure 2-7 Blade performance at different loads and materials [73]

Also, the FSI was applied in Lee et al.[74] research by placing forces calculated by BEM theory on the FE model generated in Abaqus. According to the tip displacement and rotation angle of the blade, the generated power was calculated again using the BEM method.

The reference turbine power was 2 MW and 1.5 MW at a wind speed of 25 m/s and 10 m/s respectively. The new calculated power by BEM theory after considering FSI deformation was 1.66 MW for the wind speed of 25 m/s and 1.3 MW for the 10 m/s case.

The author proposed 3 methods to enhance the generated power:

- Pre-twist of blade geometry
 - o After applying FSI on the blade, a modification was applied to blade geometry according to twist angle data to improve the output power during normal operation.
- Pitch angle control

- Changing blade pitch angle according to twist data will improve the power partially due to different twisting angles at each airfoil section.
- Fiber orientation
 - The output power was enhanced by 11.5% over the original one (1.66 MW) after changing the fiber orientation of the spar cap from 0° to 20° towards the leading edge. [74]

2.2.4 Optimization:

Wind turbine optimization could be categorized in four main areas as stated in [75]:

- Reducing the cost of generated energy by decreasing the total annual cost which causes some restrictions on the rotor design and increasing the annual energy production. Regarding the offshore wind turbine, the cost of the rotor is not governing with respect to foundation and cable cost. Accordingly, larger rotors are designed to gain more economical benefits.[76]
- Increasing energy generated annually by enhancing turbine aerodynamics to increase the produced power. The aerodynamics of the turbine could be improved by optimizing airfoil geometries and comparing the power with the original geometry using the BEM method [77], [78].
- Minimizing blade mass could be achieved by optimizing the thickness and location of spar caps layers and keeping at the same time the maximum blade span-wise deflection [79]. Also, Chen et al. [80] applied 1-way FSI on a 2 MW wind turbine to check the effect of reducing the thickness of blade parts and changing spar cap location. Due to these two schemes, the mass was reduced by 6.181% and

11.518% for reduced thickness and variable spar cap location cases respectively which is reflected directly in the blade cost.

- Multi-objective optimization by selecting two or more optimization techniques.

Also, one of the main methods used for wind turbine optimization is Bend-twist coupling (BTC). This method couples blade bending due to aerodynamic forces with the twist of the blade. The blade twist is responsible for changing the angle of attached and consequently changing the aerodynamic forces. BTC is achieved by two methods [81]:

- **Geometric coupling:**

In this type of coupling, the blade is swept from its tip. When the load is applied on this swept blade, the created moment causes the blade to twist about its span-wise axis [82]. As shown in Figure 2-8, the moment generated about blade span-wise axis from lift force at the tip due to the swept blade results in twisting the blade [83].

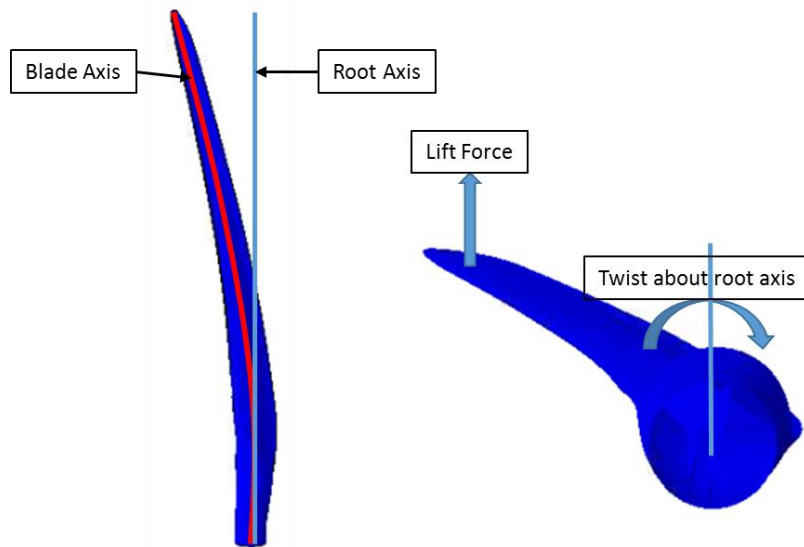


Figure 2-8 Geometric Coupling [83]

- **Material coupling:**

This kind of BTC is achieved by changing the fiber orientation of the blade's spar cap and /or skin to be away from the bending axis [81]. The concept of material coupling is based on the difference in composite material properties in each direction. Figure 2-9 illustrates the effect of fibers direction on top and bottom spar caps on achieving bend twist coupling or extension twist coupling. In the case of bend twist coupling, the fiber direction at the top and bottom is mirrored to make the blade twists due to bending load. While the blade will twist due to tension load in case of fibers are oriented in a helical layup [84].

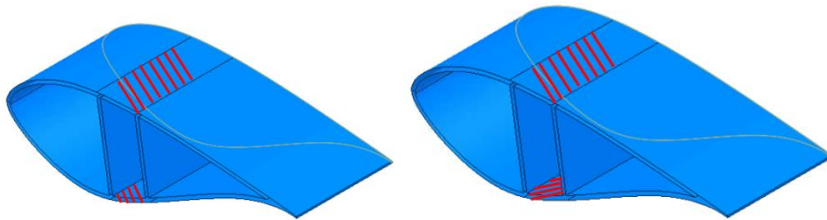
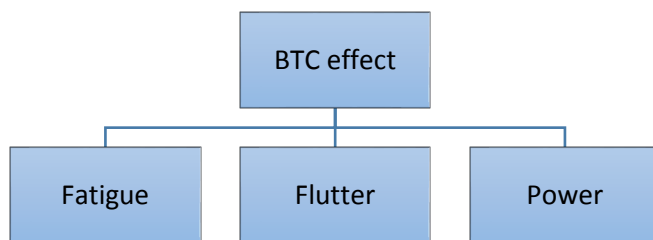


Figure 2-9(a) Bend Twist Coupling (b) Extension Twist coupling [84]

2.2.4.1 BTC blade research categories:



BTC research was focused on optimizing blade fatigue, flutter, or power. The following part discusses the effect of BTC on blade performance regarding each loading type.

2.2.4.1.1 Fatigue loading:

BTC plays a role in reducing the fatigue loading effect on the blade. When aerodynamic load increases suddenly due to wind speed increase, the BTC blade twists as it bends resulting in reducing the angle of attack and aerodynamic force.

Meng et al. [85] studied the fatigue reduction because of BTC on NREL 5 MW [29] wind turbine blades using different fiber orientations (material coupling). Then, blade fatigue life was predicted and compared with the blade design life (20 years). BEM method was coupled with the structure model then static and modal analysis were applied using ANSYS and Matlab code to show the effect of BTC.

It has been concluded that:

- Static response and natural frequencies were changed at each fiber orientation
- BTC existence minimized peaks and valleys effect
- The predicted fatigue life of the blade was 26 years

Blade loads are controlled actively or passively. Although active control methods are effective, their price increase the total cost and system uncertainty. However, passive load control methods are simple, actuator free and cost-effective. This method is effective in fatigue load reduction by 1.6–2.9% when applied by Hayat and Ha on a 5 MW wind turbine [86].

Moreover, a study was performed by Chen et al. [87] to investigate the effect of material BTC on passive control and fatigue load reduction. Also, NREL 5 MW [29] wind turbine was considered as a reference blade with various spar cap fiber orientations from 5° to 45° . It was found that due to using BTC, a higher pitch angle was required to maintain the original power production at

high wind speed. Also, tension and flap-wise bending stiffness we reduced by increasing fiber angle. While torsional stiffness was increased. Moreover, the BTC effect on fatigue load reduction was investigated resulting in a 38% to 16% reduction out of the plan and in plan bending moment amplitude.

In Manolas et al. [88] research regarding the comparison between material and geometrical BTC effect on load reduction, he applied several different cases: 10^0 fiber orientation, 5^0 fiber orientation with 3m swept tip, active control only, and combination of material/geometrical BTC and active control. 10 MW was the reference turbine. As a result of these cases, blade mass increased by 1.23% and 0.33% in the case of material BTC only and material/Geometrical BTC respectively in order to compensate the stiffness reduction. Regarding damage load which is reflected on fatigue load, passive control design resulted in 7% load reduction, while active control reduced the load by 27%. In the case of the combination of active and passive control design, the reduction increased to 30.5%

2.2.4.1.2 Flutter instability

Flutter instability is not considered an issue for small horizontal axis wind turbines; however, the classical flutter became more important for modern wind turbines with huge rotors and flexible blades [89]. Although BTC is an important factor in reducing the fatigue load reduction, it may also cause dynamic instability. The blade remains stable and vibrations are damped as long as the blade is under the flutter limit. Once this limit is exceeded, the blade becomes unstable [90].

Hayat et al. [91] investigated the flutter behavior of 5 MW wind turbine using material BTC. Three BTC conditions were studied: changing the off-axis fiber angle, changing the angle, and replacing fiberglass with carbon fibers and the last one was a combination of the two cases and increasing the thickness of

some layers and reduce others. For the first case, the flutter speed was decreased by 5% but still 3.3 times higher than the rated speed. The flutter speed was increased by 7.6% and 9.5% for second and third cases because of using lightweight carbon fibers with high stiffness.

Shakya et al. [92] studied the material BTC effect on critical flutter speed using different symmetric and asymmetric laminates at spar cap or full blade. The mode shapes were validated against the four results of [29], [93]–[95]. It was shown that the critical flutter speed was increased by 40% compared to the reference blade in the case of unbalanced symmetric laminates applied on the whole blade section. While the critical flutter speed was increased by 100% of baseline speed for asymmetric distribution.

Zhou et al. [96] evaluated the flutter limit using linear and nonlinear analysis when applied on a 5 MW wind turbine. By increasing modern wind turbine size, the blades are subjected to large flap-wise deflection. So nonlinear analysis is required under normal operation. The results showed that when using BTC and applying nonlinear analysis, the predicted flutter limit was decreased by 23% with respect to the linear analysis case. Also, it was shown that there was no great influence of unbalanced laminate on flutter speed in nonlinear analysis cases.

2.2.4.1.3 Power

BTC model links bending moment with twist angle which is reflected in changing the angle of attack and leads to aerodynamic load reduction to minimize fatigue load but reduces the generated power also. Stäblein et al. [97] presented the effect of 10 MW wind turbine blade pre-twisting and how the power production of BTC blade was improved. The analysis was performed using the BEM method and nonlinear steady-state deformation. The proposed steps for blade pre-twisting are:

- Apply reference wind speed
- Calculate uncoupled blade angle of attack
- Calculate coupled blade angle of attack
- Calculate the difference between the angle of attack in both cases
- Add this difference to twist distribution of coupled blade
- Repeat starting from step 3 until the difference becomes zero

As a result of this study, The coupled and coupled-pitched cases captured more energy at low wind speed. While the pre-twisted case showed higher performance than the coupled-only case.

Stäblein and Hansen [98] investigated the effect of turbulence on DTU 10 MW wind turbine [99] generated power. Bend twist coupling was applied by modifying the stiffness matrix as introduced by Stäblein et al. [97] and pre-twisting the blade to reach the same angle of attack of the uncoupled reference wind turbine. This study compared the generated power by uncoupled with a coupled pre-twisted blade in case of uniform inflow and high turbulence (class A) inflow as identified by IEC 61400-1 [100]. The turbulence effect was different with each wind speed. Below 11 m/sec wind speed, turbulence led to power loss in coupled case. However, at 11 m/sec, the power loss was decreased. From 12 to 14 m/sec, the power was the same for coupled and uncoupled blades.

The aforementioned literature review shows that many studies have been conducted on FSI, but few of them worked on the blade optimization methods. The purpose of the current research is to develop FSI model for the NREL 5-MW wind turbine. The specific goals of the study are:

- 1- Use ANSYS Fluent [4] for the CFD model, Abaqus [5] for the FE model, and link between these models by MPC [6].
- 2- Validate the CFD model against the Jonkman [29] report of the blade

- 3- Validate the FE model against Sandia [101] report and previous studies
- 4- Compare between the results of 1-way coupling and 2-way coupling simulations
- 5- Study the effect of centrifugal force on blade deformation
- 6- Study the impact of load combination of wind, gravitational, and centrifugal loads on blade deformation
- 7- Optimize the blade by creating a material BTC simulation to protect it from fatigue loading and stall
- 8- Propose an optimization method by increasing the fixation area at the blade root

Chapter 3 Model setup

3.1 NREL 5-MW Wind Turbine main properties

National Renewable Energy Laboratory (NREL) has developed the conceptual design of the 5-MW off-shore horizontal axis wind turbine.

Jonkman et al. [29] developed the 5 MW wind turbine with properties summarized in Table 3-1. In order to generate the rated electrical power of 5 MW with generator efficiency of 94.4%, the mechanical power should be 5.3 MW.

Rating	5 MW
Configuration	3 Blades
Rotor Diameter	126 m
Hub Diameter	3 m
Hub Height	90 m
Cut in, Rated, Cut out Wind Speed	3 , 11.4 , 25 m/s
Cut in, Rated Rotor Speed	6.9 , 12.1 rpm
Tip Speed at Rated Speed	80 m/s
Overhang	5 m
Shaft Tilt	5 degree
Pre-cone	2.5 degree

Table 3-1 NREL 5-MW Wind Turbine main properties [29]

3.2 Blade geometry

The blade consists of eight different airfoils as shown in Figure 3-1. Two cylindrical shapes at the root side. The other six airfoils consist of DU (Delft University) and NACA (National Advisory Committee for Aeronautics) shapes.

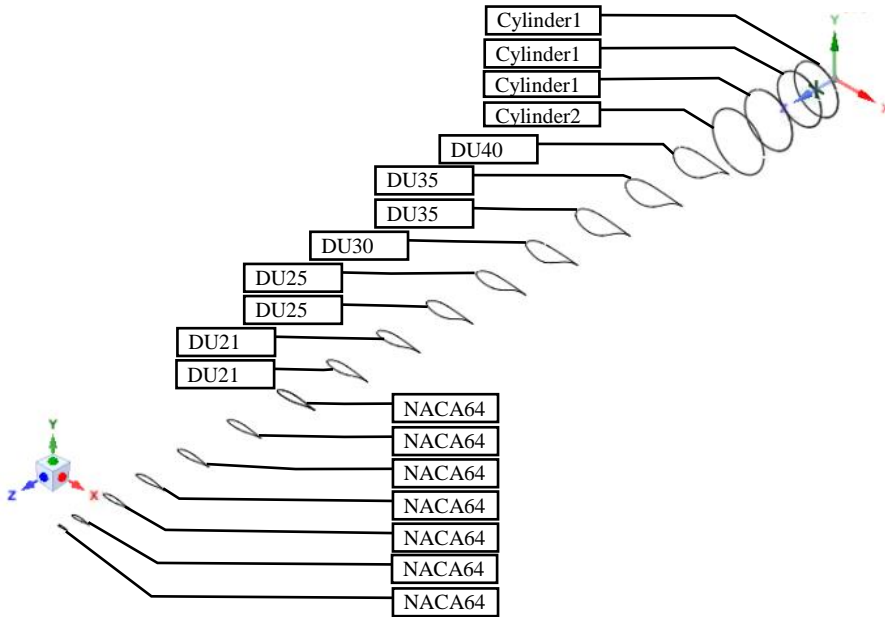


Figure 3-1 Blade Geometry

3.3 Blade CAD Model

The 3D CAD model of the blade was generated using ANSYS SpaceClaim [102]. Each airfoil is drafted using its coordinates then scaled according to the Chord length. After that, each airfoil is twisted along the blade span. Finally, the blade surface was generated by lofting the airfoils. Table 3-2 lists the location, chord length, and twist angle of each cross-section as extracted from Sandia reference report [101]. The aerodynamic center of each section is at $0.275 \cdot \text{Chord}$ and $0.5 \cdot \text{Chord}$ for airfoil and circular shaper respectively.

Blade span (m)	Rotor Radius (m)	Twist (deg)	Chord (m)	Airfoil Table
0	1.5	13.308	3.386	Circular
0.5	2	13.308	3.386	Circular
1.3667	2.8667	13.308	3.386	Circular

6.8333	8.3333	13.308	4.167	Circular
10.25	11.75	13.308	4.557	DU40_A17
14.35	15.85	11.48	4.652	DU35_A17
18.45	19.95	10.162	4.458	DU35 A17
22.55	24.05	9.011	4.249	DU30 A17
26.65	28.15	7.795	4.007	DU25 A17
30.75	32.25	6.544	3.748	DU25 A17
34.85	36.35	5.361	3.502	DU21 A17
38.95	40.45	4.188	3.256	DU21 A17
43.05	44.55	3.125	3.010	NACA64 A17
47.15	48.65	2.319	2.764	NACA64 A17
51.25	52.75	1.526	2.518	NACA64 A17
54.6667	56.1667	0.863	2.313	NACA64 A17
57.4	58.9	0.370	2.086	NACA64 A17
60.1333	61.6333	0.106	1.419	NACA64 A17
61.5	63	0	1.0855	NACA64 A17

Table 3-2 NREL 5 MW blade Airfoil properties [101]

The blade is divided into four main zones. As shown in Figure 3-2, the blade zones are leading edge, trailing edge, spar caps, and shear webs. The spar cap width is 600 mm and its center is at $0.5 \cdot \text{Chord}$ and $0.4 \cdot \text{Chord}$ of the circular and airfoil sections respectively.

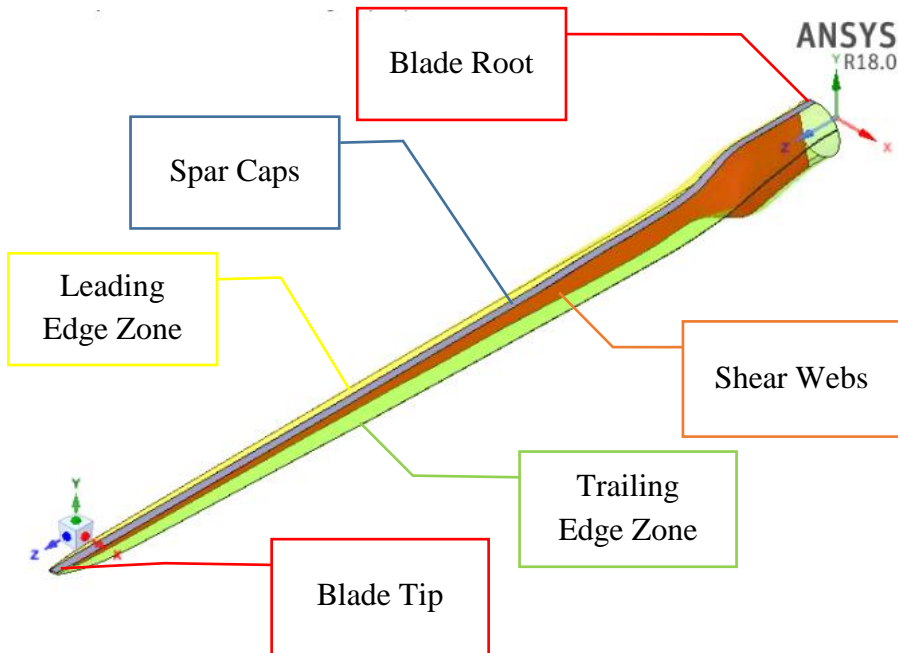


Figure 3-2 Blade main zones

3.4 CFD model

3.4.1 Fluid Domains

The fluid domain is generated using SpaceClaim [102] by creating rotating and static domains around the blade to simulate air behavior at the wind turbine. One-third of the full cylindrical domain with an angle of 120 deg. is used to reduce the number of mesh cells and simulation time. The inner rotating domain is created after excluding the blade volume from it at 15 m upstream and downstream the blade with a radius of 75 m. While the static domain is modeled at 5*rotor diameter and 10*rotor diameter upstream and downstream the wind turbine respectively with a radius of 150 m. Each surface and volume is identified with a unique name to be used in the boundary conditions definition. As shown in Figure 3-3 and Figure 3-4, each fluid domain is divided into surfaces, interface surfaces, and volumes.

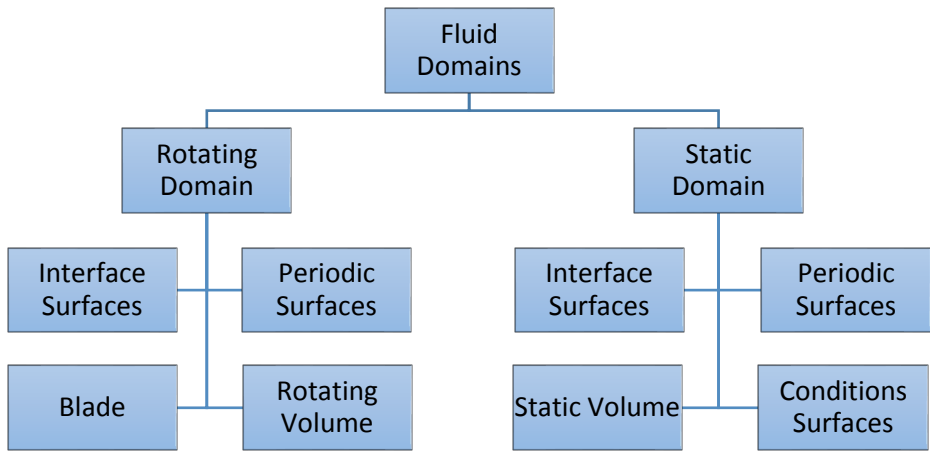


Figure 3-3 Breakdown of Fluid Domains

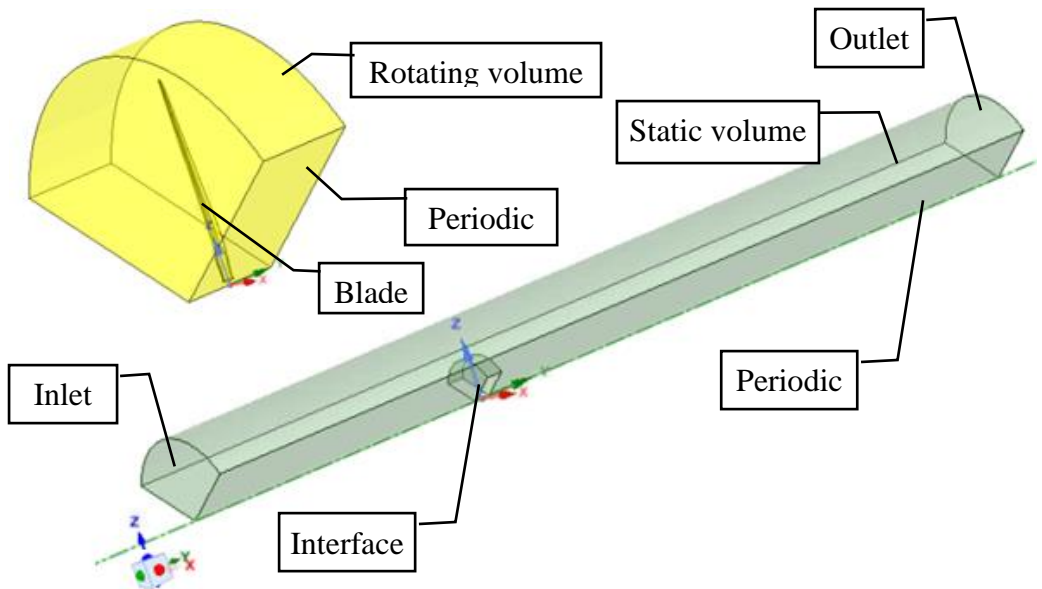


Figure 3-4 Surfaces and Volumes Identification

3.4.2 CFD Mesh

CFD model grid is built using ANSYS meshing module. Fine mesh is selected to get accurate results but it led to an increase in computational time. A combination of 4 Nodes Linear Tetrahedron (Tet4) and 6 Node Linear Wedge (Wed6) are used. In addition, 20 layers are extruded around the blade surface with an initial height of 2×10^{-5} m and a growth rate of 1.2 to control the Y^+ value. In order to reach mesh independence, different mesh densities are generated by increasing the number of cells until the change in results becomes minor. This part will be discussed in the subsequent section. The rotating domain grid is shown in Figure 3-5, while the surfaces are named as defined in 413.4.1. The average skewness of the generated grid is 0.22 and the average orthogonal quality is 0.78.

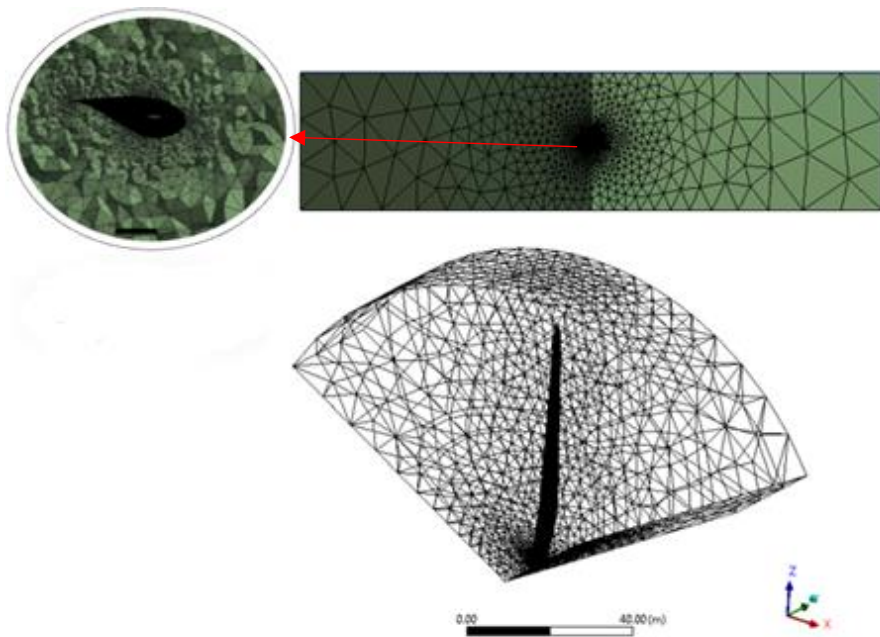


Figure 3-5 CFD grid of the rotating domain

3.4.3 CFD Model Setup

The generated grid is imported to ANSYS Fluent [4] to prepare the simulation model. Pressure based flow solver is selected which is developed for a low-speed incompressible fluid. This numerical method is based on developing the pressure equation from continuity and momentum equations [103]. Regarding the selected turbulence model, $k - \omega$ SST turbulence model gave suitable and stable results that matches the reference data. It is assumed that the flow is steady state, the air is incompressible with a density of 1.225 kg/m^3 and its viscosity is constant with a value of $1.7894\text{e-}05 \text{ kg/m.s}$. The rotating domain is defined as a moving frame with 12.1 rpm. The inlet velocity at the inlet surface of the static domain is 11.4 m/s, the interface and periodic surfaces are identified. The dynamic mesh section is defined because of mesh deformation during FSI simulation.

3.4.4 Mesh Independence

Mesh independence study is essential to distinguish whether the results are affected by mesh resolution. In order to implement this study, the simulation is run with initial mesh resolution till it converges. Then the mesh is refined and compare the simulation results with the previous one. This step is repeated until the change in results becomes negligible. In this research, the reference result is the total aerodynamic power generated from the turbine. The simulation is applied on 2.13 M, 2.60 M, 3.12 M, 3.57 M, and 4.06 M cells until the difference between the two successive simulations is less than 0.5%. Table 3-3 and Figure 3-6 indicate the values of generated power at each grid. It is shown that the difference in generated power for 3.57 M and 4.06 M

cells is 0.44%. Accordingly, the grid of 3.57 M is the suitable one as it gives accurate results at the minimum computational time.

No. of cells (M)	Power from CFD (MW)	Difference %
2.13	4.999	
2.60	5.237	4.76
3.12	5.365	2.44
3.57	5.482	2.20
4.06	5.506	0.44

Table 3-3 Generated Power Values At Each Grid

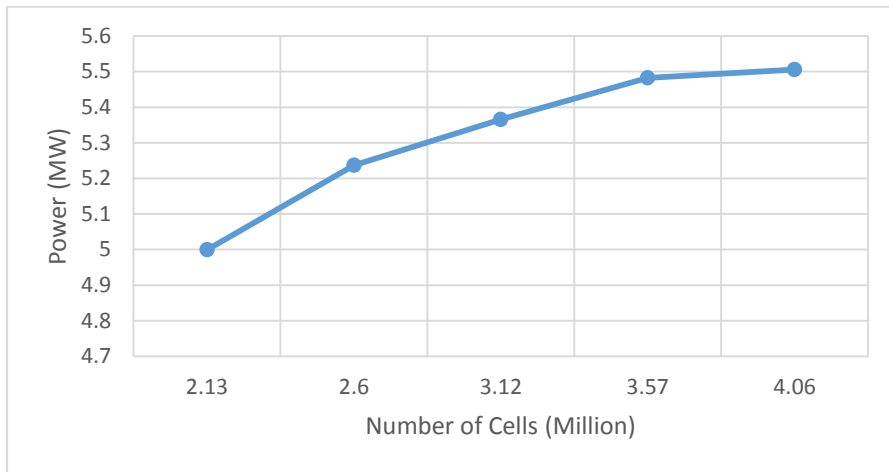


Figure 3-6 Generated Power (MW) VS Number of Cells

3.5 FE Model

3.5.1 Composite material layup and mechanical properties

The NREL 5 MW wind turbine blade is used in many studies. The main aerodynamic report of the blade was developed by Jonkman [29] and the structural mode shapes were modeled by Sandia National Laboratory (SNL) [101]. The composite materials used in the blade structure are:

- Gelcoat

- E-LT-5500 (UD): Uniaxial fiberglass at 0° fiber orientation with respect to the span axis
- SNL (Triax): Uniaxial and Double Bias fiberglass at 0° and $\pm 45^\circ$ fiber orientation with respect to the span axis
- Saertex (DB): Double Bias fiberglass at $\pm 45^\circ$ fiber orientation with respect to the span axis.
- Foam
- Carbon(UD): Uniaxial Carbon Fibers at 0° fiber orientation with respect to the span axis

Table 3-4 summarize the mechanical properties and number of layers and thickness of each composite material used in blade structure where E is young's modulus, G_{ij} is shear modulus and ν_{ij} is poisson ratio.

	Layer Thickness	Lay-up	E_1	$E_2 = E_3$	G_{12} $= G_{13}$ $= G_{23}$	ν_{12} $= \nu_{13}$ $= \nu_{23}$	Density
	mm		MPa	MPa	MPa	-	Kg/m ³
Gelcoat	0.05		3440		1380	0.3	1235
E-LT-5500 (UD)	0.47	[0] ₂	41800	14000	2630	0.28	1920
SNL(Triax)	0.94	[±45] ₂ [0] ₂	27700	13650	7200	0.39	1850
Saertex(DB)	1	[±45] ₄	13600	13300	11800	0.49	1780
Foam	1		256	256	22	0.3	200
Carbon(UD)	0.47	[0] ₂	114500	8390	5990	0.27	1220

Table 3-4 Summary of material properties [101]

As shown in Figure 3-7 and according to [95][101][87], the composite materials are distributed along blade span and cross-section. The figure

shows the composite material layup and fiber orientation; however, the shown thickness is not to scale. The leading edge and trailing edge panels layup consist of SNL (TX) $[\pm 45]_2 [0]_2$, Foam, SNL (TX) $[\pm 45]_2 [0]_2$, and Gelcoat. Trailing edge reinforcement consists of SNL (TX) $[\pm 45]_2 [0]_2$, Foam, E-LT-5500 (UD) $[0]_2$, SNL (TX) $[\pm 45]_2 [0]_2$ and Gelcoat. While the cap layup is the same as panels but the Foam is replaced with Carbon (UD) $[0]_2$. For shear webs, the layup is Saertex(DB) $[\pm 45]_4$, Foam and Saertex(DB) $[\pm 45]_4$. In order to strengthen the blade root to resist high stresses near the hub, extra SNL (TX) $[\pm 45]_2 [0]_2$ is added.

3.5.2 FE model setup

The CAD model is extracted from SpaceClaim [102] and imported into Abaqus [5] to create the FE model. In order to prepare the FE model for FSI analysis, the following steps are followed:

- The surfaces of the blade that will be coupled with the CFD model are defined
- Each composite material is associated with its related part of the blade as defined in 3.5.1
- A static, general step is created
- The boundary conditions are defined by fixing the blade from its edge at the root. Velocity in X, Y, and Z directions are 0, and moments about X, Y, and Z axes are 0
- The created mesh contains 32310 elements. 31660 elements are linear quadrilateral elements of type S4R and 650 elements are linear triangular elements of type S3
- Input file for the generated FE model is exported to be inserted in the FSI model.

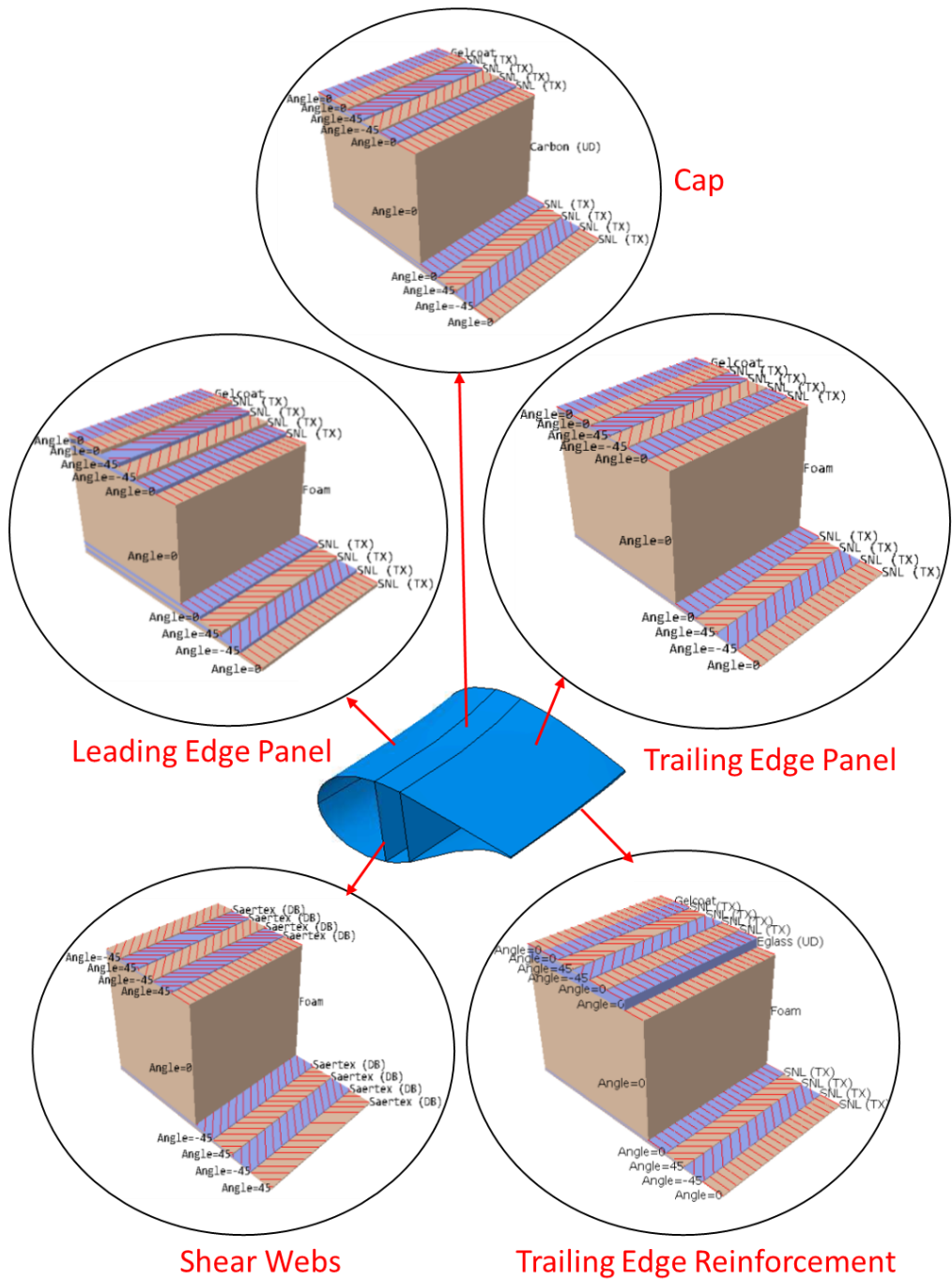


Figure 3-7 Composite material distribution along wind turbine blade cross-section

3.6 FSI Model

FSI is implemented by MPCCI [6] that exchanges the data between the CDF model and the FE model. Each system of the coupled system has its governing equations and the common variables between them are exchanged [104]. As explained in 2.1, there are two schemes of FSI, 1-way coupling, and 2-way coupling. Also, the 2-way coupling is divided into strong and weak coupling. The strong coupling requires solving all governing equations which are difficult and increases computational time. While in the weak coupling, each system is solved separately then some information is exchanged between these systems. This approach is less accurate than strong coupling [105].

The quantities are transferred between the models through two processes:

- Association: in this process, each cell in one system is linked to its partner in the other system
- Interpolation: the quantities are transferred between associated cells in both systems. MPCCI considers the difference in mesh between CFD and FE models.

Running FSI model using MPCCI requires the following steps as defined in MPCCI documentation [105]:

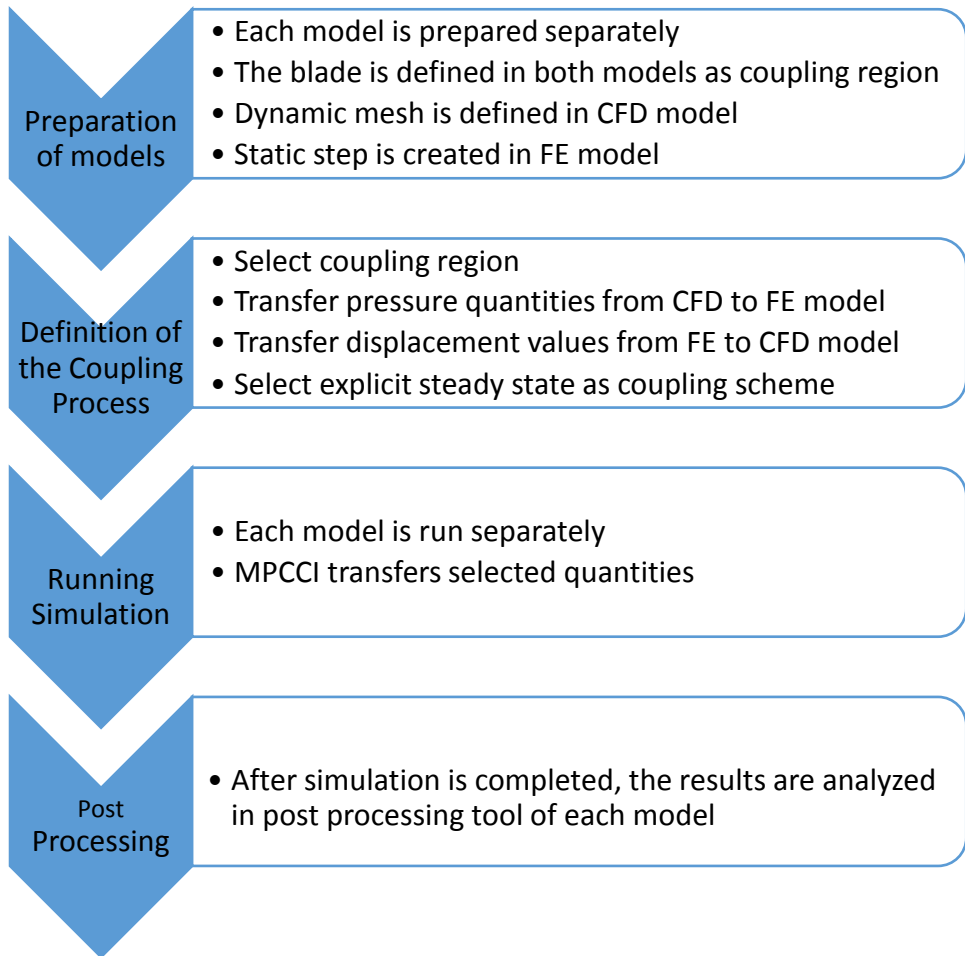


Figure 3-8 MPCCI Simulation Steps

Chapter 4 Results and Discussion

4.1 Introduction

This chapter discusses the results achieved from the simulation of CDF, FE, FSI models. Firstly, the CFD and FE models are validated separately before running the FSI model against the reference blade report and other studies applied to the wind turbine. Then, a comparison between 1-Way coupling and 2-way coupling is presented. Finally, blade optimization methods are proposed including fiber orientation and fixation method.

4.2 CFD model validation

The validation of the CDF model is performed at a wind speed of 11.4 m/s wind speed and rotor speed of 12.1 rpm. The results are compared against the blade tip velocity, turbine performance curve, and generated power at rigid and flexible cases.

4.2.1 Blade tip speed and relative velocity

According to Jonkman [29] report, the tip speed at the rated blade speed of 12.1 rpm is 80 m/s. As shown in Figure 4-1, the velocity vector along the blade span is increasing from the root to the tip with a value of 78.7 m/s.

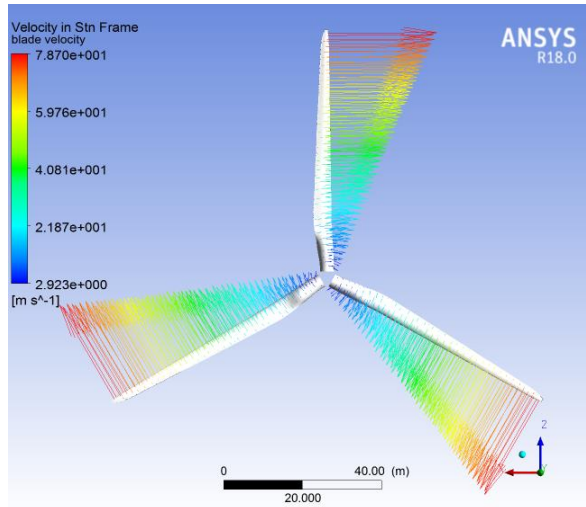
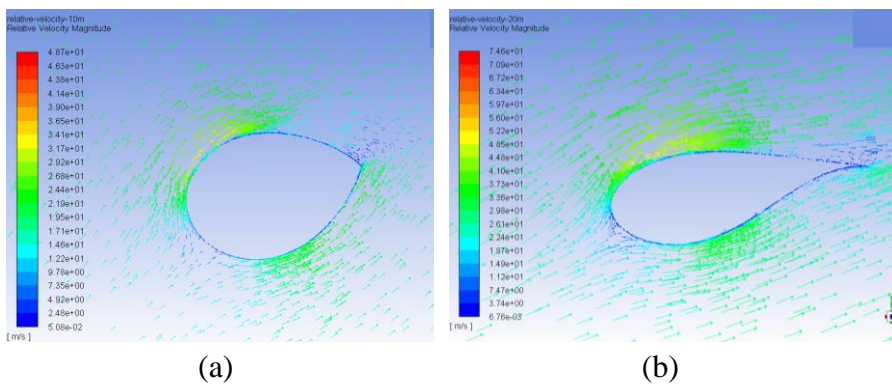


Figure 4-1 Blade Tip Speed

Also, the relative velocity vectors are presented at six cross-sections of the blade every 10 m showing the direction of relative velocity vectors at the blade leading edge, around its surface, and trailing edge. Figure 4-2 shows that the relative velocity vectors magnitude and direction at the blade at 10m, 20m, 30m, 40m, 50m, and 60m of the blade span



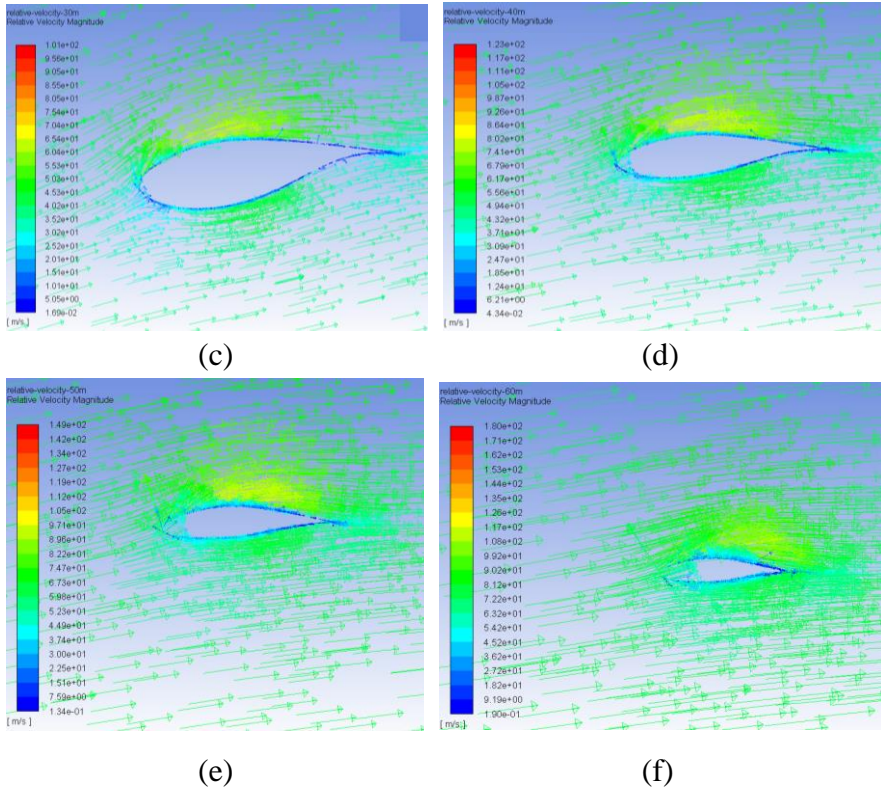


Figure 4-2 Relative Velocity Vectors Magnitude and Direction along the Blade Span at (a) 10m (b) 20m (c) 30m (d) 40m (e) 50m (f) 60m

4.2.2 Generated power at rated conditions

As one blade is simulated, the generated torque and power are multiplied by 3. Each blade generates 1442.21 kN.m and 1827.43 kW, so the total torque and power are 4326.63 and 5482.31 kW respectively. Table 4-1 presents a comparison between the generated power from the CFD model and Jonkman [29], Dose et al. [56], and Imiela et al. [62]. It is noticed that the aerodynamic power from the CFD model is higher than the reference value by 3.37% which is accepted. Also, the output power indicated in the other reference studies is higher than the reference value. The reason for this discrepancy could be that all information of the blade geometry is not

available such as the trailing edge shape. Moreover, the precone and tilting angles are not considered.

	Power (MW)		Difference %	
	Rigid	Flexible	Rigid	Flexible
Present study	5.482	5.647	--	--
Jonkman [29]	5.297	--	3.37	--
Dose et al. [56]	5.51	5.49	-0.51	2.78
Imiela et al. [62]	5.541	5.662	-1.08	0.26

Table 4-1 Comparison of generated power with other studies

4.2.3 Y^+ values

In order to solve the near-wall region, the first cell of the mesh shall be located in the viscous sublayer. This could be observed by limiting the $Y^+ \leq 1$. The Y^+ value is defined as:

$$Y^+ = \frac{yu_\tau}{\nu}$$

Where:

y = height of the first cell from wall

u_τ = friction velocity

ν = kinematic viscosity

The first layer height at the blade surface is 2×10^{-5} m with a growth rate of 1.2 to keep the Y^+ less than one. The overage Y^+ value extracted from the CFD model is 0.78.

4.2.4 Wind turbine operating curve

The other factor used to validate the CFD model is checking the aerodynamic power at different operating conditions and comparing it with the turbine performance curve. Table 4-2 shows the rotor rated power at each wind speed starting from the cut-in speed of 3 m/s to the cut-out speed of 25 m/s

Wind Speed	Power from CFD (MW)	Rotor Rated Power (MW)	Difference %
3	0.52	0.5	3.85
7.7	1.78	1.9	-6.74
10.3	4.2	4	4.76
11.4	5.482	5.297	3.37
15	5.1	5.297	-3.86
20	4.9	5.297	-8.10
25	4.87	5.297	-8.77

Table 4-2 Wind Turbine Performance Curve

4.3 FE model validation

The blade mode shapes and deformation are validated against the reference report [101], Shakya et al. [92], Hansen [93], Pourazarm et al. [95], and Jonkman [29]. The pressure distribution on the blade resulted from the CFD model is transferred through MPCCI to the FE model. Figure 4-3 shows the pressure difference between pressure and suction sides of the blade which is responsible for rotor rotation.

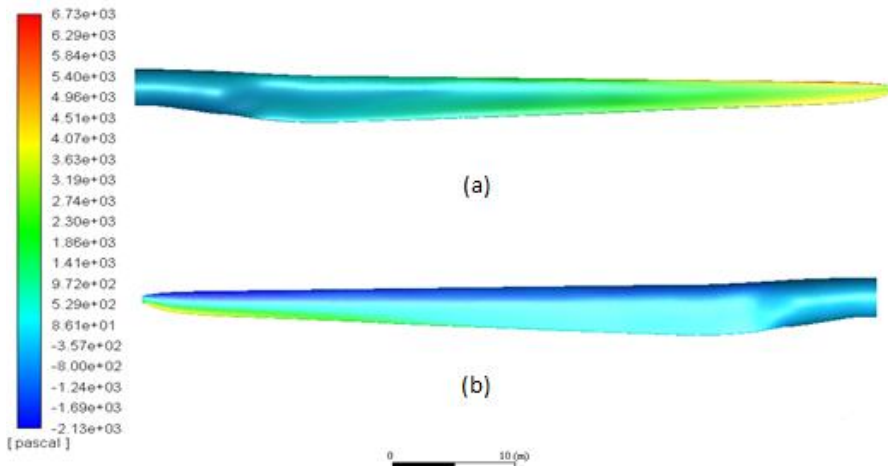
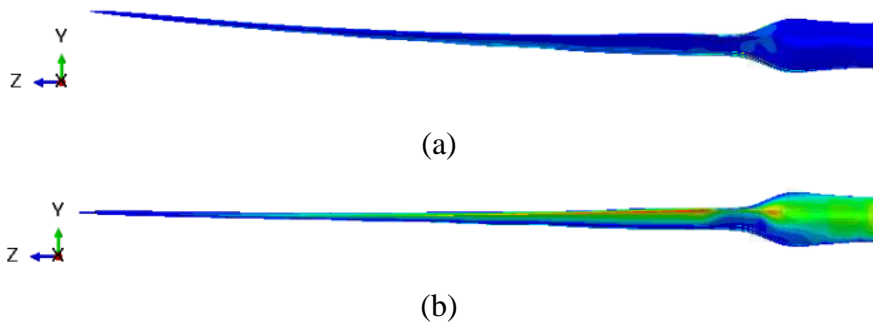


Figure 4-3 Pressure distribution on the blade

4.3.1 Mode shapes

Six mode shapes of the blade are extracted from Abaqus and compared with Sandia report. The report divided the mode shapes into 3 flap-wise bendings, 2 edgewise bendings, and 1 torsion as shown in Figure 4-4. As this blade is used in many studies, and each of them generated mode shapes values, the extracted values from Abaqus are compared with six references as illustrated in Table 4-4



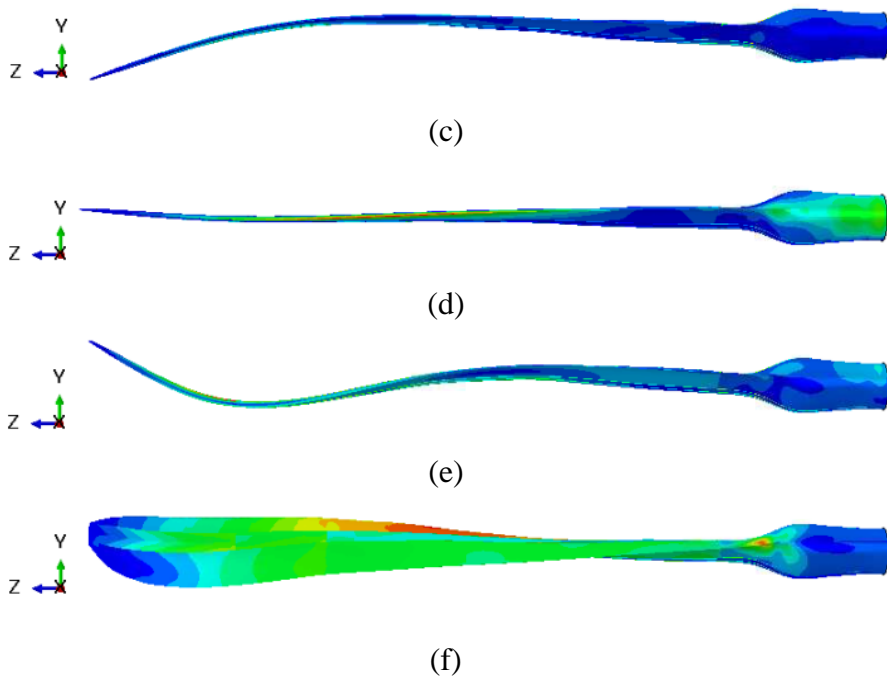


Figure 4-4 Blade Mode Shapes (a) First Flapwise (b) First Edgewise (c) Second Flapwise (d) Second Edgewise (e) Third Flapwise (f) First Torsion

Mode #	Description	Frequency (Hz)						
		Present Study	Sandia Report[101]	Shakya [92]	Hansen [93]	Meng [94]	Pourazarm [95]	Jonkman [29]
1	First Flapwise	0.62	0.87	0.69	0.69	0.72	0.64	0.69
2	First Edgewise	0.90	1.06		1.1	1.07	-	-
3	Second Flapwise	1.94	2.68	1.99	1.8	2.05	1.86	2.02
4	Second Edgewise	3.40	3.91	-	3.4	-	-	-
5	Third Flapwise	4.30	5.57	4.62	3.6	4.37	4.34	-
6	First Torsion	6.56	6.45	5.81	8	5.62	5.39	-

Table 4-3 Blade Modal Frequencies

Table 4-4 illustrates the modal frequencies of each mode shape generated in the present study and check that they present within double the standard deviation of the average. It seems that all mode

shapes lie within the reference values except the first and second mode shapes: however, they are near the reference ones and accepted.

Mode #	Present Study (Hz)	Average (Hz)	Standard Deviation	Average - 2*Standard Deviation	Average + 2*Standard Deviation
1	0.62	0.72	0.079	0.637	0.796
2	0.90	1.08	0.021	1.056	1.097
3	1.94	2.07	0.316	1.751	2.382
4	3.40	3.66	0.361	3.294	4.016
5	4.30	4.50	0.709	3.791	5.209
6	6.56	6.25	1.053	5.201	7.307

Table 4-4 Blade modal frequencies

4.3.2 Blade deformation

The other factor of the FE model validation is the blade deformation including the flap-wise deflection. The expected tip deflection as indicated in Sandia report is 6.03 m which will be compared with the flap-wise deflection in the FE model as this value is critical to protect the blade from hitting the tower. The report indicated that the allowable tip deflection is 7.07 m as the available clearance between the rotor and the tower is 10.5m and the safety factor is 1.485.

Wind load only is applied on the blade and the flap-wise deflection is compared with the 6.03m value. The one-way coupling scheme is chosen in the validation process as it is required to check the effect of applied load due to wind on blade deformation. Figure 4-5 shows the blade inplane (U1) and out of plan (U2) deflection by the applied load. The maximum flap-wise deflection at the tip is 6.055m with a

difference of 0.4%. Accordingly, this FE model is validated and will be used in the rest of the study.

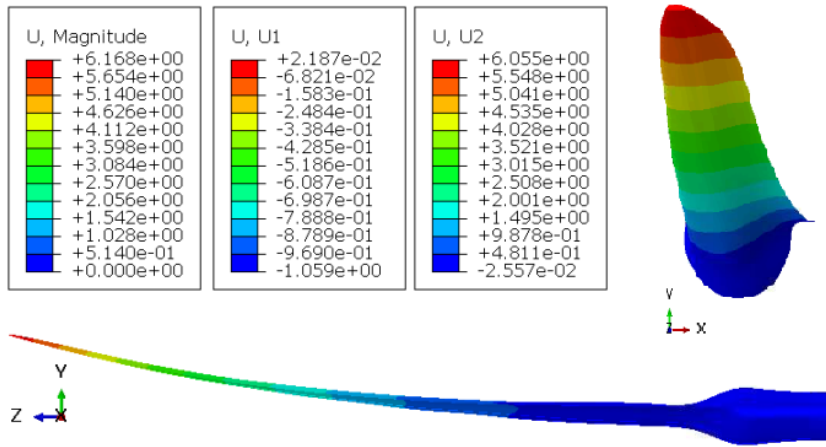


Figure 4-5 The Blade Flap-Wise and Edge-Wise Deflection

4.4 Comparison between 1-way and 2-way coupling

4.4.1 Wind Load Only

To study the behavior of the wind turbine during the normal operation, a 2-way coupling model is required as the data are exchanged between the FE and the CFD models and each one affects the results of the other. Although the computation time of the 2-way FSI models, the results should be more accurate near the actual performance of the wind turbine.

As shown in Table 4-5, there is a notable difference between 1-way and 2-way schemes. The main important difference is the flap-wise deflection which is about 0.85m as it gives extra clearance between the blade and the tower. Also, there is a reduction in edge-wise deflection and tip twist angle by 0.078m and 1.32 deg respectively. It seems that the edge-wise deflection is not highly affected by 2-way coupling.

FSI mode	Wind Load Only			
	Deformation (m)	Flap-Wise Deflection (m)	Edge-Wise Deflection (m)	Tip Twist Angle (deg.)
1-way	6.168	6.055	-1.057	-2.235
2-way	5.302	5.198	-0.979	-0.913

Table 4-5 Difference Between 1-Way and 2-Way Coupling

4.4.2 Wind Load, Gravitational Load, and Centrifugal Load

Two other forces, Gravitational and Centrifugal, affect the performance of wind turbines during normal operation in addition to the wind load. These forces depend on the blade mass and length. The centrifugal force acts radially and outward which is a function of rotational velocity squared, mass, and radius of the blade. However, the gravitational force effect depends on the position of the blade. These forces are applied to the FE model as shown in Figure 4-6. Both loads affect the flap-wise deflection at 0° and 180° positions while they affect the edgewise deflection at 90° and 270° positions.

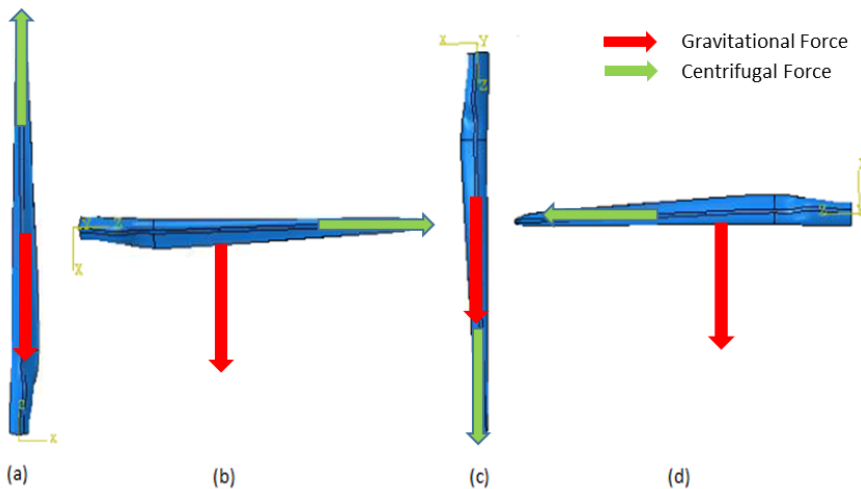
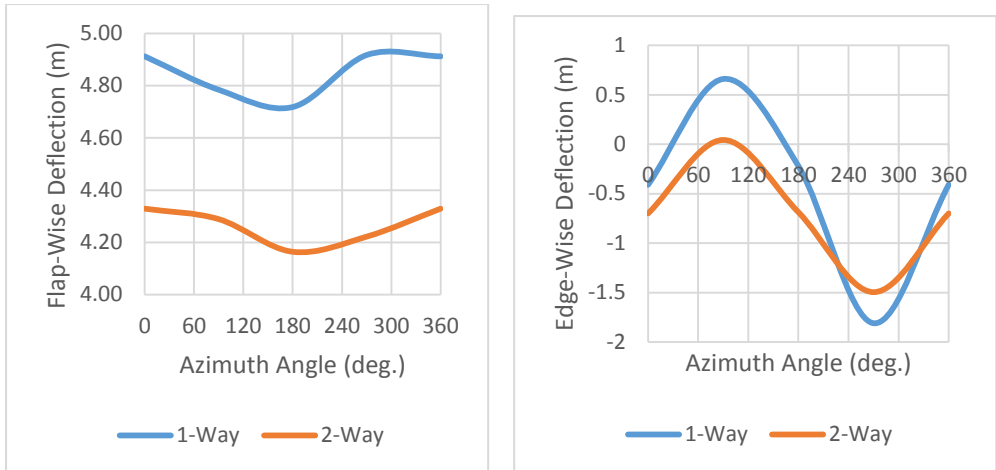


Figure 4-6 Applied gravitational and centrifugal loads at each blade position (a) 0° (b) 90° (c) 180° (d) 270°

As shown in Table 4-6 also compares the blade deformation in the case of 1-way and 2-way coupling after adding the load combination of wind, gravitational and centrifugal loads. The flap-wise deflection is reduced along with all positions of the blade. Also, both edge-wise deflection and tip twist angle at each position is decreased. In addition to the reduction in the magnitude, the amplitude of edge-wise and tip twist angle in one cycle is decreased. This reduction in deformation amplitude is shown in Figure 4-7, which affects the cyclic loading simulation.

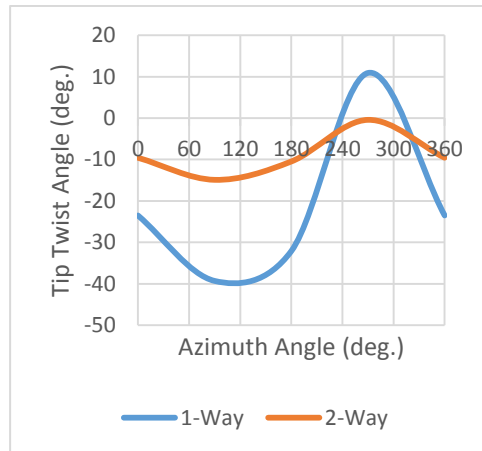
Wind Load + Gravitational Load + Centrifugal Load								
	1-Way				2-Way			
Azimuth Angle	Deformation (m)	Flap-Wise Deflection (m)	Edge-Wise Deflection (m)	Tip Twist Angle (deg.)	Deformation (m)	Flap-Wise Deflection (m)	Edge-Wise Deflection (m)	Tip Twist Angle (deg.)
	4.94	4.91	-0.41	-23.5	4.39	4.33	-0.70	-9.6
90	4.84	4.78	0.66	-39.3	4.30	4.29	0.04	-14.90
180	4.73	4.72	-0.22	-32.1	4.23	4.16	-0.69	-10.5
270	5.26	4.92	-1.81	10.9	4.49	4.22	-1.50	-0.4
360	4.94	4.91	-0.41	-23.5	4.39	4.33	-0.70	-9.6

Table 4-6 Difference between blade deformation at different azimuth angle, including the load combination



(a)

(b)



(c)

Figure 4-7 comparison between blade deformation during one cycle (a) Flap-wise deflection (b) Edge-wise deflection (c) Tip twist angle

4.5 Optimization

As discussed in section 2.2.4, the areas of optimization are achieved by reducing the cost of generated energy, enhancing turbine aerodynamics to increase power production, or reducing the cost of the blade by reducing its mass. Wind turbine blades could be optimized actively or passively. The active control is efficient but costly. The optimization could be achieved passively by modifying the blade

geometry or material without affecting the wind turbine performance. The goal of optimization is to protect the blade from damage either by environmental conditions or structural failure as explained in detail in 1.7. There are two optimization methods proposed in this study either by changing the fiber orientation or adding extra webs.

4.5.1 Optimization by changing the fiber orientation in the cap

This method is called bend twist coupling blade (BTC) which is based on changing the twist angle of the blade passively due to bending loads. BTC blade is achieved by changing the geometry or the fiber orientation of the blade as explained in section 2.2.4. The current study focuses on rotating the unidirectional fibers in the cap.

Unidirectional carbon fibers of the cap are originally placed in the same direction of the blade axis. In the present work, the carbon fiber of the cap in pressure and suction sides will be rotated off-axis by 5° , 10° , and 15° . As shown in Figure 4-8, the material layup of the cap is kept as it is SNL (TX) $[\pm 45]_2 [0]_2$, Carbon (UD) $[5/10/15]_2$, SNL (TX) $[\pm 45]_2 [0]_2$ and Gelcoat. Each fiber orientation is studied separately, and the effect of this change on flap-wise deflection, edge-wise deflection, twist angle, and output power is compared with the reference values. The FSI model is performed in steady-state at the rated wind speed and rotor speed.

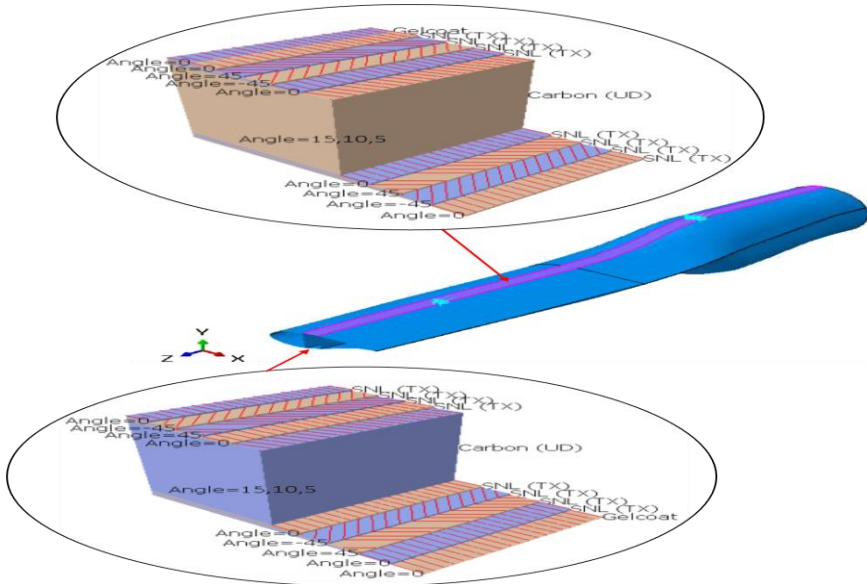


Figure 4-8 Carbon fibers orientation in the spar cap

As presented in Figure 4-9, the generated power due to using BTC is slightly reduced during the blade cycle; however, this power reduction is accepted to protect the blade from damage because of fatigue or stall.

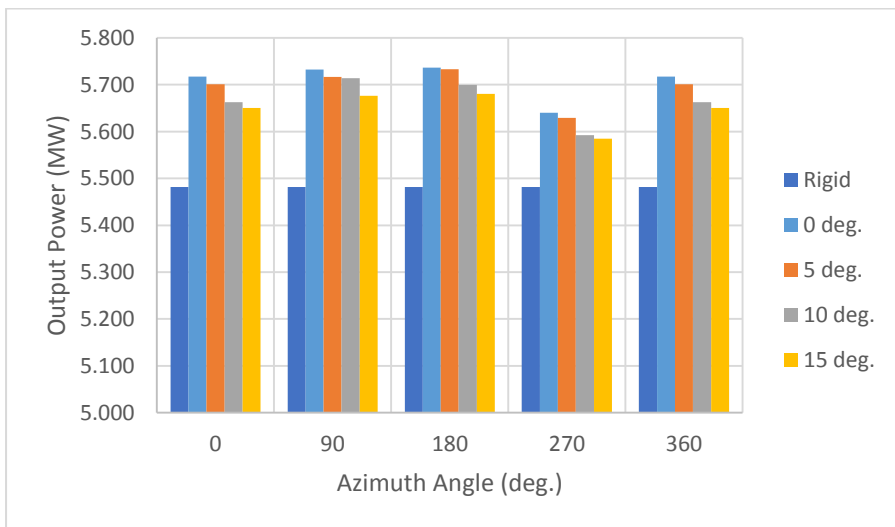


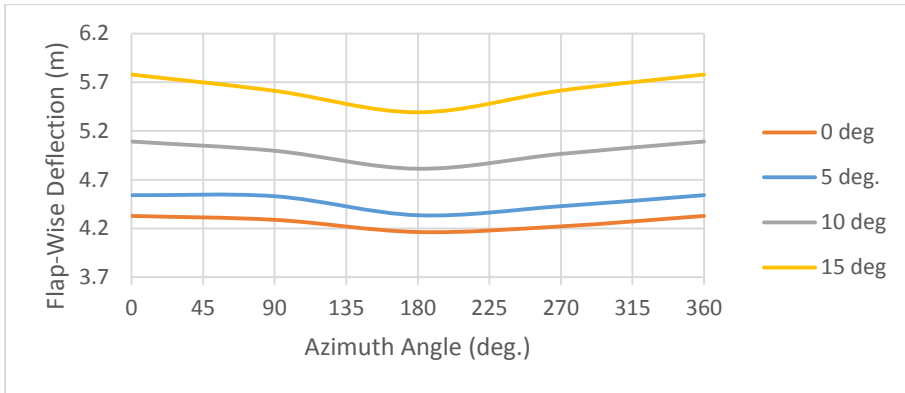
Figure 4-9 Output power with and without BTC

The cyclic tip deflection and torsion values of the BTC blade are presented in Table 4-7 and Figure 4-10, the blade longitudinal stiffness of the blade is reduced by increasing the fiber angle; however, the torsion stiffness is increased resulting in twisting the blade toward feather. Also, the peak-to-peak amplitude is reduced by increasing the angle from 0° to 15° which protects the blade from fatigue loading. Although the increase in fiber angle protects the blade from stall and fatigue, this increase is limited with the clearance between the rotor and the tower. Regarding the effect of the BTC blade on edge-wise deflection, the deformation is almost the same in all cases. Accordingly, 15° off-axis fiber orientation is considered the most suitable case due to the lowest twist angle and peak-to-peak amplitude. Moreover, Figure 4-10, Figure 4-11, Figure 4-12, Figure 4-13, and Figure 4-14 show the BTC blade deformation at different cross-sections of the blade to check that the effect of BTC appears along the blade span.

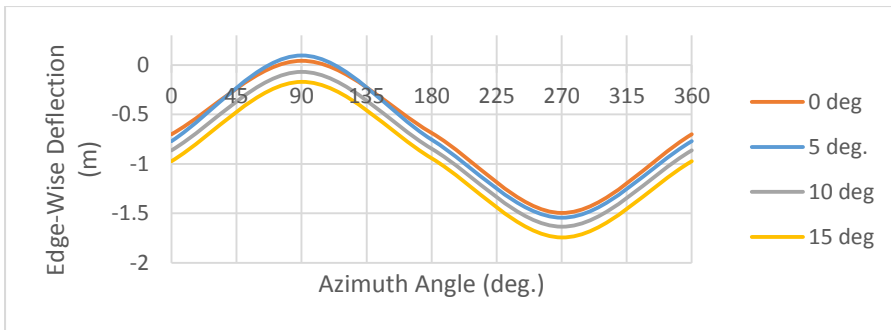
Carbon fibers angle (deg.)	Deformation (m)	Azimuth Angle (deg.)				
		0°	90°	180°	270°	360°
5°	Total (m)	4.615	4.539	4.408	4.697	4.615
	Flap-Wise Deflection (m)	4.542	4.531	4.336	4.429	4.542
	Edge-Wise Deflection (m)	-0.770	0.097	-0.754	-1.544	-0.770
	Tip Twist Angle (deg.)	-7.20	-19.21	-7.93	0.99	-7.20
10°	Total (m)	5.176	5.008	4.896	5.237	5.176
	Flap-Wise Deflection (m)	5.092	4.997	4.813	4.965	5.092
	Edge-Wise Deflection (m)	-0.863	-0.069	-0.846	-1.635	-0.863
	Tip Twist Angle (deg.)	-5.86	-12.71	-6.08	1.27	-5.86
15°	Total (m)	5.877	5.629	5.487	5.894	5.877
	Flap-Wise Deflection (m)	5.779	5.612	5.392	5.615	5.779

	Edge-Wise Deflection (m)	-0.973	-0.170	-0.943	-1.744	-0.973
	Tip Twist Angle (deg.)	-5.04	-10.75	-5.14	0.83	-5.04

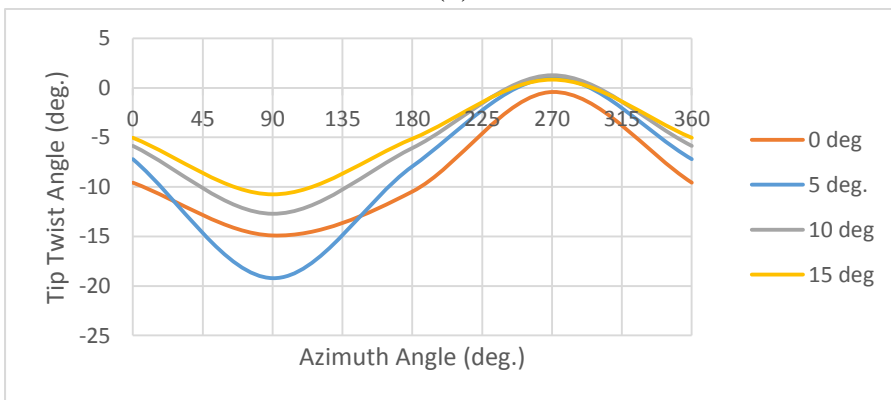
Table 4-7 BTC blade deformation



(a)

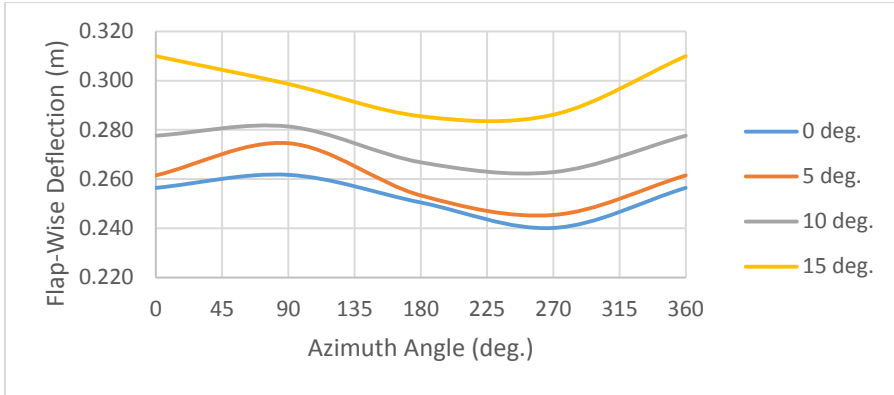


(b)

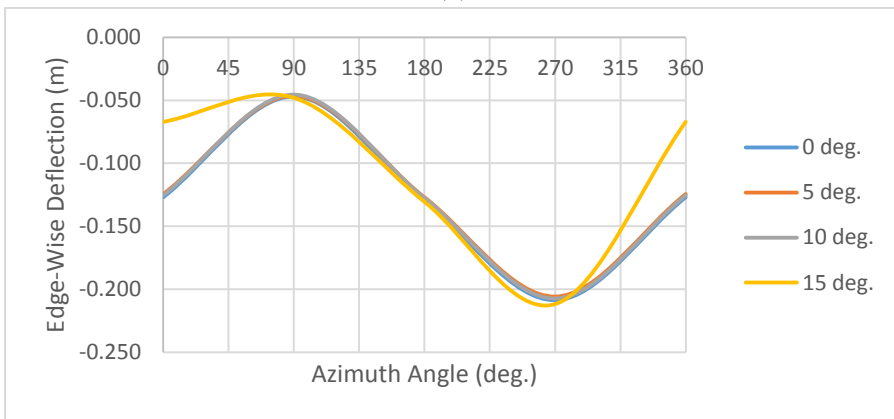


(c)

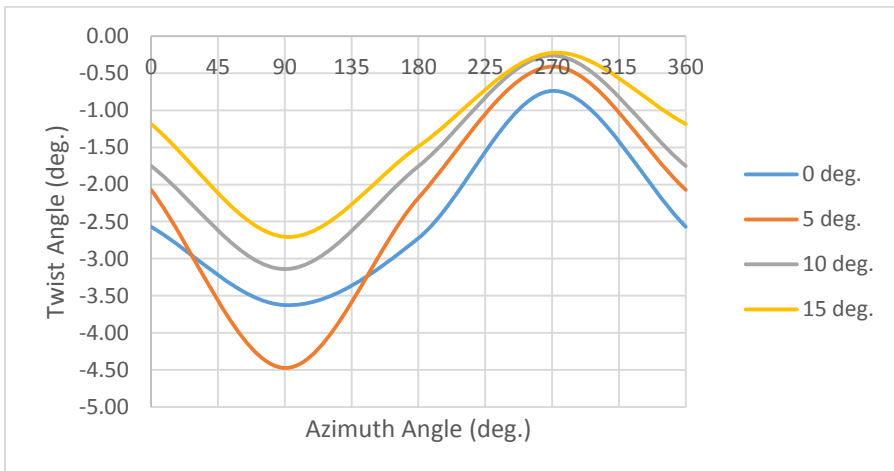
Figure 4-10 Blade deformation at the tip for 0,5,10,15 carbon fiber orientation (a) Flap-wise deflection (b) Edge-wise deflection (c) Twist angle



(a)

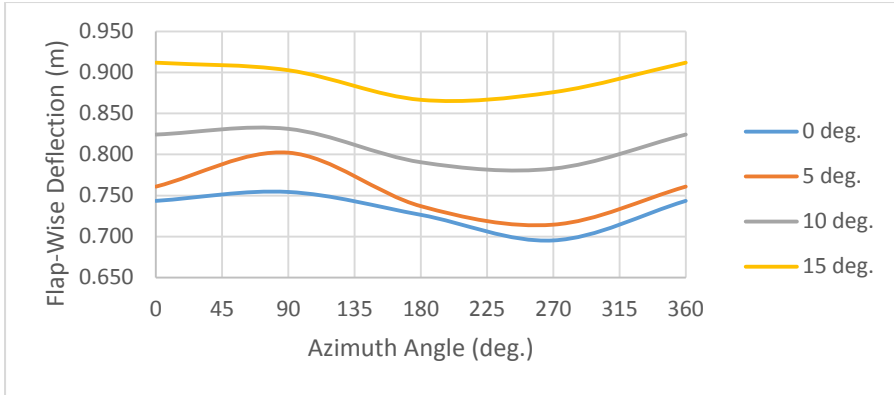


(b)

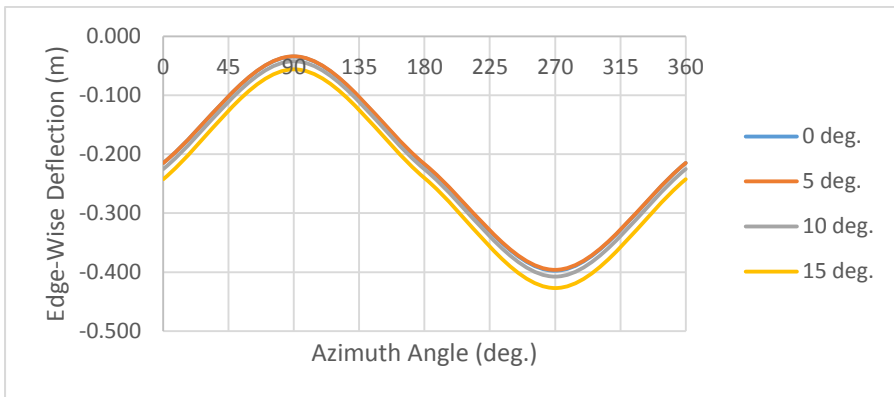


(c)

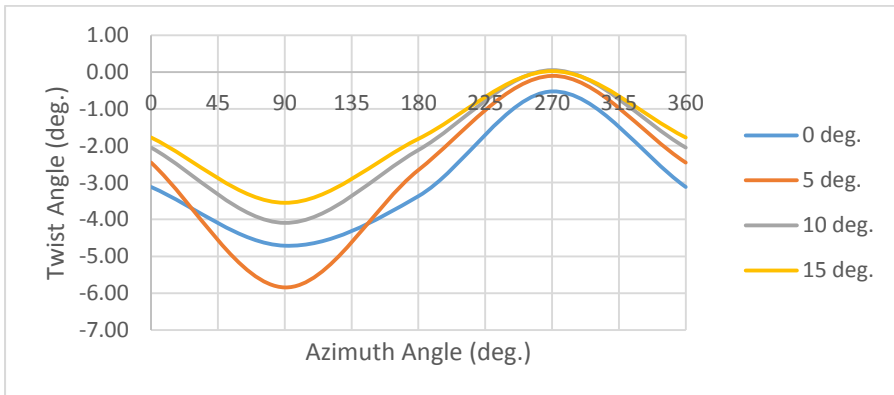
Figure 4-11 Blade deformation at 20m of the blade span for 0°, 5°, 10°, 15° carbon fiber orientation (a) Flap-wise deflection (b) Edge-wise deflection (c) Twist angle



(a)

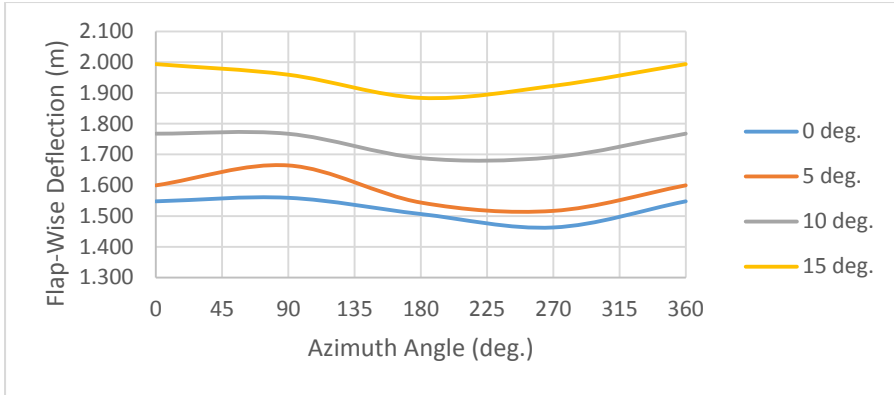


(b)

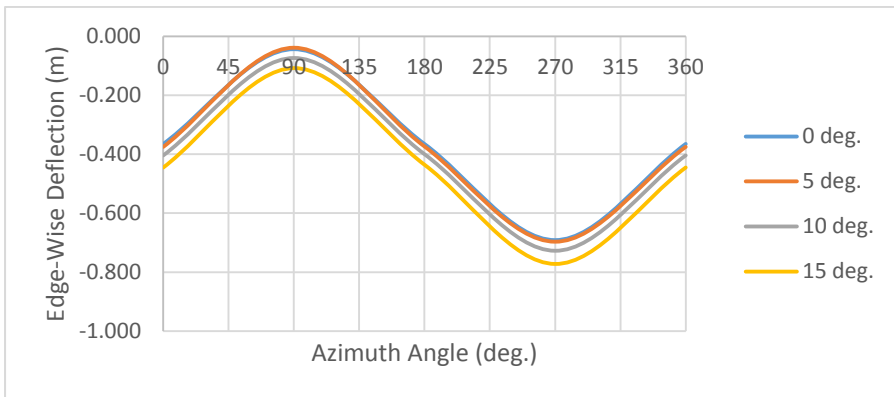


(c)

Figure 4-12 Blade deformation at 30m of the blade span for 0°, 5°, 10°, 15° carbon fiber orientation (a) Flap-wise deflection (b) Edge-wise deflection (c) Twist angle



(a)



(b)

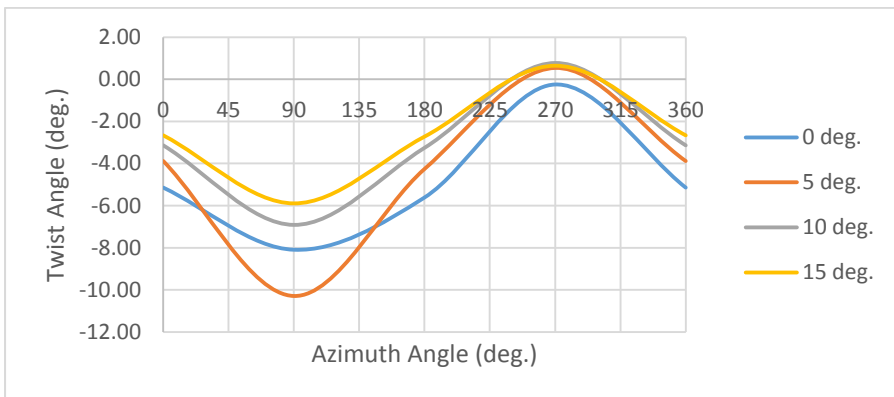
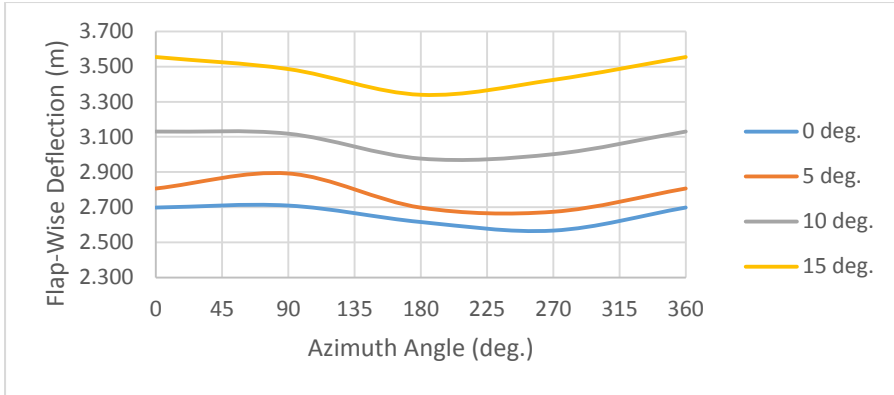
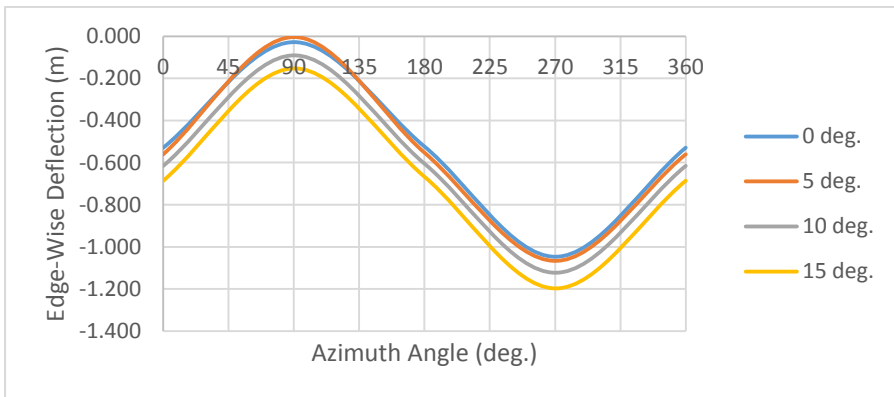


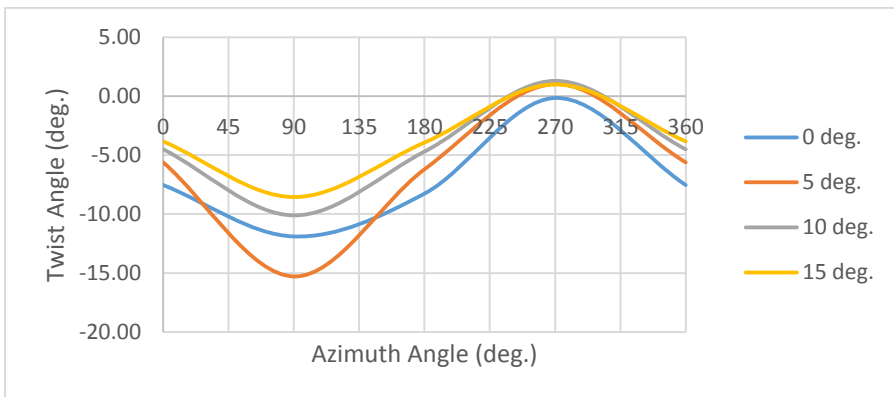
Figure 4-13 Blade deformation at 40m of the blade span for $0^{\circ}, 5^{\circ}, 10^{\circ}, 15^{\circ}$ carbon fiber orientation (a) Flap-wise deflection (b) Edge-wise deflection (c) Twist angle



(a)



(b)



(c)

Figure 4-14 Blade deformation at 50m of the blade span for $0^{\circ}, 5^{\circ}, 10^{\circ}, 15^{\circ}$ carbon fiber orientation (a) Flap-wise deflection (b) Edge-wise deflection (c) Twist angle

4.5.2 Optimization by increasing the fixation near the blade root

There is another approach to protect the blade from fatigue and stall. This approach depends on increasing the area of fixation at the blade root which could be achieved by adding extra webs perpendicular to the shear web. This method is presented in the FE model by extending the blade fixation from its edge to a part of the blade surface. There are two models created for this approach, one at 1.5 m from the blade root and the other is at 3m.



Figure 4-15 Blade fixation

The output power in all FSI cases is higher than the rigid one; however, these high values decrease by increasing the area of fixation as shown in Figure 4-16.

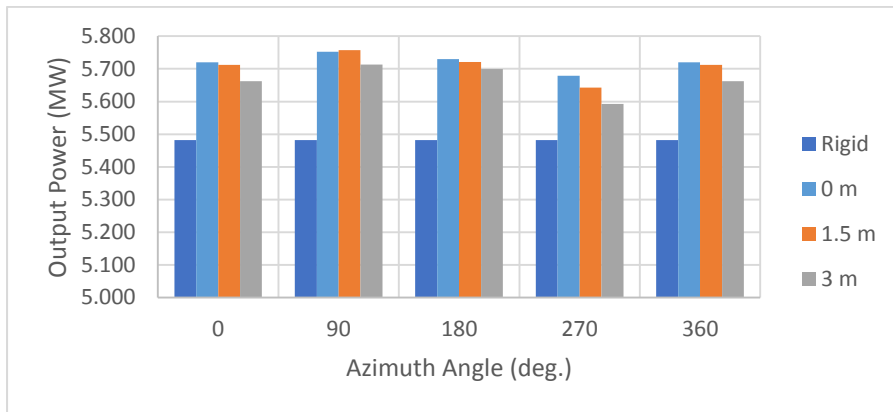
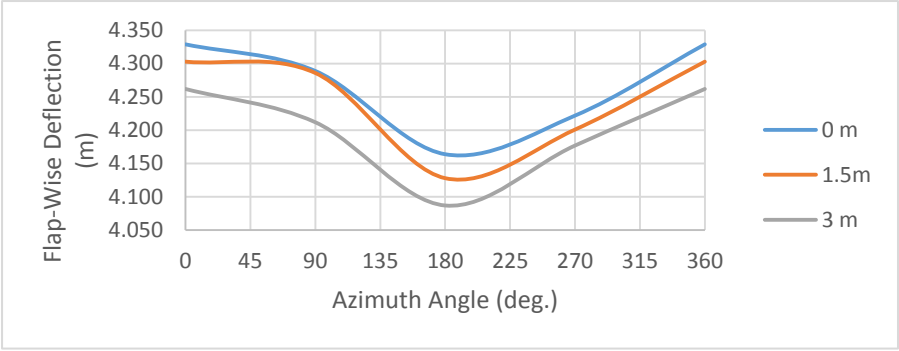


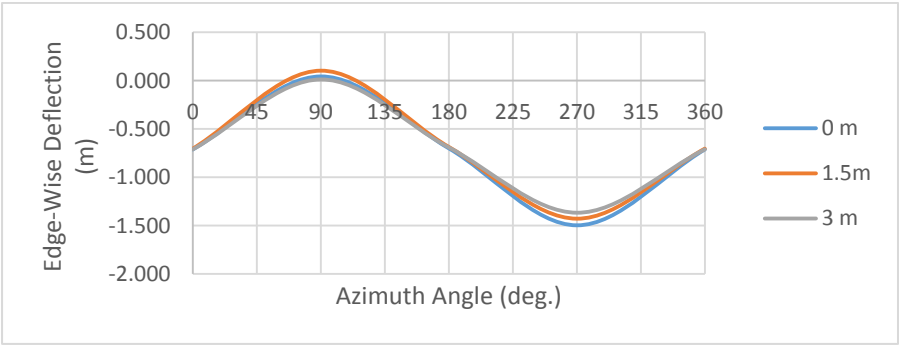
Figure 4-16 Comparison of the output power between the rigid and different fixation schemes

As shown in Figure 4-17, Figure 4-18, Figure 4-19, Figure 4-20, and Figure 4-21 the longitudinal stiffness of the blade is increased by increasing the area of fixation which leads to a decrease in the flap-wise deflection. However, the edgewise deflection and torsion are

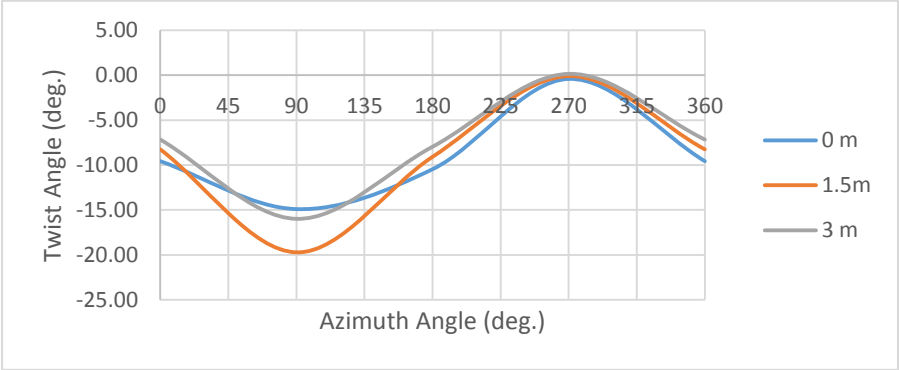
almost the same. The benefit of this method is that it could be used to increase the bending stiffness which leads to a decrease in the clearance between the blade and the tower. These figures illustrate the flap-wise deflection, edge-wise deflection, and torsion at five cross-sections of the blade starting from 20m from the blade root to the tip.



(a)

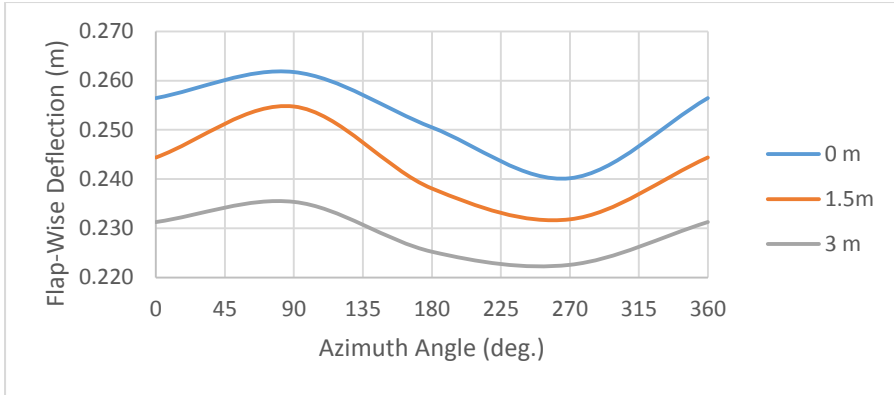


(b)

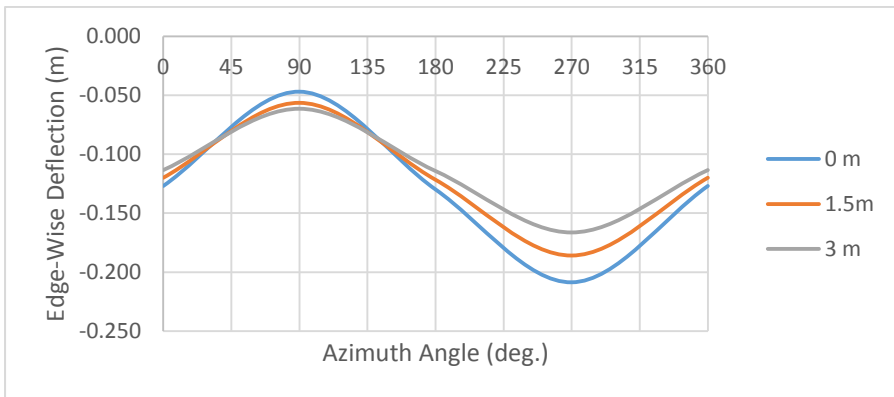


(c)

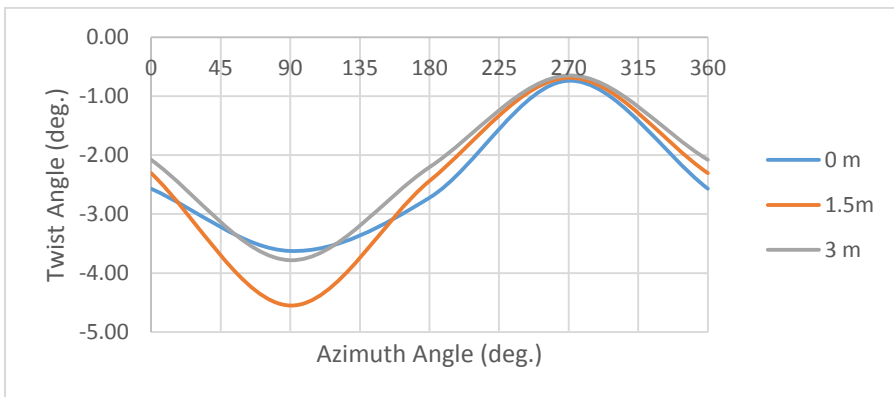
Figure 4-17 Blade deformation at the tip for 0m, 1.5m, 3m fixation (a) Flap-wise deflection (b) Edge-wise deflection (c) Twist angle



(a)

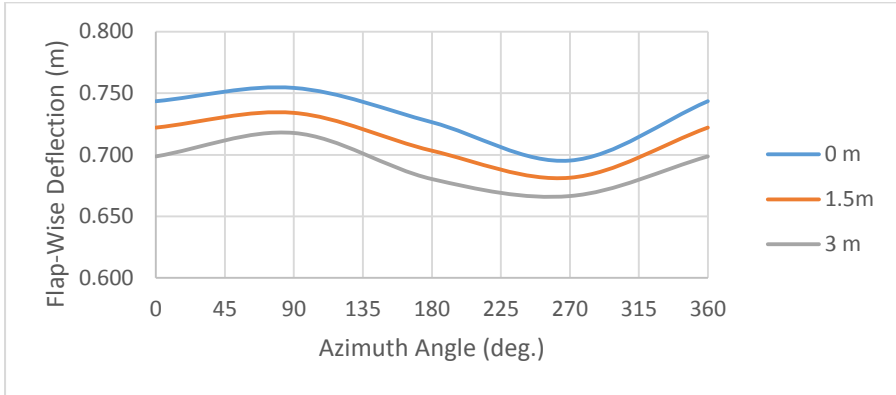


(b)

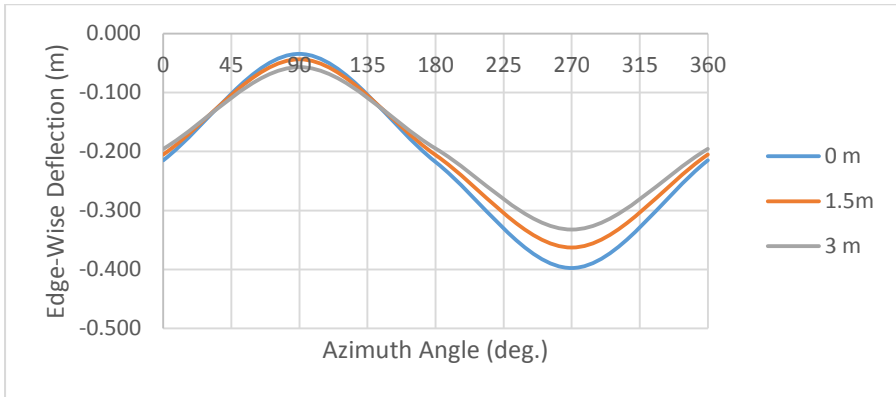


(c)

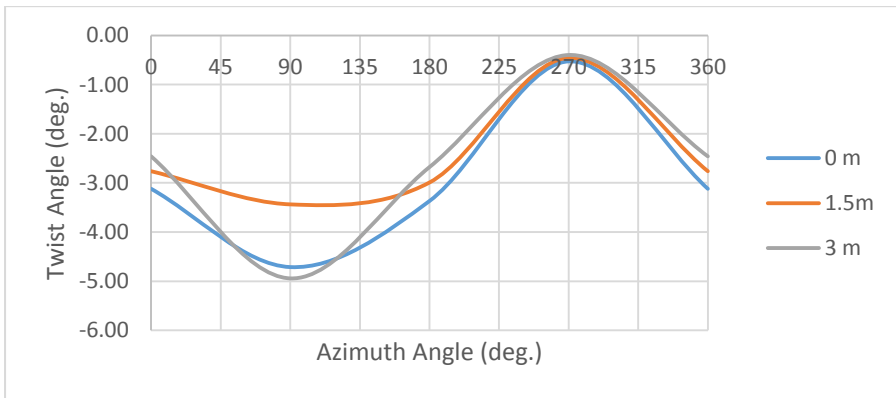
Figure 4-18 Blade deformation at 20m of the blade span for 0m, 1.5m, 3m fixation (a) Flap-wise deflection (b) Edge-wise deflection (c) Twist angle



(a)

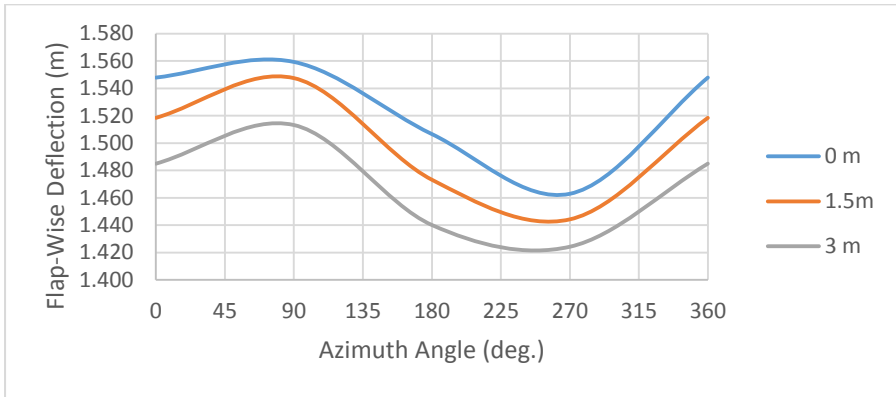


(b)

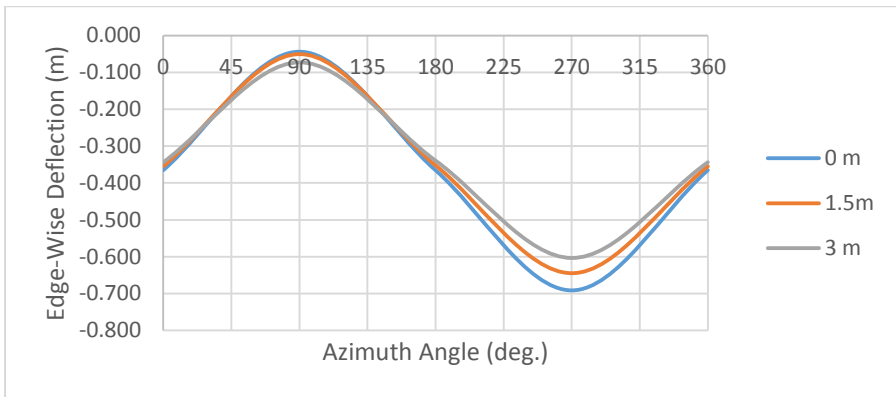


(c)

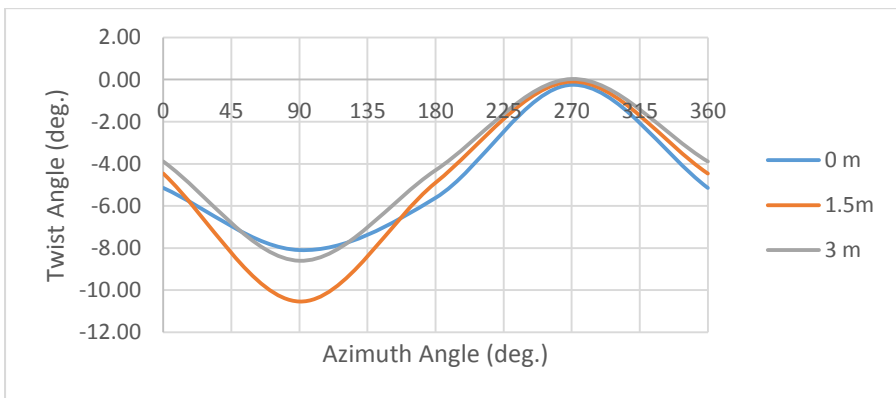
Figure 4-19 Blade deformation at 30m of the blade span for 0m, 1.5m, 3m fixation (a) Flap-wise deflection (b) Edge-wise deflection (c) Twist angle



(a)

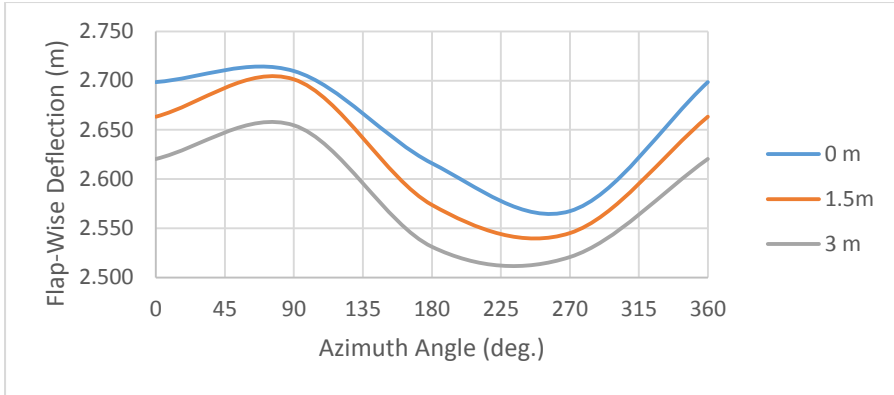


(b)

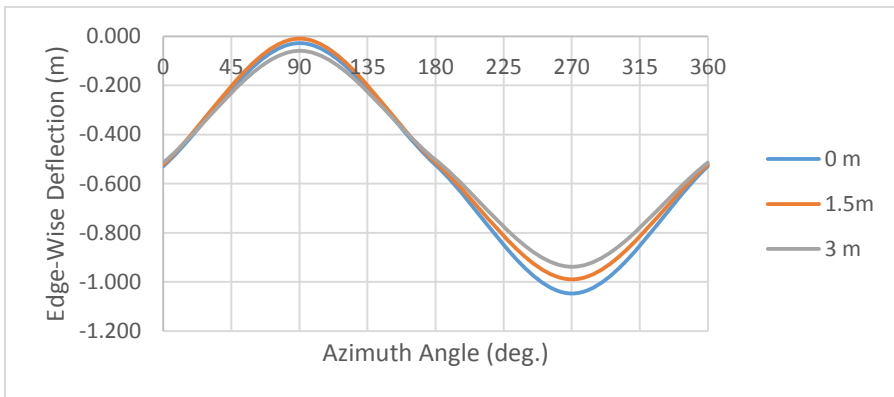


(c)

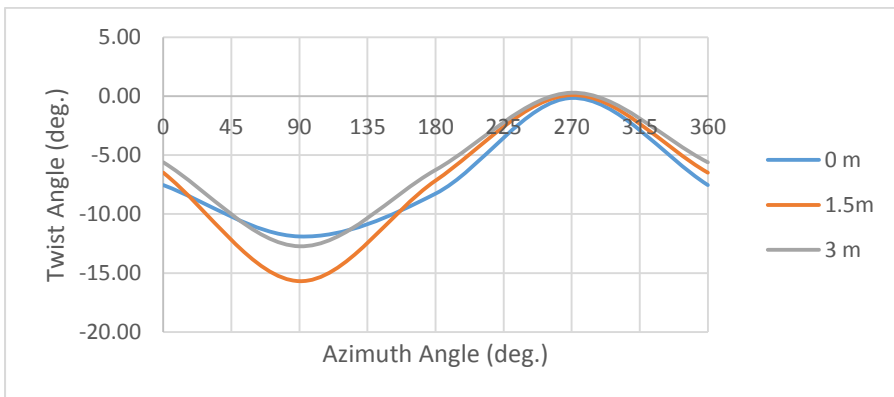
Figure 4-20 Blade deformation at 40m of the blade span for 0m, 1.5m, 3m fixation (a) Flap-wise deflection (b) Edge-wise deflection (c) Twist angle



(a)



(b)



(c)

Figure 4-21 Blade deformation at 50m of the blade span for 0m, 1.5m, 3m fixation (a) Flap-wise deflection (b) Edge-wise deflection (c) Twist angle

Chapter 5 Conclusion and recommendations

5.1 Conclusion

In the present work, the wind turbine blade is studied as an application of FSI. The reference blade of 5 MW is developed by the National Laboratory of Renewable Energy (NREL). The CFD model is created and validated by ANSYS Fluent while the FE model is generated by Abaqus. The data are exchanged between both models through MPCCI. The composite layup of the blade is modeled from Sandia report [101], Chen et al. [87], and Shakya et al. [92]. Uniaxial, biaxial, and triaxial layups of fiberglass, carbon fibers, and foam.

The CFD model is validated against the tip speed and the generated power indicated in the NREL 5 MW wind turbine report. The tip speed from the FCD model is 78.7 m/s while the reference value is 80m/s. The calculated power difference from the average of reference values is 0.6% and 1.27% for rigid and flexible cases respectively.

The flap-wise deflection from the FE model is 6.055m with a difference of 0.4%. and the six mode shape frequencies are within the limits of the reference values.

A 2-way coupling model is applied on the blade at the rated operating conditions and gives more accurate results than 1-way coupling as the deformation of the blade due to wind load is reflected on the CFD mesh. Then, the power is calculated again according to the new mesh.

The centrifugal and gravitational loads affect the blade deformation. The centrifugal force value is constant while its direction is radial and outward. The gravitational load effect depends on the blade position. The centrifugal force has an impact on reducing the flap-wise

deflection and increasing the blade twist angle. The gravitational force affects the flap-wise deflection in the vertical position and the edge-wise deflection in the horizontal position.

The blade deformation is optimized by applying the material BTC concept. This is achieved by rotating the carbon fibers away from the blade axis. Three cases are performed on the BTC blade at 5° , 10° , 15° away from the blade axis and the following conclusions can be drawn:

- 1- The material BTC method depends on the fiber orientation if the spar cap
- 2- The flap-wise stiffness is extremely affected by the fibers rotation angle, as the flap-wise deflection is increased by increasing the rotation angle.
- 3- The fibers' off-axis rotation angle is limited to the clearance between the rotor and the tower.
- 4- The rotation angle has a minor effect on the edge-wise deflection which could be neglected
- 5- The torsional stiffness is increased by increasing the rotation angle
- 6- The generated power in the rigid case is lower than the flexible one; however, the power is slightly reduced in the case of the BTC blade but still higher than the rigid blade.
- 7- The peak-to-peak amplitude of the blade twist angle is reduced by increasing the angle of rotation resulting in the protection of the blade from damage due to fatigue.
- 8- Due to the increase in the torsional stiffness, the twist angle is reduced at all positions of the blade. This reduction allows the blade to twist to feather and protect it from the stall.

The other optimization approach is increasing the blade stiffness by strengthening it from the root side which can be achieved by adding extra webs at the blade root. This approach is implemented by fixing part of the blade root surface resulting in the improvement in blade flap-wise deflection. However, the edge-wise deflection and twisting are still not improved. Regarding the generated power, it is decreased by increasing the fixation area but still higher than the rigid blade case.

5.2 Recommendations

The recommendations for future studies are summarized in the following points

- 1- Performing the FSI model in transient condition to extract the results at all positions of the blade.
- 2- Running a strong coupling FSI and compare the blade deformation with the present study
- 3- Creating a geometric BTC blade and compare it with the current material BTC
- 4- Creating a combination of a BTC blade and root fixation then studying its effect on blade optimization
- 5- Predicting the lifetime of the blade due to fatigue
- 6- Creating an economic study for the impact of changing the blade material on the total cost of the turbine and the improvement in its performance.

References

- [1] P. Moriarty and D. Honnery, “Can renewable energy power the future?,” *Energy Policy*, vol. 93, pp. 3–7, 2016, doi: 10.1016/j.enpol.2016.02.051.
- [2] “BP Statistical Review of World Energy,” 2020. [Online]. Available: <https://www.bp.com/en/global/corporate/energy-economics/statistical-review-of-world-energy/renewable-energy.html#wind-energy>.
- [3] J. Tu, K. Inthavong, and K. K. L. Wong, *Computational Fluid Structure Interaction Methods and Applications*. WILEY, 2013.
- [4] “Ansys® Academic Research Fluent, Release 18.0.” .
- [5] “Abaqus. Dassault Systemes. Release 18.0. [Online]. Available: <http://www.simulia.com>.” .
- [6] “MpCCI CouplingEnvironment.” Fraunhofer SCAI, [Online]. Available: www.mpcci.de.
- [7] R. Gasch and J. Twele, “Wind Power Plants: Fundamentals, Design, Construction and Operation,” p. 567, 2012, doi: 10.1007/978-3-642-22938-1.
- [8] T. Burton, N. Jenkins, D. Sharpe, and E. Bossanyi, *Wind Energy Handbook*, Second Edi. John Wiley & Sons, Ltd, 2011.
- [9] R. Gawarkiewicz, F. Wasilczuk, and M. Wasilczuk, “Drivetrain of a Wind Turbine,” *Mach. Dyn. Res.*, vol. 39, no. 2, pp. 83–95, 2015.
- [10] N. Goudarzi and W. D. Zhu, “A review on the development of wind turbine generators across the world,” *Int. J. Dyn. Control*, vol. 1, no. 2, pp. 192–202, 2013, doi: 10.1007/s40435-013-0016-y.
- [11] M. G. Kim and P. H. Dalhoff, “Yaw systems for wind turbines- Overview of concepts, current challenges and design methods,” *J. Phys. Conf. Ser.*, vol. 524, no. 1, 2014, doi: 10.1088/1742-6596/524/1/012086.
- [12] Y. Yasuda, S. Yokoyama, M. Minowa, and T. Satoh, “Classification of lightning damage to wind turbine blades,” *IEEJ Trans. Electr. Electron. Eng.*, vol. 7, no. 6, pp. 559–566, 2012, doi: 10.1002/tee.21773.

- [13] D. Ancona and J. McVeigh, “Wind turbine-materials and manufacturing fact sheet,” *Princet. Energy Resour. Int. LLC*, pp. 1–8, 2001, [Online]. Available: http://www.perihq.com/documents/WindTurbine-MaterialsandManufacturing_FactSheet.pdf.
- [14] P. Brøndsted and R. P. L. Nijssen, *Advances in wind turbine blade design and materials*. Woodhead Publishing, 2013.
- [15] P. J. Schubel and R. J. Crossley, “Wind turbine blade design,” *Energies*, vol. 5, no. 9, pp. 3425–3449, 2012.
- [16] M. Hansen, *Aerodynamics of Wind Turbines*, 2nd ed. London;Sterling, VA; Earthscan: Routledge, 2008.
- [17] E. Hau, *Wind turbines: fundamentals, technologies, application, economics*, 2nd ed. New York;Berlin: Springer, 2005.
- [18] L. Mishnaevsky, K. Branner, H. N. Petersen, J. Beauson, M. McGugan, and B. F. Sørensen, “Materials for wind turbine blades: An overview,” *Materials (Basel)*, vol. 10, no. 11, 2017, doi: 10.3390/ma10111285.
- [19] A. P. Vassilopoulos, *Fatigue life prediction of composites and composite structures*. 2010.
- [20] K. B. Katnam, A. J. Comer, D. Roy, L. F. M. Da Silva, and T. M. Young, “Composite repair in wind turbine blades: An overview,” *J. Adhes.*, vol. 91, no. 1–2, pp. 113–139, 2015, doi: 10.1080/00218464.2014.900449.
- [21] C. P. Debel, “Identification of damage types in wind turbine blades tested to failure,” in *Materialeopførsel og skadesanalyse*, 2004, pp. 123–127.
- [22] K. Skelton, “Discussion paper on managin composite blade waste,” *Windeurope.Org*, no. March, p. 18, 2017, doi: 10.13140/RG.2.2.22748.90248.
- [23] L. Mishnaevsky and P. Brøndsted, “Statistical modelling of compression and fatigue damage of unidirectional fiber reinforced composites,” *Compos. Sci. Technol.*, vol. 69, no. 3–4, pp. 477–484, 2009, doi: 10.1016/j.compscitech.2008.11.024.
- [24] S. Joncas, *Thermoplastic Composite Wind Turbine Blades*. 2010.
- [25] “Ansys® Academic Research System Coupling.” [Online].

Available: www.ansys.com/academic.

- [26] “COMSOL Multiphysics.” COMSOL Inc., [Online]. Available: www.comsol.com.
- [27] X. Cai, P. Pan, J. Zhu, and R. Gu, “The analysis of the aerodynamic character and structural response of large-scale wind turbine blades,” *Energies*, vol. 6, no. 7, pp. 3134–3148, 2013, doi: 10.3390/en6073134.
- [28] M. S. Jeong, S. W. Kim, I. Lee, S. J. Yoo, and K. C. Park, “Investigation of Wake effects on aeroelastic responses of horizontal-axis wind-turbines,” *AIAA J.*, vol. 52, no. 6, pp. 1133–1144, 2014, doi: 10.2514/1.J051899.
- [29] J. Jonkman, S. Butterfield, W. Musial, and G. Scott, “Definition of a 5-MW reference wind turbine for offshore system development,” 2009. [Online]. Available: http://tethys-development.pnnl.gov/sites/default/files/publications/Jonkman_et_al_2009.pdf.
- [30] L. J. F. M.M. Hand, D.A. Simms, A. D.W. Jager, J.R. Cotrell, S. Schreck, and S. M. Larwood, “Unsteady Aerodynamics Experiment Phase VI: Wind Tunnel Test Configurations and Available Data Campaigns,” no. 7, pp. 27–28, 2017.
- [31] M. Carrión, M. Woodgate, R. Steijl, G. Barakos, S. Gómez-Iradi, and X. Munduate, “CFD and aeroelastic analysis of the MEXICO wind turbine,” *J. Phys. Conf. Ser.*, vol. 555, no. 1, 2014, doi: 10.1088/1742-6596/555/1/012006.
- [32] A. Bechmann, N. Sørensen, and F. Zahle, “CFD simulations of the MEXICO rotor,” *Wind Energy*, vol. 14, pp. 677–689, 2011, doi: 10.1002/we.450.
- [33] D. W. MacPhee and A. Beyene, “Experimental and Fluid Structure Interaction analysis of a morphing wind turbine rotor,” *Energy*, vol. 90, pp. 1055–1065, 2015, doi: 10.1016/j.energy.2015.08.016.
- [34] M. E. Braaten, C. Seeley, and M. Tooley, “High fidelity fluid-structure interaction analysis of a wind turbine blade,” 2013, doi: 10.2514/6.2013-1693.
- [35] W. Mo, D. Li, X. Wang, and C. Zhong, “Aeroelastic coupling analysis of the flexible blade of a wind turbine,” *Energy*, vol. 89, pp. 1001–1009, 2015, doi: 10.1016/j.energy.2015.06.046.

- [36] X. Liu, X. Zhang, D. Li, Y. Chen, and Z. Ye, “Unsteady aerodynamic force analysis of wind turbine airfoil,” *Yingyong Jichu yu Gongcheng Kexue Xuebao/Journal Basic Sci. Eng.*, vol. 18, pp. 503–516, 2010, doi: 10.3969/j.issn.1005-0930.2010.03.015.
- [37] L. Wang, R. Quant, and A. Kolios, “Fluid structure interaction modelling of horizontal-axis wind turbine blades based on CFD and FEA,” *J. Wind Eng. Ind. Aerodyn.*, vol. 158, pp. 11–25, 2016, doi: 10.1016/j.jweia.2016.09.006.
- [38] M. L. Jonkman, J.M., Buhl Jr, “FAST User’s Guide. National Renewable Energy Laboratory, Golden, CO.,” 2005.
- [39] E. Hoogedoorn, G. B. Jacobs, and A. Beyene, “Aero-elastic behavior of a flexible blade for wind turbine application: A 2D computational study,” *Energy*, vol. 35, no. 2, pp. 778–785, 2010, doi: 10.1016/j.energy.2009.08.030.
- [40] M. Drela, “XFOIL: an analysis and design system for low Reynolds number airfoils.,” *Low Reynolds Number Aerodyn. Proc. Conf., Notre Dame, U.S.a., June 5-7, 1989 }Edited By T.J. Mueller}. (Lecture Notes, no. 54)*, Berlin, Germany, Springer-Verlag, 1989, pp. 1–12, 1989, doi: 10.1007/978-3-642-84010-4_1.
- [41] *Partial Differential Equation Toolbox™ User’s Guide, the mathworks MATLAB*. 2007.
- [42] G. Santo, M. Peeters, W. van Paeppegem, and J. Degroote, “Fluid–structure interaction simulations of a wind gust impacting on the blades of a large horizontal axis wind turbine,” *Energies*, vol. 13, no. 3, 2020, doi: 10.3390/en13030509.
- [43] S. Timme, K. J. Badcock, and A. Da Ronch, “Gust analysis using computational fluid dynamics derived reduced order models,” *J. Fluids Struct.*, vol. 71, pp. 116–125, 2017, doi: 10.1016/j.jfluidstructs.2017.03.004.
- [44] Z. Wang and C. Zhu, “Numerical simulation for in-cloud icing of three-dimensional wind turbine blades,” *Simulation*, vol. 94, no. 1, pp. 31–41, 2018, doi: 10.1177/0037549717712039.
- [45] C. Grinderslev, F. Belloni, S. G. Horcas, and N. Sørensen, “Investigations of aerodynamic drag forces during structural blade testing using high fidelity fluid-structure interaction,” *Investig. Aerodyn. drag forces Dur. Struct. Bl. Test. using high*

- Fidel. fluid-structure Interact.*, pp. 1–26, 2019, doi: 10.5194/wes-2019-64.
- [46] P. R. Greaves, R. G. Dominy, G. L. Ingram, H. Long, and R. Court, “Evaluation of dual-axis fatigue testing of large wind turbine blades,” *Proc. Inst. Mech. Eng. Part C J. Mech. Eng. Sci.*, vol. 226, no. 7, pp. 1693–1704, 2012, doi: 10.1177/0954406211428013.
- [47] F. Shi, Z. Wang, J. Zhang, Z. Gong, and L. Guo, “Influences of wind and rotating speed on the fluid-structure interaction vibration for the offshore wind turbine blade,” *J. Vibroengineering*, vol. 21, no. 2, pp. 483–497, 2019, doi: 10.21595/jve.2018.19356.
- [48] D. A. Corson, D. T. Griffith, T. Ashwill, and F. Shakib, “Investigating aeroelastic performance of multi-megawatt wind turbine rotors using CFD,” *Collect. Tech. Pap. - AIAA/ASME/ASCE/AHS/ASC Struct. Struct. Dyn. Mater. Conf.*, no. April, pp. 1–17, 2012, doi: 10.2514/6.2012-1827.
- [49] Z. Yu, Z. Hu, X. Zheng, Q. Ma, and H. Hao, “Aeroelastic performance analysis of wind turbine in the wake with a new elastic actuator line model,” *Water (Switzerland)*, vol. 12, no. 5, 2020, doi: 10.3390/W12051233.
- [50] Joel H. Ferziger and M. Peric, *Computational Methods for Fluid Dynamics*. Berlin, Germany: Springer Science & Business, 2012.
- [51] Y. Li, A. M. Castro, T. Sinokrot, W. Prescott, and P. M. Carrica, “Coupled multi-body dynamics and CFD for wind turbine simulation including explicit wind turbulence,” *Renew. Energy*, vol. 76, pp. 338–361, 2015, doi: 10.1016/j.renene.2014.11.014.
- [52] M. S. Jeong, M. C. Cha, S. W. Kim, and I. Lee, “Numerical investigation of optimal yaw misalignment and collective pitch angle for load imbalance reduction of rigid and flexible HAWT blades under sheared inflow,” *Energy*, vol. 84, pp. 518–532, 2015, doi: 10.1016/j.energy.2015.03.016.
- [53] F. L. Ponta, A. D. Otero, L. I. Lago, and A. Rajan, “Effects of rotor deformation in wind-turbine performance: The Dynamic Rotor Deformation Blade Element Momentum model (DRD-BEM),” *Renew. Energy*, vol. 92, pp. 157–170, 2016, doi: 10.1016/j.renene.2016.01.098.

- [54] D. O. Yu and O. J. Kwon, “A coupled CFD-CSD method for predicting HAWT rotor blade performance,” *51st AIAA Aerosp. Sci. Meet. Incl. New Horizons Forum Aerosp. Expo. 2013*, no. January, pp. 1–22, 2013, doi: 10.2514/6.2013-911.
- [55] Z. Ma, P. Zeng, and L. P. Lei, “Analysis of the coupled aeroelastic wake behavior of wind turbine,” *J. Fluids Struct.*, vol. 84, pp. 466–484, 2019, doi: 10.1016/j.jfluidstructs.2018.09.001.
- [56] B. Dose, H. Rahimi, I. Herráez, B. Stoevesandt, and J. Peinke, “Fluid-structure coupled computations of the NREL 5 MW wind turbine by means of CFD,” *Renew. Energy*, vol. 129, pp. 591–605, 2018, doi: 10.1016/j.renene.2018.05.064.
- [57] “The OpenFOAM Foundation Ltd, OpenFOAM: the Open Source Computational Fluid Dynamics (CFD) Toolbox v4.1.0, 2016.,” [Online]. Available: <https://openfoam.org/>.
- [58] D. Foti, X. Yang, L. Shen, and F. Sotiropoulos, “Effect of wind turbine nacelle on turbine wake dynamics in large wind farms,” *J. Fluid Mech.*, vol. 869, pp. 1–26, 2019, doi: 10.1017/jfm.2019.206.
- [59] D. O. Yu and O. J. Kwon, “Time-accurate aeroelastic simulations of a wind turbine in yaw and shear using a coupled CFD-CSD method,” *J. Phys. Conf. Ser.*, vol. 524, no. 1, 2014, doi: 10.1088/1742-6596/524/1/012046.
- [60] C. Heinz, N. Sørensen, F. Zahle, and W. Skrzypinski, “Vortex-induced vibrations on a modern wind turbine blade,” *Wind Energy*, pp. 1–11, 2016, doi: 10.1002/we.1967.
- [61] M. C. Hsu and Y. Bazilevs, “Fluid-structure interaction modeling of wind turbines: Simulating the full machine,” *Comput. Mech.*, vol. 50, no. 6, pp. 821–833, 2012, doi: 10.1007/s00466-012-0772-0.
- [62] M. Imiela, F. Wienke, C. Rautmann, C. Willberg, P. Hilmer, and A. Krumme, “Towards multidisciplinary wind turbine design using high-fidelity methods,” *AIAA*, pp. 1–12, 2015, doi: 10.2514/6.2015-1462.
- [63] T. G. and R. H. D. Schwamborn, “‘The DLR TAU - Code: Recent Applications in Research and Industry’ , In proceedings of ‘European Conference on Computational Fluid Dynamics‘ ECCOMAS CDF 2006, Delft The Netherland, 2006.,” p. 2006,

2006.

- [64] T. F. and C. W. S. Freund, F. Heinecke, ““Parametric Model Generation and Sizing of Lightweight Structures for a Multidisciplinary Design Process” , NAFEMS, 20-21 May in Bamberg Germany.,” p. 21.
- [65] H. A. Madsen, J. Johansen, N. N. Sørensen, G. C. Larsen, and M. H. Hansen, “Simulation of low frequency noise from a downwind wind turbine rotor,” *Collect. Tech. Pap. - 45th AIAA Aerosp. Sci. Meet.*, vol. 11, no. July 2015, pp. 7549–7560, 2007, doi: 10.2514/6.2007-623.
- [66] F. Zahle, N. N. Sørensen, and J. Johansen, “Wind turbine rotor-tower interaction using an incompressible overset grid method,” *Wind Energy*, vol. 12, no. 6, pp. 594–619, 2009, doi: 10.1002/we.327.
- [67] Y. Bazilevs, M. Hsu, J. Kiendl, R. Wüchner, and K. Bletzinger, “3D Simulation of Wind Turbine Rotors at Full Scale. Part I: Geometry modeling and aerodynamics,” *Int. J. Numer. Methods Fluids*, vol. 65, pp. 207–235, 2011, doi: 10.1002/fld.
- [68] Y. Bazilevs, M. Hsu, J. Kiendl, R. Wüchner, and K. Bletzinger, “3D Simulation of Wind Turbine Rotors at Full Scale. Part II: Fluid – Structure Interaction Modeling with Composite Blades,” *Int. J. Numer. Methods Fluids*, vol. 65, pp. 236–253, 2011, doi: 10.1002/fld.
- [69] J. Kiendl, Y. Bazilevs, M. C. Hsu, R. Wüchner, and K. U. Bletzinger, “The bending strip method for isogeometric analysis of Kirchhoff-Love shell structures comprised of multiple patches,” *Comput. Methods Appl. Mech. Eng.*, vol. 199, no. 37–40, pp. 2403–2416, 2010, doi: 10.1016/j.cma.2010.03.029.
- [70] G. Santo, M. Peeters, W. Van Paepegem, and J. Degroote, “The effect of gravity in transient fluid-structure interaction simulations of a large wind turbine with composite blades,” *8th Int. Conf. Text. Compos. Inflatable Struct. - Struct. Membr. 2017*, p. 12, 2017.
- [71] J. Degroote, “Partitioned Simulation of Fluid-Structure Interaction: Coupling Black-Box Solvers with Quasi-Newton Techniques,” *Arch. Comput. Methods Eng.*, vol. 20, no. 3, pp. 185–238, 2013, doi: 10.1007/s11831-013-9085-5.
- [72] G. Santo, M. Peeters, W. Van Paepegem, and J. Degroote,

- “Dynamic load and stress analysis of a large horizontal axis wind turbine using full scale fluid-structure interaction simulation,” *Renew. Energy*, vol. 140, pp. 212–226, 2019, doi: 10.1016/j.renene.2019.03.053.
- [73] P. Krawczyk, A. Beyene, and D. MacPhee, “Fluid structure interaction of a morphed wind turbine blade,” *Int. J. Energy Res.*, vol. 37, no. 14, pp. 1784–1793, 2013, doi: 10.1002/er.2991.
- [74] Y. J. Lee, Y. T. Jhan, and C. H. Chung, “Fluid-structure interaction of FRP wind turbine blades under aerodynamic effect,” *Compos. Part B Eng.*, vol. 43, no. 5, pp. 2180–2191, 2012, doi: 10.1016/j.compositesb.2012.02.026.
- [75] A. Chehouri, R. Younes, A. Ilinca, and J. Perron, “Review of performance optimization techniques applied to wind turbines,” *Appl. Energy*, vol. 142, pp. 361–388, 2015, doi: 10.1016/j.apenergy.2014.12.043.
- [76] H. Snel, “Review of aerodynamics for wind turbines,” *Wind Energy*, vol. 6, no. 3, pp. 203–211, 2003, doi: 10.1002/we.97.
- [77] K. Oğuz and N. Sezer-Uzol, “Aerodynamic Optimization of Horizontal Axis Wind Turbine Rotor by Using BEM, CST Method and Genetic Algorithm,” 2019.
- [78] B. Bavanish and K. Thyagarajan, “Optimization of power coefficient on a horizontal axis wind turbine using bem theory,” *Renew. Sustain. Energy Rev.*, vol. 26, pp. 169–182, 2013, doi: 10.1016/j.rser.2013.05.009.
- [79] C. C. Liao, X. L. Zhao, and J. Z. Xu, “Blade layers optimization of wind turbines using FAST and improved PSO Algorithm,” *Renew. Energy*, vol. 42, pp. 227–233, 2012, doi: 10.1016/j.renene.2011.08.011.
- [80] J. Chen, Q. Wang, W. Z. Shen, X. Pang, S. Li, and X. Guo, “Structural optimization study of composite wind turbine blade,” *Mater. Des.*, vol. 46, pp. 247–255, 2013, doi: 10.1016/j.matdes.2012.10.036.
- [81] A. R. Stäblein, “Analysis and Design of Bend-Twist Coupled Wind Turbine Blades,” in *MARE-WINT: New Materials and Reliability in Offshore Wind Turbine Technology*, W. Ostachowicz, M. McGugan, J.-U. Schröder-Hinrichs, and M. Luczak, Eds. Cham: Springer International Publishing, 2016,

pp. 67–80.

- [82] T. D. Ashwill, G. Kanaby, K. Jackson, and M. Zuteck, “Development of the swept-twist adaptive rotor (star) blade,” *48th AIAA Aerosp. Sci. Meet. Incl. New Horizons Forum Aerosp. Expo.*, pp. 4–7, 2010.
- [83] S. M. Barr, “Optimization of tow-steered composite wind turbine blades for static aeroelastic performance,” Lehigh University, 2018.
- [84] S. M. Barr and J. W. Jaworski, “Optimization of tow-steered composite wind turbine blades for static aeroelastic performance,” *Renew. Energy*, vol. 139, pp. 859–872, 2019, doi: 10.1016/j.renene.2019.02.125.
- [85] H. Meng, F. S. Lien, G. Glinka, and P. Geiger, “Study on fatigue life of bend-twist coupling wind turbine blade based on anisotropic beam model and stress-based fatigue analysis method,” *Compos. Struct.*, vol. 208, no. May 2018, pp. 678–701, 2019, doi: 10.1016/j.compstruct.2018.10.032.
- [86] K. Hayat and S. K. Ha, “Load mitigation of wind turbine blade by aeroelastic tailoring via unbalanced laminates composites,” *Compos. Struct.*, vol. 128, pp. 122–133, 2015, doi: 10.1016/j.compstruct.2015.03.042.
- [87] J. Chen, X. Shen, X. Zhu, and Z. Du, “Study on composite bend-twist coupled wind turbine blade for passive load mitigation,” *Compos. Struct.*, vol. 213, no. November 2018, pp. 173–189, 2019, doi: 10.1016/j.compstruct.2019.01.086.
- [88] D. I. Manolas, G. P. Serafeim, P. K. Chaviaropoulos, V. A. Riziotis, and S. G. Voutsinas, “Assessment of load reduction capabilities using passive and active control methods on a 10MW-scale wind turbine,” *J. Phys. Conf. Ser.*, vol. 1037, no. 3, 2018, doi: 10.1088/1742-6596/1037/3/032042.
- [89] D. W. Lobitz, “Aeroelastic stability predictions for a MW-sized blade,” *Wind Energy*, vol. 7, no. 3, pp. 211–224, 2004, doi: 10.1002/we.120.
- [90] G. Bir and J. Jonkman, “Aeroelastic instabilities of large offshore and onshore wind turbines,” *J. Phys. Conf. Ser.*, vol. 75, no. 1, 2007, doi: 10.1088/1742-6596/75/1/012069.
- [91] K. Hayat, A. G. M. De Lecea, C. D. Moriones, and S. K. Ha, “Flutter performance of bend-twist coupled large-scale wind

- turbine blades,” *J. Sound Vib.*, vol. 370, pp. 149–162, 2016, doi: 10.1016/j.jsv.2016.01.032.
- [92] P. Shakya, M. R. Sunny, and D. K. Maiti, “A parametric study of flutter behavior of a composite wind turbine blade with bend-twist coupling,” *Compos. Struct.*, vol. 207, no. June 2018, pp. 764–775, 2019, doi: 10.1016/j.compstruct.2018.09.064.
- [93] M. Hansen, “Stability analysis of three-bladed turbines using an eigenvalue approach,” *42nd AIAA Aerosp. Sci. Meet. Exhib. Proc. ASME Wind Energy Symp. Reno, Nevada*, no. January, 2004.
- [94] F. Meng, “Aero-elastic Stability Analysis for Large-Scale Wind Turbines,” TUDelft, 2011.
- [95] P. Pourazarm, Y. Modarres-Sadeghi, and M. Lackner, “A parametric study of coupled-mode flutter for MW-size wind turbine blades,” *Wind Energy*, no. May 2015, pp. 1–20, 2013, doi: 10.1002/we.
- [96] X. Zhou, K. Huang, and Z. Li, “Effects of bend-twist coupling on flutter limits of composite wind turbine blades,” *Compos. Struct.*, vol. 192, no. February, pp. 317–326, 2018, doi: 10.1016/j.compstruct.2018.02.071.
- [97] A. R. Ståblein, C. Tibaldi, and M. H. Hansen, “Using pretwist to reduce power loss of bend-twist coupled blades,” *34th Wind Energy Symp.*, 2016, doi: 10.2514/6.2016-1010.
- [98] A. R. Ståblein and M. H. Hansen, “Effect of Turbulence on Power for Bend-Twist Coupled Blades,” *J. Phys. Conf. Ser.*, vol. 753, no. 4, 2016, doi: 10.1088/1742-6596/753/4/042018.
- [99] M. H. H. Christian Bak, Frederik Zahle, Robert Bitsche, Taeseong Kim, Anders Yde, Lars Christian Henriksen, Anand Natarajan, “Description of the DTU 10 MW Reference Wind Turbine,” no. July, p. 138, 2013.
- [100] *IEC 61400-1 Ed. 3, wind turbines - Part 1: Design requirements, 2005.* .
- [101] B. R. Resor, “Definition of a 5MW/61.5 m wind turbine blade reference model,” *Albuquerque, New Mex. USA, Sandia Natl. Lab. SAND2013-2569 2013*, no. Sandia Report, p. 50, 2013.
- [102] “Ansys® Academic Research SpaceClaim, Release 18.0.” .
- [103] *Ansys Fluent Theory Guide*, no. November. 2013.

- [104] O. C. Zienkiewicz and R. Taylor, *The Finite Element Method*. 2000.
- [105] *MpCCI 4.5.2-1 Documentation*. 2018.

Appendix A

CFD mesh setup

1- Global mesh sizing

Sizing	
Size Function	Proximity and Curvature
Relevance Center	Fine
Initial Size Seed	Active Assembly
Transition	Slow
Span Angle Center	Fine
<input type="checkbox"/> Curvature Normal A...	Default (18.0 °)
<input type="checkbox"/> Num Cells Across G...	Default (3)
Proximity Size Functio...	Faces and Edges
<input type="checkbox"/> Min Size	Default (0.25920 m)
<input type="checkbox"/> Proximity Min Size	Default (0.25920 m)
<input type="checkbox"/> Max Face Size	Default (25.920 m)
<input type="checkbox"/> Max Tet Size	Default (51.840 m)
<input type="checkbox"/> Growth Rate	Default (1.20)
Automatic Mesh Base...	On
<input type="checkbox"/> Defeature Size	Default (0.12960 m)
Minimum Edge Length	6.5282e-003 m

2- Quality

Quality	
Check Mesh Quality	Yes, Errors
<input type="checkbox"/> Target Skewness	Default (0.900000)
Smoothing	Medium
Mesh Metric	Skewness
<input type="checkbox"/> Min	2.3341e-006
<input type="checkbox"/> Max	0.95257
<input type="checkbox"/> Average	0.22097
<input type="checkbox"/> Standard Deviation	0.13649

3- Statistics

Statistics	
<input type="checkbox"/> Nodes	1221818
<input type="checkbox"/> Elements	3573777

4- Local mesh sizing

[-] Scope	
Scoping Method	Geometry Selection
Geometry	7 Edges
[-] Definition	
Suppressed	No
Type	Number of Divisions
<input type="checkbox"/> Number of Divisions	900
[-] Advanced	
Size Function	Uniform
Behavior	Hard
Bias Type	No Bias

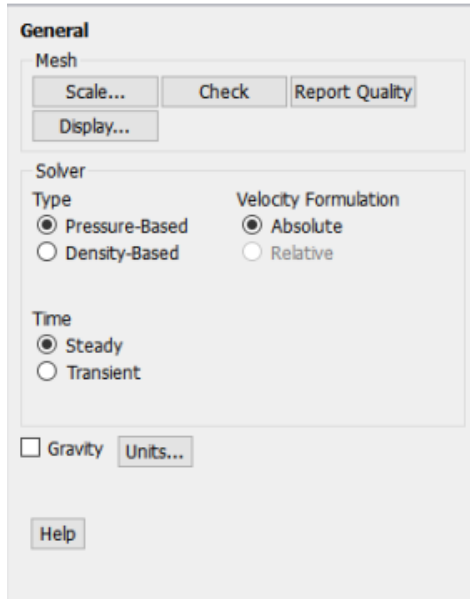
5- Inflation

[-] Scope	
Scoping Method	Geometry Selection
Geometry	1 Body
[-] Definition	
Suppressed	No
Boundary Scoping Method	Geometry Selection
Boundary	9 Faces
Inflation Option	First Layer Thickness
<input type="checkbox"/> First Layer Height	2.e-005 m
<input type="checkbox"/> Maximum Layers	20
<input type="checkbox"/> Growth Rate	1.2
Inflation Algorithm	Pre

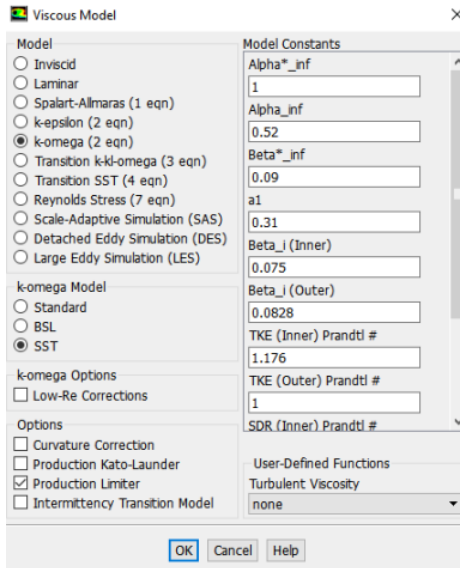
Appendix B

CFD model setup

6- General



7- Models



8- Materials

Create/Edit Materials

Name: Material Type:

Chemical Formula: Fluent Fluid Materials:

Mixture:

Order Materials by:
 Name
 Chemical Formula

Fluent Database...
User-Defined Database...

Properties

Density (kg/m3): Edit...

Viscosity (kg/m-s): Edit...

Change/Create Delete Close Help

9- Cell zone condition

Fluid

Zone Name:

Material Name: Edit...

Frame Motion 3D Fan Zone Source Terms
 Mesh Motion Laminar Zone Fixed Values
 Porous Zone

Reference Frame Mesh Motion Porous Zone 3D Fan Zone Embedded LES Reaction Source Terms Fixed Values Multiphase

Relative Specification UDF
Relative To Cell Zone: Zone Motion Function:

Rotation-Axis Origin Rotation-Axis Direction

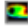
X (m): X:
Y (m): Y:
Z (m): Z:

Rotational Velocity Translational Velocity

Speed (rpm): X (m/s):
Copy To Mesh Motion Y (m/s):
Z (m/s):

OK Cancel Help

10- Boundary conditions

 Velocity Inlet ✕

Zone Name
inlet

Momentum Thermal Radiation Species DPM Multiphase Potential UDS

Velocity Specification Method Components

Reference Frame Absolute

Supersonic/Initial Gauge Pressure (pascal) 0 constant

Coordinate System Cartesian (X, Y, Z)

X-Velocity (m/s) 0 constant

Y-Velocity (m/s) 11.4 constant

Z-Velocity (m/s) 0 constant


Turbulence

Specification Method Intensity and Viscosity Ratio

Turbulent Intensity (%) 5 P

Turbulent Viscosity Ratio 10 P

OK Cancel Help

 Pressure Outlet ✕

Zone Name
outlet

Momentum Thermal Radiation Species DPM Multiphase Potential UDS

Backflow Reference Frame Absolute

Gauge Pressure (pascal) 0 constant

Backflow Direction Specification Method Normal to Boundary

Backflow Pressure Specification Total Pressure

Radial Equilibrium Pressure Distribution

Average Pressure Specification

Target Mass Flow Rate

Turbulence

Specification Method Intensity and Viscosity Ratio

Backflow Turbulent Intensity (%) 5 P

Backflow Turbulent Viscosity Ratio 10 P

OK Cancel Help

11- Mesh interfaces

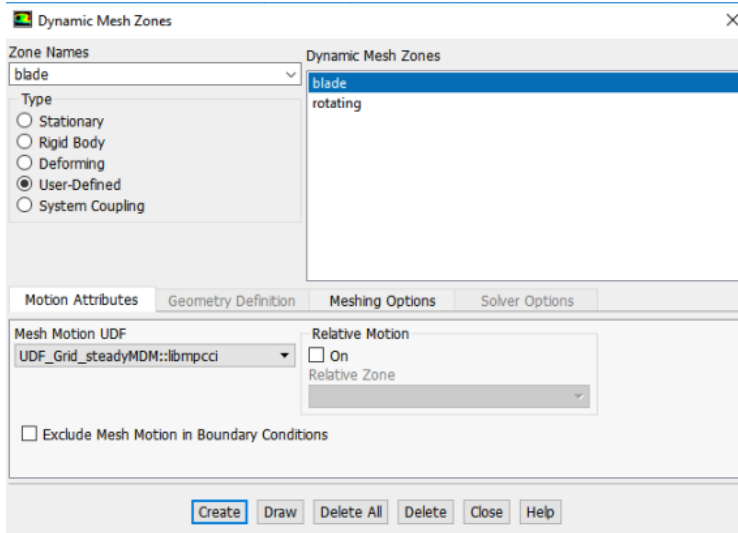
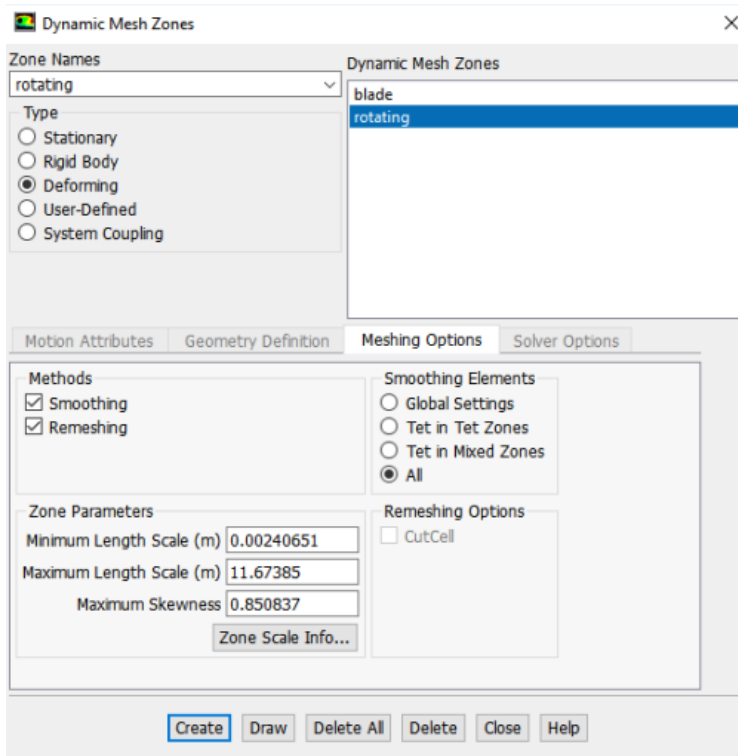
Create/Edit Mesh Interfaces

Mesh Interface	Interface Zones Side 1	Interface Zones Side 2
periodic-1	r1_inner_interface	r2_inner_interface
[1/10]	[1/10]	[1/10]
<ul style="list-style-type: none"> in out r1 r2 top 	<ul style="list-style-type: none"> inner_top_interface outer_in_interface outer_out_interface outer_top_interface r1_inner_interface 	<ul style="list-style-type: none"> outer_out_interface outer_top_interface r1_inner_interface r1_outer_interface r2_inner_interface
Interface Options <input checked="" type="checkbox"/> Periodic Boundary Condition <input type="checkbox"/> Periodic Repeats <input type="checkbox"/> Coupled Wall <input checked="" type="checkbox"/> Matching <input type="checkbox"/> Mapped <input type="checkbox"/> Static	Boundary Zones Side 1 Boundary Zones Side 2	Interface Wall Zones Side 1 Interface Wall Zones Side 2 Interface Interior Zones r1-periodic
Periodic Boundary Condition Type <input type="radio"/> Translational <input checked="" type="radio"/> Rotational Offset Angle (deg) 120		
<input checked="" type="checkbox"/> Auto Compute Offset Mapped <input type="checkbox"/> Enable Local Tolerance <input type="text" value="1"/> <input type="checkbox"/> Local Edge Length Factor		
<input type="button" value="Create"/> <input type="button" value="Delete"/> <input type="button" value="Draw"/> <input type="button" value="List"/> <input type="button" value="Close"/> <input type="button" value="Help"/>		

Create/Edit Mesh Interfaces

Mesh Interface	Interface Zones Side 1	Interface Zones Side 2
periodic-2	r1_outer_interface	r2_outer_interface
[1/10]	[1/10]	[1/10]
<ul style="list-style-type: none"> in out r1 r2 top 	<ul style="list-style-type: none"> outer_in_interface outer_out_interface outer_top_interface r1_inner_interface r1_outer_interface 	<ul style="list-style-type: none"> outer_top_interface r1_inner_interface r1_outer_interface r2_inner_interface r2_outer_interface
Interface Options <input checked="" type="checkbox"/> Periodic Boundary Condition <input type="checkbox"/> Periodic Repeats <input type="checkbox"/> Coupled Wall <input checked="" type="checkbox"/> Matching <input type="checkbox"/> Mapped <input type="checkbox"/> Static	Boundary Zones Side 1 Boundary Zones Side 2	Interface Wall Zones Side 1 Interface Wall Zones Side 2 Interface Interior Zones r2-periodic
Periodic Boundary Condition Type <input type="radio"/> Translational <input checked="" type="radio"/> Rotational Offset Angle (deg) 120		
<input checked="" type="checkbox"/> Auto Compute Offset Mapped <input type="checkbox"/> Enable Local Tolerance <input type="text" value="1"/> <input type="checkbox"/> Local Edge Length Factor		
<input type="button" value="Create"/> <input type="button" value="Delete"/> <input type="button" value="Draw"/> <input type="button" value="List"/> <input type="button" value="Close"/> <input type="button" value="Help"/>		

12- Dynamic mesh



13- Solution method

Task Page

Solution Methods

Pressure-Velocity Coupling

Scheme
Coupled

Spatial Discretization

Gradient
Least Squares Cell Based

Pressure
Second Order

Momentum
Second Order Upwind

Turbulent Kinetic Energy
Second Order Upwind

Specific Dissipation Rate
Second Order Upwind

Transient Formulation

Non-Iterative Time Advancement

Frozen Flux Formulation

Pseudo Transient

Warped-Face Gradient Correction

High Order Term Relaxation [Options...](#)

[Default](#)

Appendix C

FE model setup

1- Step

The image shows two overlapping dialog boxes from a software application. The top dialog is titled "Step Manager" and contains a table with the following data:

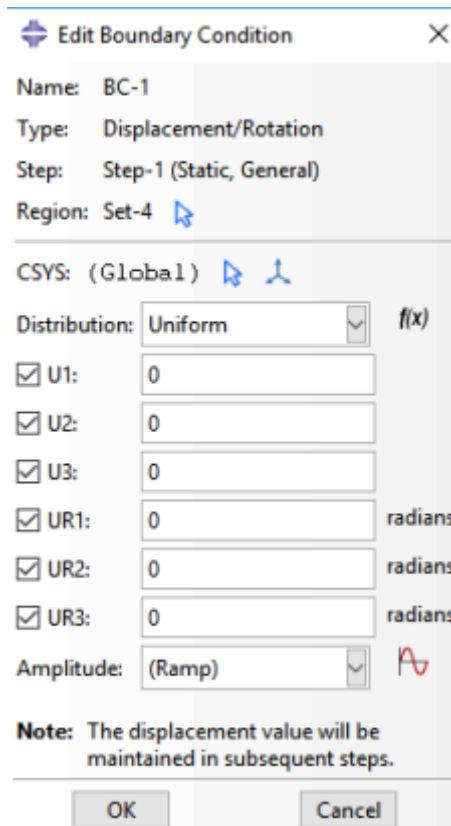
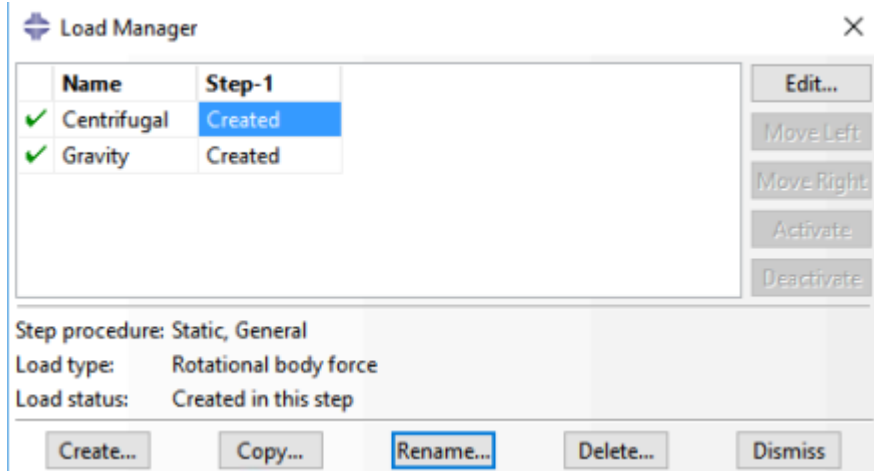
Name	Procedure	Nlgeom	Time
✓ Initial	(Initial)	N/A	N/A
✓ Step-1	Static, General	ON	5

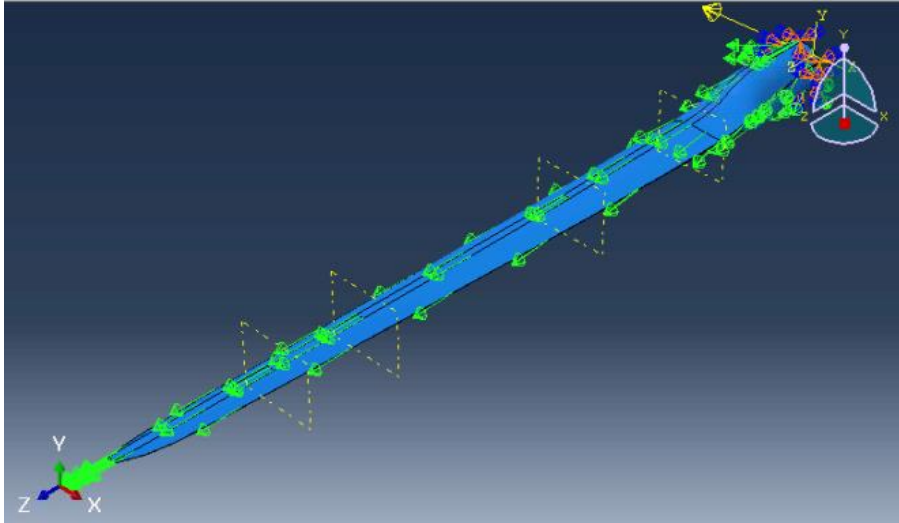
Below the table are buttons for "Create...", "Edit...", "Replace...", "Rename...", "Delete...", "Nlgeom...", and "Dismiss". The "Edit Step" dialog is open over the "Edit..." button. It shows the following settings:

- Name: Step-1
- Type: Static, General
- Tab: Incrementation
- Type: Automatic Fixed
- Maximum number of increments: 10000000
- Increment size: Initial (0.0001), Minimum (5E-08), Maximum (5)

Buttons for "OK" and "Cancel" are at the bottom.

2- Loads

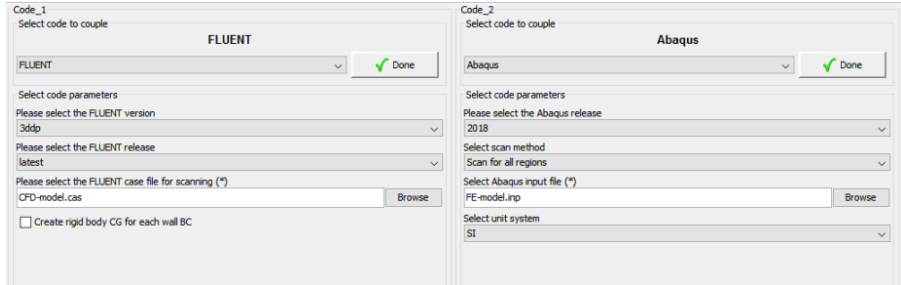




Appendix D

FSI model setup

1- Models step



The screenshot shows two side-by-side configuration panels for Code_1 and Code_2.

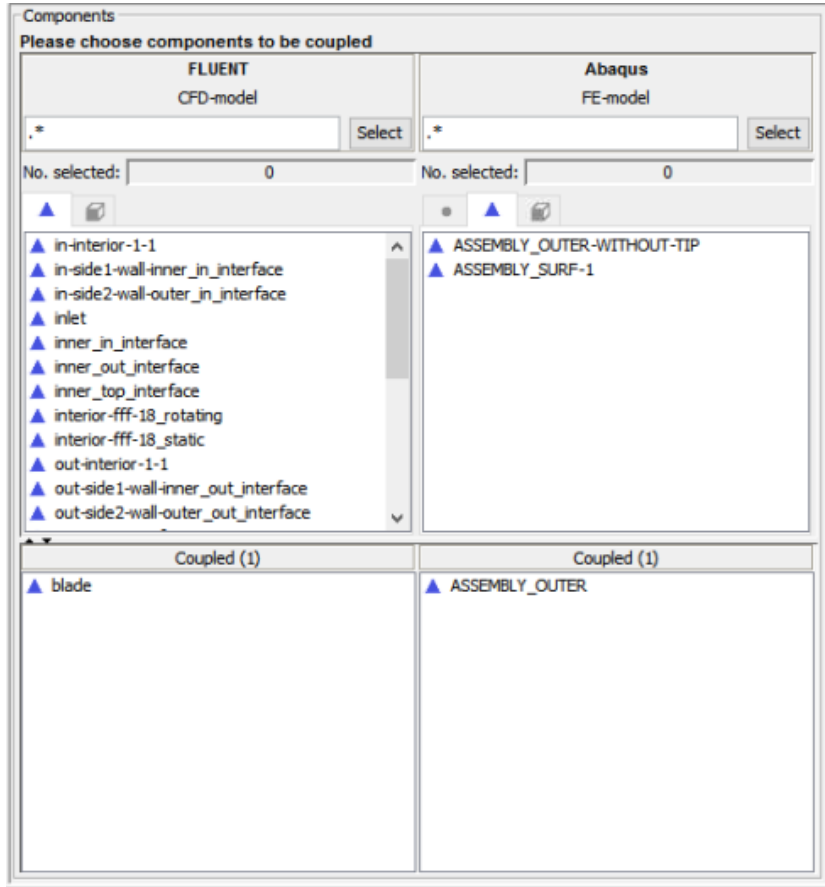
Code_1 (FLUENT):

- Select code to couple: FLUENT (Done)
- Select code parameters: Done
- Please select the FLUENT version: 3ddp
- Please select the FLUENT release: latest
- Please select the FLUENT case file for scanning (*): CFD-model.cas (Browse)
- Create rigid body CG for each wall BC

Code_2 (Abaqus):

- Select code to couple: Abaqus (Done)
- Select code parameters: Done
- Please select the Abaqus release: 2018
- Select scan method: Scan for all regions
- Select Abaqus input file (*): FE-model.inp (Browse)
- Select unit system: SI

2- Build regions

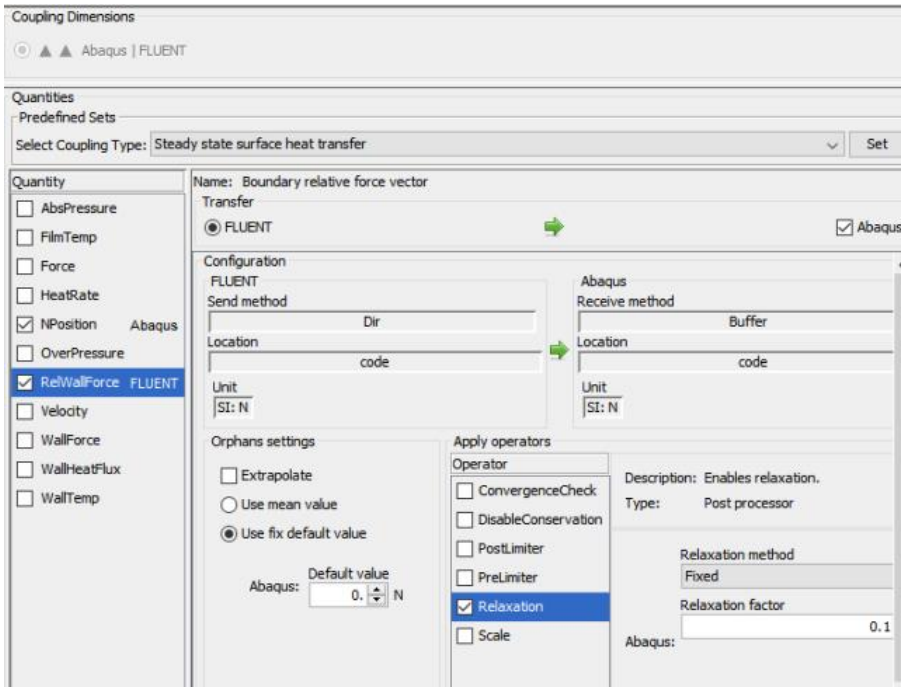


The screenshot shows the 'Components' dialog box with the following sections:

Please choose components to be coupled

FLUENT CFD-model	Abaqus FE-model
.*	.*
No. selected: 0	No. selected: 0
<ul style="list-style-type: none">▲ in-interior-1-1▲ in-side1-wall-inner_in_interface▲ in-side2-wall-outer_in_interface▲ inlet▲ inner_in_interface▲ inner_out_interface▲ inner_top_interface▲ interior-fff-18_rotating▲ interior-fff-18_static▲ out-interior-1-1▲ out-side1-wall-inner_out_interface▲ out-side2-wall-outer_out_interface	<ul style="list-style-type: none">▲ ASSEMBLY_OUTER-WITHOUT-TIP▲ ASSEMBLY_SURF-1
Coupled (1)	Coupled (1)
▲ blade	▲ ASSEMBLY_OUTER

3- Quantity set



4- Go step

